Optical Forces in Complex Beams of Light

by

David B. Ruffner

A dissertation submitted in partial fulfillment
of the requirements for the degree of
Doctor of Philosophy
Department of Physics
New York University
January, 2015

David G. Grier

ProQuest LLC.
789 East Eisenhower Parkway
P.O. Box 1346
Ann Arbor, MI 48106 - 1346

Dedication

To my best friend, my wife, Melissa.

Acknowledgments

This thesis owes its existence to a number of amazing people. They encouraged me to keep asking questions, and they guided and supported me through the difficult process of writing down my results into a, hopefully, coherent story.

First, I would like to thank my advisor, David Grier, for your unfailing optimism, your great sense of humor, and your involvement. Thank you especially for the painstaking editing of this thesis! I am grateful for the great work environment that you created with your positive attitude.

I am grateful to my committee, Alexander Grosberg, Paul Chaikin, Matthew Kleban, and Jasna Brujic, who supported me through the thesis process. Their questions and feedback were invaluable. Special thanks to Paul Chaikin and Alexander Grosberg who taught me soft matter physics, and to Matthew Kleban for his advice.

Thanks to the past and present members of the Grier group that have been my family during my time at the lab. Thank you Fook Chiong Cheong, Lisa Dixon, and Ke Xiao for teaching me so much and for your kindness. Thanks to Hagay Shpaisman for your honest feedback which helped me grow. Bhaskar Krishnatreya, thank you for answering my questions and for your sense of humor.

Thanks to Henrique Moyses for your generosity and dependability, and thanks to Dan Evans for your unique perspective. Special thanks to Henrique, Chen Wang, Mark Hannel, and Aaron Yevick who helped edit this thesis. You all made me look forward to coming to the lab, thank you.

I am indebted to the Physics Department and especially the Center for Soft Matter Research where I've met so many great scientists and amazing human beings. Thanks especially to Jessica Ong and Evette Ma for helping with all of the paperwork that can be the Achilles heel of a graduate student. Thanks to Mark Ofitserov for making things work in the lab. Thanks also to Andrew Hollingsworth for answering all of my questions about the lab and even about basic chemistry.

Thanks for my classmates who were my comrades throughout the difficulties and joys of our time here. Special thanks to Sven Kreiss, Colm Kelleher, Marjorie Schillo, Roberto Gobbetti, and Craig Lage. And thank you to my friends Giovanni Milione, Chris Joseph, Buh Meh Chu, LJ Dequina, Andy McDonough, Giuseppe Barone, Mike Brooks, and Joe Harmon, who supported me and connected me with the outside world.

Thanks to my family for their constant support. Thanks to my dad for introducing me to nature through foraging walks. Thanks to my mom for being a great teacher to me and my siblings and for her encouraging me to study physics. Thanks to brothers and sisters, Helen Kinson, Nathan Ruffner, Lasha Ruffner, Anne Fernandez, Mary Ruffner, Laura Ruffner, and Emma Ruffner. I can't fail when I'm part of such great team. Thanks for being my promoters and being excited about my work.

Thanks to my beautiful wife Melissa for your encouragement and love through my time at NYU. Thank you for always listening to me talk about my research. Your bravery enabled us to go on this adventure together, and your strength supported me and helped me to finish. Thank you for loving me through it all.

Finally thanks be to God for your beautiful creation, but most of all for your love.

Abstract

Light possesses no mass but can transfer momentum to matter and thus can exert forces. This thesis explores these optical forces, focusing on two surprising discoveries: optical forces arising from the spin angular momentum of light and beams of light that can pull, as well as push.

In the first case, we show that non-uniform beams of light can exert a force proportional to the curl of the spin angular momentum density. To show this we have developed a framework for expressing optical momentum in terms of experimentally controlled parameters. This framework makes clear that the curl of the spin angular momentum density contributes to the optical linear momentum. Surprisingly, we find that this contribution does not lead to spin-dependent optical forces at the electric dipole level. Experimentally, however, we find that spin-dependent optical forces do indeed act on isotropic microspheres in focused circularly-polarized beams of light. Theoretically, we confirm that spin-dependent forces appear at higher order in multipole scattering, which explains the experimental results.

Using the same theoretical framework, we show that beams of light can act as tractor beams that pull illuminated objects upstream against the direction of propagation. We demonstrate this extraordinary effect experimentally with optical conveyor beams. These experiments achieve long-range bidirectional transport of colloidal microparticles along propagation invariant beams of light. They show moreover that optical conveyors can move multiple particles simultaneously thanks to the self-healing properties of these modes of light. Not only do optical conveyors constitute practical realizations of tractor beams, but they also act as stronger traps than conventional optical traps and are less sensitive to particle composition. Axial interference endows optical conveyors with these superb trapping properties, which in turn gives them greater range than conventional optical traps. Our work provides a jumping off point towards future work on long-range optical tractor beams and other novel optical micromanipulation.

Contents

List of Figures

Introduction

Light carries momentum. With every scattering, emission or absorption event, therefore, light exerts forces on matter. In simple beams of light, described as plane waves, these forces take the form of radiation pressure that blows objects downstream. In more complicated beams of light, optical force fields can have surprising properties. A prime example of the counterintuitive nature of optical forces was provided by Ashkin in 1986, when he and his coworkers at Bell Laboratories discovered that it was possible to trap and hold a small bead with a focused beam of light, making a laser tweezers [14]. This discovery kick-started the field of optical manipulation [15–17], in which complex optical fields are designed to exert arbitrary forces on small objects. In this thesis, we explore how the local properties of complex beams of light can give rise to nontrivial force fields.

Optical forces are not simply proportional to light's momentum density. In this sense optical forces are an emergent property of the light-matter interaction. Much of the research in optical manipulation relies on classical electromagnetism, which rests on the solid foundation created by Maxwell in the 1870's. Maxwell, however, never suggested that a focused beam of light can act as a trap for small particles, and much less that a beam of light can possess both spin and orbital angular momentum [18] and can exert torque on matter [19]. This may seem surprising because complex beams can always be expressed as a sum of plane waves, which Maxwell and his contemporaries understood. However it is hard to find the specific superposition of plane waves needed to create beams with interesting force fields. This challenge opens up plenty of room for new discoveries in optical manipulation.

Studying the local properties of beams of light offers useful insights into the origin of optical forces. For instance, the radiation pressure exerted by light on a particle can be understood in terms of the Poynting vector, which describes the local flux of energy. This optical energy flux is proportional to its momentum density, which the particle redirects by scattering the light. From conservation of momentum, this scattering leads to the radiation pressure. Optical trapping of dielectric particles also relies on forces that depend on local properties of the beam, in this case the gradient of the intensity [14]. Describing the forces in this way explains the need for tightly focused beams in optical trapping. Only large gradients of intensity can create a force strong enough to counteract the radiation pressure. Understanding optical forces in terms of the beam's properties provides intuition for designing new and interesting optical force fields.

The first part of this thesis focuses on the relationship between the optical spin angular momentum density and optical forces. Each photon of light carries $\pm\hbar$ of spin angular momentum, which Beth verified experimentally in 1936 [20]. Recent experiments suggest that beams with non-uniform polarization not only can exert torques on birefringent particles, but also can exert linear forces even on isotropic particles [7, 21]. Other work has suggested an interesting coupling between the spin and orbital angular momentum of light [22–25], but this has not yet been definitively settled [26–28]. Further progress in this area could open up a whole new channel for implementing optical manipulation.

This thesis aims to clarify the nature of polarization-dependent optical forces. Chapter 2 presents a theoretical framework for understanding the optical momentum density in terms of local characteristics of the beam. This allows us to relate the spin angular momentum density of the light to its linear momentum density. Intuitively this relationship should lead to spin-dependent optical forces, a proposal that we test experimentally in Chapter 4 by observing the motion of colloidal microspheres in beams of light with non-uniform polarization [8]. These measurements provide strong evidence for the influence of optical forces arising from the spin angular momentum of light. We qualitatively explain these spin-dependent optical forces acting on particles with induced multipole moments in Chapter 5.

In the second part of this thesis we focus on how beams of light can pull illuminated objects back to their source. Such beams of light act as tractor beams that have long been a topic for science fiction stories. Since its initial demonstration in 2010 [29] this surprising effect has captured the interest of a growing number of researchers [30–34]. Physically a beam can exert a pulling force on an object that scatters the wave in the forward direction. Because the beam consequently carries more momentum in the forward direction after scattering, the object must recoil in the opposite direction to conserve momentum. This principle was first proposed by Marston in 2006 for acoustic waves [35].

We set Marston's principle to work in optical conveyors beams [36–38], and demonstrate that they act as active tractor beams [12]. Chapter 6 describes how these beams can be projected using holographic methods and how they can pull colloidal microspheres against the direction of propagation. The interferometric structure of these beams leads to excellent trapping properties as is discussed in Chapter 7 [13]. The trapping properties in turn allow them to work at longer range than conventional optical traps and other proposed tractor beams.

Both spin-dependent optical forces and the pulling force of optical tractor beams are examples of counterintuitive optical forces. They are not obvious from the properties of the plane waves that make up these beams. We provide a more physical understanding of these forces by elucidating how they arise from the local variations of spin angular momentum density and intensity, respectively.

Chapter 1

History of Optical Forces and Torques

Serendipitous discoveries characterize the history of the study of optical forces. Although their effects are very small in daily life, optical forces are based on interesting physics and have many applications. In this chapter we will describe some of the coincidences and breakthroughs that created this rapidly developing field, and how our research fits into the story.

Optical forces were first discovered because of the passing of a comet. Halley's comet visits Earth every 75 years. During its return in 1531, it was carefully observed by Petrus Apianus who reported that its tail always points away from the sun [39]. In 1607 Kepler witnessed Halley's comet's next return [40], and he proposed that the the tail is extended by radiation pressure [41]. As early as 1746, Euler used Huygens' wave model for light to place Kepler's conjecture on a firmer footing by demonstrating that waves can exert forces [42]. In this report,

Figure 1.1: The 1066 A.D. appearance of Halley's Comet depicted in the Bayeux Tapestry. Source: Wikimedia Commons [1].

Euler proposed that the visible tail consists of particles liberated from the comet's surface [42].

With each return, Halley's comet continued to influence the understanding of radiation pressure. Referring specifically to the phenomenon of comet tails, Maxwell studied the radiation pressure of light in his seminal *Treatise on Electricity and Magnetism*, published in 1873 [43]. In this work he computed the momentum density carried by a plane electromagnetic wave, and used these calculations to determine the radiation pressure that light can exert on reflecting and absorbing surfaces. Maxwell's predictions were confirmed experimentally by Lebedev in 1901 [44] using a method proposed by Maxwell himself. Any doubt about this experiment was removed in 1903, when Nichols and Hull measured radiation

Figure 1.2: Kepler (left) conjectures there is radiation pressure from observing comets. Euler (right) demonstrates waves can exerts forces. Source: Wikimedia Commons [2,3].

pressure with a more sensitive technique [4]. Interestingly, Nichols and Hull also attempted to verify Kepler's conjecture about comet tails [45].

The possibility that circularly polarized light might exert torque on optically anisotropic objects was not proposed until 1914 [46], and was not demonstrated until Beth's landmark experiments on optically driven torsion oscillators in the 1930's [20,47]. Quantitative agreement with theory provided direct mechanical evidence for the equivalence of circular polarization in classical field theory with photon spin in quantum electrodynamics.

Once established theoretically and experimentally, optical forces and torques received comparatively little attention for several decades, probably because they are too feeble to perceptibly influence most macroscopic systems. Optical forces

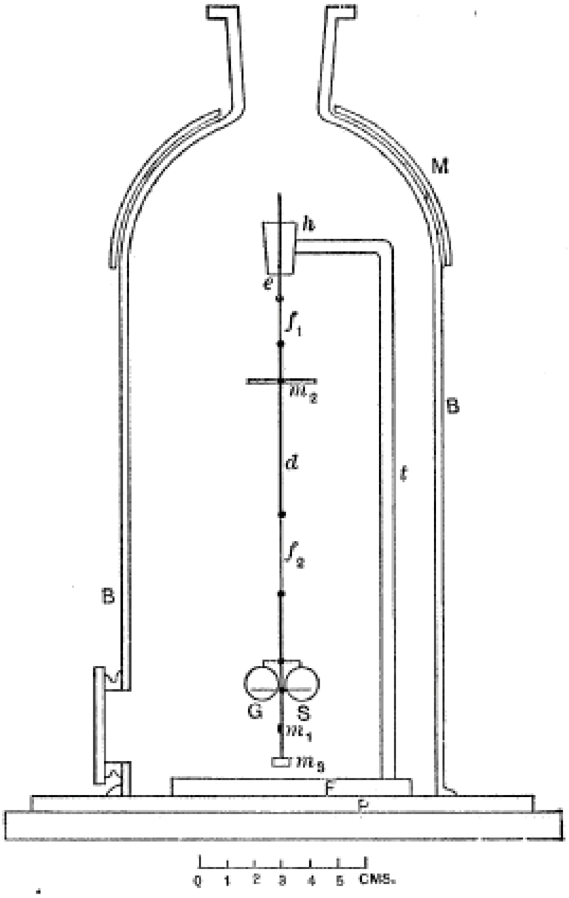

Figure 1.3: Schematic of the experimental apparatus used by Nichols and Hull to measure the radiation pressure of light. Figure from Ref. [4].

scale as P/c, where P is the optical power and c is the speed of light. Since the speed of light is great, optical forces are correspondingly weak. Even such diminutive forces, however, may have a substantial influence on the dynamics of microscopic systems, as Ashkin demonstrated in 1970 by levitating micrometer-scale colloidal spheres against gravity with a collimated laser beam [5]. This breakthrough founded the field of optical micromanipulation.

Ashkin's report included a second crucial innovation. Whereas Lebedev,

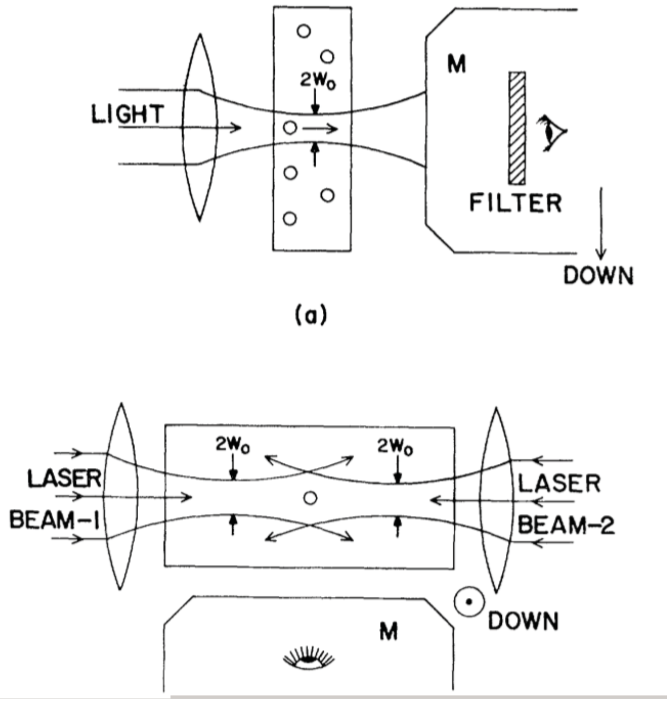

Figure 1.4: Schematic of the experimental apparatus used by Ashkin in the first optical micromanipulation experiments. Reprinted with permission from Ref. [5]. Copyright (1970) by the American Physical Society.

Nichols and Hull relied on reflection to transduce light's momentum into a measurable force, the radiation pressure in Ashkin's experiments resulted from a combination of reflection and refraction at the small particles' surfaces [5,14,48]. An illuminated object redirects the momentum in a beam of light by scattering the light away from its direction of propagation, and then recoils to conserve momentum. Even transparent objects, therefore, can be moved by light, without the ill effects of heating that stymied 19th century attempts to measure radiation pressure. The rich phenomenology of light scattering, moreover, can yield opto-mechanical effects that are both surprising and useful.

A ray-optics description of light's interaction with a dielectric sphere illustrates some interesting features of optical forces. Light scattering by refraction can redirect more optical momentum down the optical axis than would have been present in the unscattered beam. This happens, for instance, when a small dielectric sphere is placed just downstream of the focus in a converging Gaussian beam. The sphere acts as a lens that tends to converge the initially diverging beam toward the optical axis. The resulting recoil force therefore pulls the particle upstream against the radiation pressure due to absorption, reflection and surface scattering. The particle can be trapped by the beam if there is a point in the beam where the recoil force balances radiation pressure. This is the principle behind the optical tweezers that Ashkin and his coworkers discovered in 1986 [14].

The realization that light scattering can usefully harness the momentum density in a beam of light for controlling the motion of microscopic objects sparked a revolution in optical micromanipulation. Applications for optical traps soon were identified in such areas as cellular [49–51] and molecular biology [52–57], in atomic [58] and condensed matter physics [59,60], and in materials science [61,62].

Once optical micromanipulation gained widespread acceptance, researchers from around the world began to investigate in more detail how the properties of a light wave might be harnessed to refine and extend the capabilities of optical traps. Optical tweezers created from circularly polarized light, for example, were demonstrated in 1998 to exert torques on birefringent particles [63, 64]. A landmark article from 1992 proposed that beams of light with helical wavefront structure would carry not only linear momentum and spin angular momentum, but also orbital angular momentum [18] that could be transferred even to optically isotropic objects. This prediction was confirmed experimentally through observations of

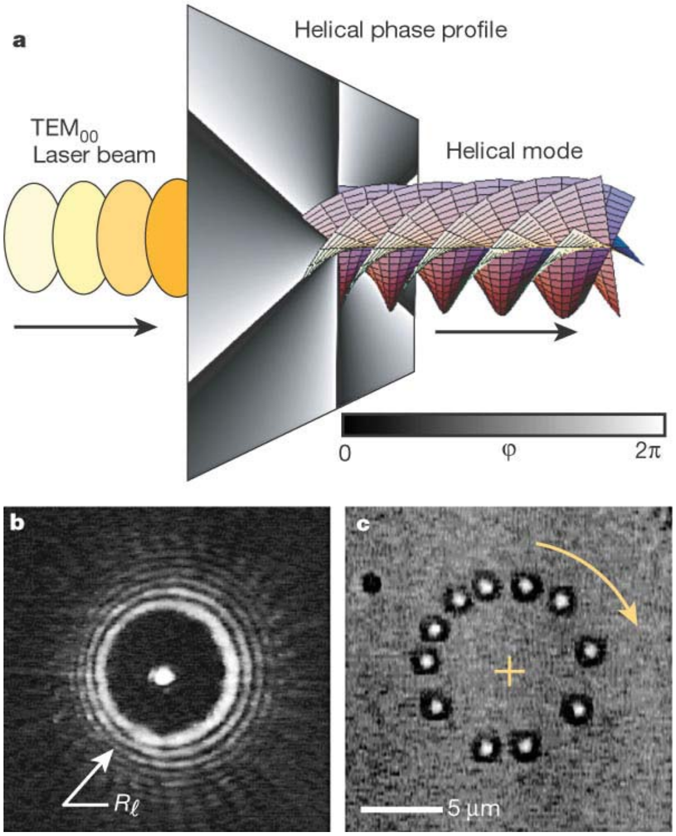

Figure 1.5: An optical vortex, with a helical phase profile. The optical orbital angular momentum of this beam induces colloidal particles to orbit around the beam. Reprinted with permission from Ref. [6]. Copyright (2003) by the American Physical Society.

micrometer-diameter colloidal particles circulating in optical traps created from helical Laguerre-Gaussian modes [19, 65, 66].

Helical modes that carry orbital angular momentum often are created from conventional Gaussian modes by imposing azimuthal phase gradients on the light's wavefronts [67, 68]. Such phase gradients introduce orbital angular momentum by redirecting the light's linear momentum flux into a spiral that winds around the optical axis. The idea of using phase gradients to redirect radiation pressure has

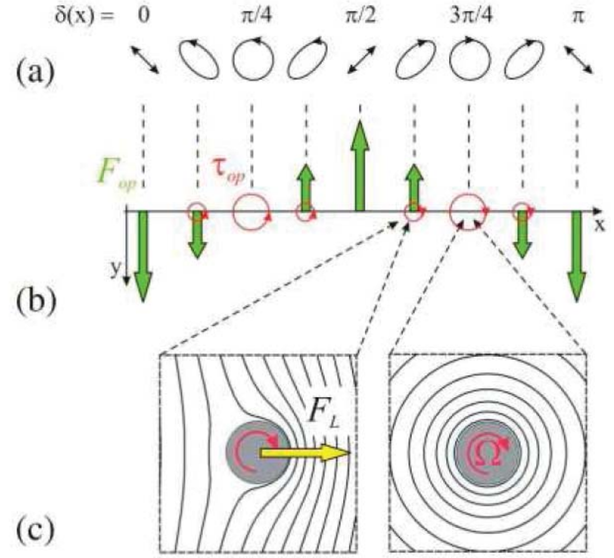

Figure 1.6: Diagram showing optical forces arising from polarization gradients. Figure reprinted with permission from Ref. [7].

been harnessed to create single-beam optical traps that apply specified forces along specified paths in three dimensions [11,69]. These extended optical traps generalize the point-like trap formed by optical tweezers into programmed optical force fields that have been implemented though holographic mode shaping [15, 68, 70].

Most efforts to design and harness optical force and torque fields have relied on the scalar theory of light propagation, in which the polarization is assumed to be uniform throughout the beam. Recently, however, spatial variations in the polarization have been shown to contribute to both the linear forces and also the torques that light can exert [7, 8, 21]. The scalar theory does not account for the vector nature of light and so fails to address potentially valuable opportunities for optical micromanipulation. These opportunities are very promising, particularly given the development of experimental techniques for projecting beams of light with specified amplitude [71], phase [69], and polarization profiles [72].

Spatial control over the polarization of the light can create beams with non-uniform optical spin angular angular momentum, whose properties are not well understood. The nature of the spin angular momentum carried by a beam of light and its relationship to the orbital angular momentum have been subjects of ongoing investigation [73–75]. Spin angular momentum, for example, has been shown to contribute to the orbital angular momentum carried by a beam of light through a process called spin-to-orbit conversion [8, 24, 76]. There is a need for deeper understanding of how this conversion works and how it can be applied.

To address these questions, we explore how optical forces arise in beams with non-uniform spin angular momentum. In Chapter 2, we investigate how non-uniform spin-angular momentum leads to spin-dependent linear momentum. A key step is to write the linear momentum in terms of experimentally accessible parameters, which allows easier comparison to experiment and gives physical insight. These theoretical results indicate the existence spin-dependent optical forces. We describe our experiments that measure these forces in Chapter 4. Then in Chapter 5 we calculate how these forces arise from the light's interaction with the multipole moments of the illuminated particles.

In the second part of this thesis, we study how to extend optical traps over long axial ranges and how to pull particles with light. The limited range of optical tweezers is a major drawback for optical micromanipulation, and has been a subject of intense study. Researchers have made incremental gains in increasing optical trap range by using optical vortices [66], spatially filtered beams of light [48,77,78], and beams of light with spatially varying polarization [79, 80]. Alternatively, the trapping particle can be engineered to improve its trapping properties [81], although this solution is not ideal since it limits generality. Finally, more radical approaches use another force to counter the radiation pressure of the light. For example, counterpropagating traps use another beam of light to balance the radiation pressure from the first beam [82]. This approach allows for optical trapping over long range, but at the cost of additional complexity [83]. Despite substantial advances, the problem of long range optical trapping remains unsolved.

Beams with strong enough diffraction gradients to form optical traps tend to diffract strongly and, consequently, have a very limited range. Counter to this conventional thinking, Durnin created hope for long range optical traps in 1987 with the discovery of nondiffracting modes of light [84]. These optical modes are beams of light whose transverse profile does not change along the axis of propagation. Although, the uncertainty principle dictates that all bounded beams diffract, it is possible for a beam of light to have a finite region where its profile remains almost unchanged with propagation. Durnin experimentally demonstrated such a beam with the profile of a Bessel function, a so-called Bessel beam [85]. Indeed Bessel beams have proved to be useful for trapping colloidal microparticles [86]. These beams can manipulate colloidal microparticles over an impressive range of 3 mm, although in this experiment the colloidal microparticles were not trapped in three dimensions but pressed against the sample chamber by the radiation pressure of the beam [87].

The promise of nondiffracting modes of light opened up the possibility of practical tractor beams. Long features of science fiction stories [88], tractor beams are traveling waves of light that can transport illuminated objects back to their source. The principle for practical implementations of tractor beams was first articulated by Marston in the case of nondiffracting acoustic Bessel beams [35]. The first experimental demonstration of a real-world tractor beam was by Lee *et al.* who used optical solenoid beams to pull colloidal microspheres over a range of 8 µm [29]. This proof of concept demonstration inspired a surge of research activity [30–34,89]. Existing implementations are based on non-diffracting modes of light, most often Bessel beams or superpositions of Bessel beams. It was suggested that the non-diffracting nature of these beams allows them to work over long distances [30]. This prediction has yet to be realized experimentally.

Behind the excitement of tractor beams, there is an unanswered question: What makes a tractor beam fundamentally different than optical tweezers? In fact, optical tweezers have already been called tractor beams [90]. Holographic techniques allow for the creation and movement of optical tweezers in three dimensions. These moving optical traps can pull and transport trapped particles along with them, and have been demonstrated to work over a 40 µm range, greater than that of the optical solenoid beam [91]. In addition, the proposed optical tractor beams based on Bessel beams were predicted to be very sensitive to particle composition, which limits their applicability [31]. In order for the field of tractor beams to move forward, evidence is needed of fundamental advantages of tractor beams over conventional optical traps.

We attacked this problem using optical conveyors as an archetype for optical tractor beams [36–38]. These beams form a series of intensity maxima along the optical axis, which create traps for microparticles. We demonstrate that particles can be pulled by shifting the intensity maxima [12]. This work, described in Chapter 6, suggests optical conveyors have trapping properties superior to conventional optical tweezers. The experiments described in Chapter 7 confirm this prediction, by showing that axial interference endows these beams with excellent trapping properties compared to conventional optical tweezers [13]. These experiments also demonstrate that optical conveyors have longer range than optical tweezers. This provides some of the first evidence that optical tractor beams can lead to qualitative and quantitative improvements in long range optical trapping.

Chapter 2

Photokinetics I

2.1 Optical momentum

The momentum carried by a beam of light is unambiguously described by the Poynting vector which was introduced by John Henry Poynting in 1884 [92]. Despite its familiarity, the Poynting vector can have unexpected properties in non-uniform optical fields. Such fields are characterized by spatially varying amplitude, phase, and polarization, all of which are local and experimentally accessible parameters. One surprise is that the optical momentum flux, written in terms of these parameters, includes two terms accounting for light's angular momentum: one arising from the photon's intrinsic spin angular momentum and another arising from the topology of the beam's wavefronts. Streamlines of the momentum flux define a generalized wave vector, whose behavior can differ from intuition based on geometrical optics.

2.1.1 Optical field in experimental parameters

A monochromatic beam of light with frequency ω may be described with its vector potential,

$$\mathbf{A}\left(\mathbf{r},t\right) = u\left(\mathbf{r}\right)\, e^{-i\omega t}\,\hat{\varepsilon}\left(\mathbf{r}\right), \tag{2.1}$$

where the real-valued amplitude $u\left(\mathbf{r}\right)$ and the complex-valued polarization $\hat{\varepsilon}\left(\mathbf{r}\right)$ both may vary with position $\mathbf{r}$. Each vector component of the polarization

$$\varepsilon_j\left(\mathbf{r}\right) = a_j\left(\mathbf{r}\right)\, e^{i\varphi_j(\mathbf{r})}, \tag{2.2}$$

has a real-valued magnitude $a_j\left(\mathbf{r}\right)$ and phase $\varphi_j\left(\mathbf{r}\right)$. The polarization's normalization then requires

$$\sum_{j=1}^{3} a_j^2\left(\mathbf{r}\right) = 1. \tag{2.3}$$

If the polarization's components have fixed relative phases, φ_j, the common phase may be factored out,

$$\hat{\varepsilon}\left(\mathbf{r}\right) = e^{i\varphi(\mathbf{r})}\sum_{j=1}^{3} a_j\left(\mathbf{r}\right)\, e^{i\varphi_j}\,\hat{e}_j. \tag{2.4}$$

This is the case, for example, in linearly polarized beams of light, for which $\varphi_j = 0$.

One non-standard consequence of adopting Eq. (2.2), is that the polarization of linearly polarized light no longer is real-valued. This notation has the benefit, however, of reflecting typical experimental implementations in which the relevant phases and amplitudes are controlled independently. Moreover, it lends itself to physical interpretation.

In the Coulomb or radiation gauge, the light's electric and magnetic fields are expressed in terms of the vector potential as

$$\mathbf{E}(\mathbf{r},t) = -\partial_t \mathbf{A}\left(\mathbf{r},t\right) \quad \text{and} \tag{2.5}$$

$$\mathbf{H}(\mathbf{r},t) = \frac{1}{\mu} \nabla \times \mathbf{A}\left(\mathbf{r},t\right), \tag{2.6}$$

where μ is the magnetic permeability of the medium.

The forces and torques experienced by illuminated objects depend on the local intensity of the light, specifically the radiative flux,

$$I\left(\mathbf{r}\right) = \frac{c n_m \epsilon_0}{2} \left|\mathbf{E}\left(\mathbf{r},t\right)\right|^2 = \frac{c n_m \epsilon_0 \omega^2}{2} \left|\mathbf{A}\left(\mathbf{r},t\right)\right|^2 = \frac{c n_m \epsilon_0 \omega^2}{2} u^2(\mathbf{r}), \tag{2.7}$$

where c is the speed of light, n_m is the refractive index of the medium, and ϵ_0 is the permittivity of free space. The radiative flux depends only on the local amplitude, $u\left(\mathbf{r}\right)$, and not on the polarization or the phase. For convenience, we introduce the spectral action density,

$$\mathcal{I}\left(\mathbf{r}\right) = \frac{1}{n\omega c} I\left(\mathbf{r}\right), \tag{2.8}$$

which has the units of an angular momentum density and usefully scales the frequency dependence out of our formulation of optical forces and torques.

2.1.2 Momentum from the curl of the spin angular momentum density

The time-averaged linear momentum density carried by a beam of light is given by Poynting's theorem as

$$\mathbf{g}\left(\mathbf{r}\right) = \frac{1}{2c^2}\,\Re\left\{\mathbf{E}^*\left(\mathbf{r},t\right)\times\mathbf{H}(\mathbf{r},t)\right\} \tag{2.9}$$

$$= \frac{\omega}{2\mu c^2}\,\Im\left\{\mathbf{A}^*\left(\mathbf{r},t\right)\times\left[\nabla\times\mathbf{A}\left(\mathbf{r},t\right)\right]\right\}. \tag{2.10}$$

The momentum density can be decomposed into two terms with the identity $\mathbf{a}\times(\nabla\times\mathbf{b}) = \mathbf{a}_i\nabla\mathbf{b}_i - (\mathbf{a}\cdot\nabla)\mathbf{b}$, which eliminates the cross products,

$$\mathbf{g}\left(\mathbf{r}\right) = \frac{\omega}{2c^2\mu}\Im\left\{A_i^*\left(\mathbf{r}\right)\nabla A_i\left(\mathbf{r}\right) - \left[\mathbf{A}^*\left(\mathbf{r}\right)\cdot\nabla\right]\mathbf{A}\left(\mathbf{r}\right)\right\}. \tag{2.11}$$

The divergence of the vector potential is zero in our gauge, which allows us to add another term to the momentum density,

$$\mathbf{g}\left(\mathbf{r}\right) = \frac{\omega}{2c^2\mu}\Im\left\{A_i^*\left(\mathbf{r}\right)\nabla A_i\left(\mathbf{r}\right) - \left[\mathbf{A}^*\left(\mathbf{r}\right)\cdot\nabla\right]\mathbf{A}\left(\mathbf{r}\right) + \left[\nabla\cdot\mathbf{A}\left(\mathbf{r}\right)\right]\mathbf{A}^*\left(\mathbf{r}\right)\right\}, \tag{2.12}$$

and apply another identity, $\nabla\times(\mathbf{a}\times\mathbf{b}) = \mathbf{a}(\nabla\cdot\mathbf{b}) - \mathbf{b}(\nabla\cdot\mathbf{a}) + (\mathbf{b}\cdot\nabla)\mathbf{a} - (\mathbf{a}\cdot\nabla)\mathbf{b})$, to obtain

$$\mathbf{g}\left(\mathbf{r}\right) = \frac{\omega}{2c^2\mu}\Re\left\{iA_i(\mathbf{r})\nabla A_i^*(\mathbf{r})\right\} + \frac{\omega}{2c\mu}\frac{1}{2i}\nabla\times\left[\mathbf{A}^*(\mathbf{r})\times\mathbf{A}(\mathbf{r})\right]. \tag{2.13}$$

References [93] and [25] identify the first term as arising from the orbital angular momentum density and the second from the spin angular momentum density. This fascinating result implies the linear momentum in a beam of light is not independent of the spin or orbital angular momentum; they are intimately connected. The physical meaning of this decomposition, however, is not immediately apparent. It becomes more clear when these results are expressed in terms of experimental parameters.

Rewriting Eq. (2.13) in terms of Eq. (2.1) yields

$$\mathbf{g}\left(\mathbf{r}\right) = -i\,\mathcal{I}\left(\mathbf{r}\right) \sum_{j=1}^{3} \varepsilon_j^*\left(\mathbf{r}\right)\, \nabla\varepsilon_j\left(\mathbf{r}\right) + \frac{i}{2}\nabla\times\left[\mathcal{I}\left(\mathbf{r}\right)\,\hat{\varepsilon}\left(\mathbf{r}\right)\times\hat{\varepsilon}^*\left(\mathbf{r}\right)\right]. \tag{2.14}$$

Normalization of $\hat{\varepsilon}\left(\mathbf{r}\right)$ implies $\nabla\left[\hat{\varepsilon}^*\left(\mathbf{r}\right)\cdot\hat{\varepsilon}\left(\mathbf{r}\right)\right] = 0$ and therefore that the first term in Eq. (2.14) is real-valued. Similarly, the dimensionless quantity

$$\boldsymbol{\sigma}\left(\mathbf{r}\right) = i\,\hat{\varepsilon}\left(\mathbf{r}\right)\times\hat{\varepsilon}^*\left(\mathbf{r}\right) \tag{2.15}$$

is manifestly real-valued. Components of $\boldsymbol{\sigma}\left(\mathbf{r}\right)$ written in terms of the field components using the Levi-Civita antisymmetric tensor ϵ_{ijk},

$$\sigma_i\left(\mathbf{r}\right) = i\sum_{j=1}^{3}\sum_{k=1}^{3}\epsilon_{ijk}\, a_j\left(\mathbf{r}\right)\, a_k\left(\mathbf{r}\right)\, e^{i\left[\varphi_j\left(\mathbf{r}\right)-\varphi_k\left(\mathbf{r}\right)\right]}, \tag{2.16}$$

depend only on differences in relative phases rather than on their absolute values. Because $\boldsymbol{\sigma}\left(\mathbf{r}\right)$ has unit magnitude for circularly polarized light and vanishes for linearly polarized light, we identify it as the helicity of the beam. Dimensional analysis then suggests that

$$\mathbf{s}\left(\mathbf{r}\right) = \mathcal{I}\left(\mathbf{r}\right)\,\boldsymbol{\sigma}\left(\mathbf{r}\right) \tag{2.17}$$

is the spin angular momentum density carried by a beam of light. This interpretation of $\mathbf{s}(\mathbf{r})$ will be placed on a firmer footing in Sec. 2.3.

The first term in Eq. (2.14) is most usefully expressed in terms of the magnitudes and phases of the polarization. The second term is the curl of the spin density. The result [8],

$$\mathbf{g}(\mathbf{r}) = \mathcal{I}(\mathbf{r}) \sum_{j=1}^{3} a_j^2(\mathbf{r})\ \nabla\varphi_j(\mathbf{r}) + \frac{1}{2}\nabla\times\mathbf{s}(\mathbf{r}) \tag{2.18}$$

is a general expression for the linear momentum density in a beam of light.

For the special case of linearly polarized light, the second term on the right-hand side of Eq. (2.18) vanishes, and the remaining term reduces to the remarkably simple form,

$$\mathbf{g}(\mathbf{r}) = \mathcal{I}(\mathbf{r})\ \nabla\varphi(\mathbf{r}), \tag{2.19}$$

which implies that the momentum density is directed by gradients of the phase. The phase gradient is perpendicular to the wavefronts of the beam, and it points in the direction of wavefront motion. Consequently the momentum density also points in this direction. It seems reasonable to expect that small particles illuminated by the beam scatter some of this momentum, and thus experience a force in the direction of the phase gradient [69]. In a plane wave, the phase gradient force reduces to the force from the radiation pressure. In more complex beams the phase gradient force has been used successfully to design three-dimensional force fields for small objects [29, 69, 94, 95].

The first term in Eq. (2.18) generalizes the phase gradient contribution to the momentum density. Each component of the polarization defined by Eq. (2.2) has its own phase. These phases have different spatial dependence in beams of

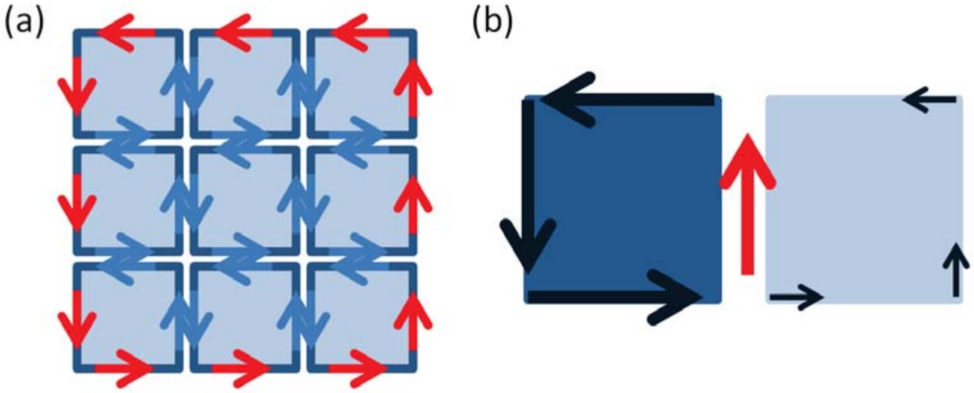

Figure 2.1: Schematic of the momentum flux from the curl of optical spin angular momentum. (a) Cross section of a beam of light with uniform circular polarization, where the small squares represent the optical spin angular momentum at each point in the beam. The red arrows represent the resulting circulation of momentum flux around the beam perimeter. (b) Non-uniform optical spin angular momentum represented by the size of the arrows and the color of the squares creates a flux of optical momentum given by the red arrow.

light with spatially varying elliptical polarization. Therefore each component can carry momentum in independent directions, which is described by the sum in the first term of Eq. (2.18). Although this contribution to the momentum density depends on the polarization, it is not otherwise deeply connected with the quantum mechanical spin of the light's photons [25]. Rather, it is a contribution to the momentum density directed by phase gradients.

The spin-curl term [8] in Eq. (2.18) arises only in elliptically or circularly polarized beams of light and is intimately connected with photon spin, as will be made clear in Sec. 2.3. It arises both for spatially varying helicity in non-uniformly polarized beams and, more commonly, for intensity variations in beams with non-zero helicity. This resulting non-uniform spin angular momentum density creates a bound current of optical momentum as is shown in Fig. 2.1(a). Fig. 2.1(b) shows how this bound current is created from incomplete cancellation of optical spin angular momentum.

2.2 The generalized wave vector

The streamlines of optical momentum density provide powerful visualization of the spin-curl contribution to the optical momentum density. The trajectories of these streamlines follow the generalized wave vector, which is related by definition [25] to the time-averaged momentum density,

$$\mathbf{q}(\mathbf{r}) = \frac{\mathbf{g}(\mathbf{r})}{\mathcal{I}(\mathbf{r})}. \tag{2.20}$$

The streamlines in Fig. 2.2 are plotted for a focused beam of circularly polarized light. The spin angular momentum density in such a beam twists the streamlines around the optical axis as they converge to the focus.

The curved trajectories of these streamlines indicate that they are not rays defined by a conventional wave vector. This observation prompts us to investigate the properties of the generalized wave vector. Interestingly, this classical quantity can be understood quantum mechanically. In addition, the generalized wave vector provides insight into how energy flows through interferometrically structured beams. Results from this analysis have practical applications in optical trapping and in particle tracking.

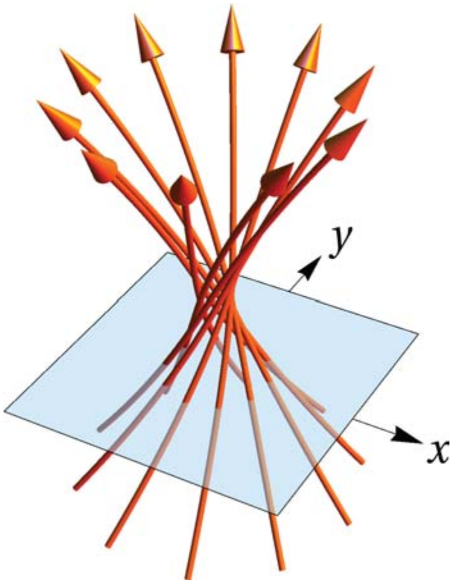

Figure 2.2: Streamlines of the momentum flux in a strongly focused circularly polarized optical tweezers. Figure from Ref. [8].

In the associated quantum-mechanical description, $\mathbf{p}(\mathbf{r}) = \hbar\mathbf{q}(\mathbf{r})$ is the expectation value of the photon momentum measured at position $\mathbf{r}$ [25, 96] using a weak measurement [97]. Recently this quantity has been measured in a single-photon interference pattern by Kocsis *et al.* who interpreted it as the average trajectory of the photons [98]. Bliokh *et al.* connected that experiment to the classical quantities that we are discussing here [99]. The quantum mechanical definition of the generalized wave vector provides context to understand some of its other unusual properties.

The magnitude of the generalized wave vector can vary with position, and vanishes altogether in standing waves. The variability of $q(\mathbf{r}) = |\mathbf{q}(\mathbf{r})|$ is crucial for the performance of single-beam optical traps since it can lead to an optical pulling force. A converging or diverging beam can have some momentum transverse to the optical axis, making $q(\mathbf{r})$ less than ω/c. A scatterer can redirect this momentum along the optical axis and thus recoil in the opposite direction, or be pulled by the light. This effect is harnessed most dramatically in the operation of the tractor beams described in Chapter 6.

The wave vector in a general beam of light need not be transverse to the polarization. The transversality condition $\mathbf{q}(\mathbf{r}) \cdot \hat{\varepsilon}(\mathbf{r}) = 0$ is not satisfied in general; the light in a non-uniform beam may have some degree of longitudinal polarization. Although this notion does not arise in discussions of uniformly polarized paraxial beams, it is well studied in the context of radially-polarized [100] and strongly focused [101] beams of light.

These considerations suggest that quite extraordinary effects should be expected in beams of light whose amplitude, phase, and polarization profiles are chosen suitably. The vector potential describing a freely propagating beam of light must satisfy Maxwell's wave equation,

$$\nabla^2 \mathbf{A}(\mathbf{r}, t) = \frac{1}{c^2} \frac{\partial^2}{\partial t^2} \mathbf{A}(\mathbf{r}, t) . \tag{2.21}$$

Substituting Eq. (2.1) into Eq. (2.21) and gathering the real-valued terms yields

$$\sum_{j=1}^{3} a_j^2(\mathbf{r}) \left[|\nabla \varphi_j(\mathbf{r})|^2 - \frac{\nabla^2 a_j(\mathbf{r})}{a_j(\mathbf{r})} - \frac{\nabla^2 u(\mathbf{r})}{u(\mathbf{r})} \right] = \frac{\omega^2}{c^2}, \tag{2.22}$$

which constrains variations in the constituent amplitudes and phases.

For linearly polarized light, the wave vector reduces to $\mathbf{q}(\mathbf{r}) = \nabla \varphi(\mathbf{r})$ and Eq. (2.22) reduces to

$$q^2(\mathbf{r}) - \frac{\nabla^2 u(\mathbf{r})}{u(\mathbf{r})} = \frac{\omega^2}{c^2}. \tag{2.23}$$

Whereas $\mathbf{q}\left(\mathbf{r}\right)$ describes a propagating wave, the second term on the left-hand side of Eq. (2.23) describes a standing-wave component of the beam that carries no momentum. This term vanishes for plane waves and may be ignored in the paraxial approximation, in which case Eq. (2.23) reduces to the familiar dispersion relation for plane waves, $q^2 = \omega^2/c^2$.

The fact that Eq. (2.22) is different from the familiar dispersion relation is related to the uncertainty principle. The dispersion relation connects the energy of a wave to its momentum. More precisely, the wave equation connects the expected value of the squared energy of the wave with the expected value of the squared momentum,

$$\left\langle \hat{p}^2 \right\rangle = \frac{\left\langle \hat{E}^2 \right\rangle}{c^2}, \tag{2.24}$$

where $\hat{p}$ is the momentum operator, $\hat{E}$ is the energy operator, and the brackets indicate the time-averaged expectation value. Dividing by $\hbar$, assuming monochromatic light, and using the definition of the variance, we arrive at

$$q^2 + \sigma_q^2 = \frac{\omega^2}{c^2}, \tag{2.25}$$

where q is the expectation value of the wave vector and σ_q^2 is its variance. Consequently for linearly polarized light, we see from Eq. (2.23) that $\sigma_q^2 = -\nabla^2 u\left(\mathbf{r}\right)/u\left(\mathbf{r}\right)$. This quantity is the uncertainty in the photon momentum and is related to the spatial variations of the beam. This relationship between localization and momentum uncertainty is intimately connected to the uncertainty principle [102].

The generalized dispersion relation can be applied practically toward esti-

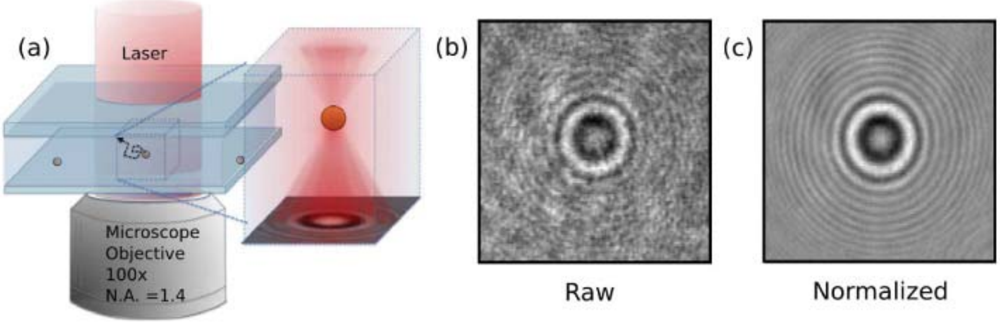

Figure 2.3: (a) Schematic of holographic imaging setup. A laser illuminates a sample containing a colloidal microparticle. (b) The objective captures the incident and scattered light which form a raw hologram. (c) This raw hologram can be normalized by a background image. Figure from Ref. [9]

.

mating the axial position of a microsphere in digital holographic microscopy [9,103], using the setup shown schematically in Fig. (2.3). A collimated laser illuminates a colloidal microparticle, and the resulting interference pattern is imaged by a camera. This technique will be described in more detail in Chapter 3. The generalized dispersion relation provides a way to understand the interference pattern in terms of the uncertainty of the photon momentum. According to Eq. (2.25), uncertainty in the momentum of the observed photons corresponds to fluctuations in the intensity.

In the case of scattering from a small particle, the photons can have momentum either in the direction of the unscattered wave or else pointed away from the scatterer. This choice creates uncertainty and causes an interference pattern. The interference is locally a sinusoidal pattern with a spatial frequency that is proportional to the angle between the incident and the scattered light. Consequently the local curvature of the interference pattern determines the uncertainty in the photon momentum according to Eq. (2.25). The direction of the scattered light can then be deduced since the direction of incident light is known. Propagating these scattered rays back to their source provides an estimate of the position of the scatterer.

The imaginary terms from the wave equation, Eq. (2.21), yield a continuity condition

$$\mathbf{q}\left(\mathbf{r}\right) \cdot \nabla \ln I\left(\mathbf{r}\right) = -\nabla \cdot \mathbf{q}\left(\mathbf{r}\right), \tag{2.26}$$

which shows that the intensity in a beam of light cannot change along the direction of propagation unless the wave vector diverges or converges. This behavior implies

$$\nabla \cdot \mathbf{g}(\mathbf{r}) = 0, \tag{2.27}$$

which ensures that the time averaged energy is locally conserved. The optical energy is thus transported along $\hat{q}\left(\mathbf{r}\right)$ along with its momentum. This same result also reveals that streamlines of $\mathbf{q}\left(\mathbf{r}\right)$ can follow curved paths. They differ in this respect from the linear light rays of geometric optics. Whereas individual photons still propagate on average along straight lines, streamlines of $\mathbf{q}\left(\mathbf{r}\right)$ track the expectation value of their propagation direction and can follow more general trajectories that satisfy Eq. (2.26).

2.3 Derivation of the separation between optical spin and orbital angular momentum

The generalized wave vector gives insight into the behavior of the momentum flux in a beam of light, but it does not provide the reason for identifying the terms in Eq. (2.18) as related to the spin and the orbital angular momentum. The source of this splitting can be found in the conservation of angular momentum in the optical field. In this section we derive this result using the electromagnetic stress-energy tensor.

The stress-energy tensor describes the conservation of both energy and momentum. It is derived from the Lagrangian of the electromagnetic field [104],

$$\mathcal{L} = -\frac{1}{4\mu_0} F_{\mu\nu} F^{\mu\nu}, \tag{2.28}$$

where $F^{\mu\nu} = \partial^\mu A^\nu - \partial^\nu A^\mu$, and A^μ is the vector potential. We will drop the spatial and time dependence in this section for clarity, and we will employ Einstein summation notation with indices running from 0 to 4 with time being the 0th dimension. The electric and magnetic fields are then $E^i/c = -F^{0i}$ and $\epsilon^{ijk} B^k = -F^{jk}$. The canonical stress energy tensor for a vector field ϕ_k is

$$T_c^{\mu\nu} = \frac{\partial \mathcal{L}}{\partial \left(\partial_\mu \phi_\lambda\right)} \partial^\nu \phi_\lambda - g^{\mu\nu} \mathcal{L}, \tag{2.29}$$

where $g^{\alpha\beta}$ is the metric of the space. One of the main properties of the canonical stress-energy tensor is that it satisfies the local momentum conservation equation,

$$\partial_\mu T_c^{\mu\nu} = 0. \tag{2.30}$$

To calculate this tensor for the electromagnetic field we will use A^μ as the field. Written in terms of the vector potential, the Lagrangian becomes

$$\mathcal{L} = -\frac{1}{2\mu_0}\left(\partial^\mu A^\nu \partial_\mu A_\nu - \partial^\mu A^\nu \partial_\nu A_\mu\right), \tag{2.31}$$

and so the derivative of the Lagrangian is

$$\frac{\partial \mathcal{L}}{\partial(\partial_\mu A_\lambda)} = -\frac{1}{\mu_0} F^{\mu\lambda}. \tag{2.32}$$

In turn, the canonical stress-energy tensor for the electromagnetic field is

$$T_c^{\mu\nu} = \frac{1}{\mu_0}\left(-F^{\mu\lambda}\,\partial^\nu A_\lambda + \frac{g^{\mu\nu}}{4} F^{\alpha\beta} F_{\alpha\beta}\right). \tag{2.33}$$

We separate this into a symmetric and an antisymmetric part by using the fact that $\partial^\nu A_\lambda = F^\nu{}_\lambda + \partial_\lambda A^\nu$ so that

$$T_c^{\mu\nu} = \frac{1}{\mu_0}\left(F^{\mu\lambda}\,F_\lambda{}^\nu + \frac{g^{\mu\nu}}{4} F^{\alpha\beta} F_{\alpha\beta}\right) - \frac{1}{\mu_0} F^{\mu\lambda}\,\partial_\lambda A^\nu. \tag{2.34}$$

At this point, the stress-energy tensor is not unique because a term that is a total derivative could be added to it without affecting the conservation condition. It will turn out that we will need a symmetric stress-energy tensor to conserve angular momentum, and that this constraint will define to a unique energy momentum tensor.

The generalized angular momentum tensor can be written in covariant form,

$$M^{\mu\nu\gamma} = \frac{1}{c}\left(T_c^{\mu\nu}x^\gamma - T_c^{\mu\gamma}x^\nu\right). \tag{2.35}$$

Then the generalized angular momentum density is $M^{0\mu\nu} = p^\mu x^\nu - p^\nu x^\mu$, where $p^\mu = T^{0\mu}/c$ is the momentum density. The generalized angular momentum must be defined in a plane $\mu\nu$ since there is not a unique axis that is perpendicular to a plane in space time. Following Barnett [93], we note that in three dimensions the angular momentum density is

$$j_i = \frac{1}{2}\epsilon_{ijk}M^{0jk}. \tag{2.36}$$

In addition, we can define a flux in the l direction of the angular momentum's ith component to be,

$$M_i^l = \frac{1}{2}\epsilon_{ijk}M^{ljk}. \tag{2.37}$$

Because angular momentum must be conserved, the angular momentum flux must also satisfy a conservation law,

$$\begin{aligned}
\partial_\mu M^{\mu\nu\gamma} &= \frac{1}{c}\partial_\mu\left(T_c^{\mu\nu}x^\gamma - T_c^{\mu\gamma}x^\nu\right) && (2.38)\\
&= \frac{1}{c}\left(\partial_\mu T_c^{\mu\nu}x^\gamma + T_c^{\gamma\nu} - \partial_\mu T_c^{\mu\gamma} - T_c^{\nu\gamma}\right) && (2.39)\\
&= \frac{1}{c}\left(T_c^{\gamma\nu} - T_c^{\nu\gamma}\right). && (2.40)
\end{aligned}$$

Conservation of angular momentum requires the last expression to vanish. Therefore, the stress-energy tensor must be symmetric. However, the canonical stress-energy tensor is not symmetric and so must be symmetrized. Following Jackson [104], we add a divergenceless term,

$$T_S^{\mu\nu} = \frac{1}{\mu_0}\partial_\lambda (F^{\mu\lambda} A^\nu) = \frac{1}{\mu_0} F^{\mu\lambda}\,\partial_\lambda A^\nu, \tag{2.41}$$

to the canonical stress-energy tensor, now denoted as $T_O^{\mu\nu}$. The resulting stress-energy tensor,

$$\begin{aligned} T^{\mu\nu} &= T_O^{\mu\nu} + T_S^{\mu\nu} &(2.42)\\ &= \frac{1}{\mu_0}\left(F^{\mu\lambda}\,F_\lambda{}^\nu + \frac{g^{\mu\nu}}{4} F^{\mu\nu} F_{\mu\nu}\right), &(2.43)\end{aligned}$$

is symmetric so its angular momentum is conserved as needed.

Belinfante showed in 1940 that the canonical stress energy tensor accounts for the orbital angular momentum in a beam of light while the added term accounts for the spin [105]. Both contributions are required for angular momentum conservation. We will reproduce his calculation now in order to clarify why we associate these terms with the spin and orbital angular momentum.

Belinfante identifies

$$s^{\mu\nu\gamma} = \frac{1}{c}\left(x^\mu T_S^{\gamma\nu} - x^\nu T_S^{\gamma\mu}\right) \tag{2.44}$$

with the spin angular momentum density arising from the light's polarization and

$$m^{\mu\nu\gamma} = \frac{1}{c}\left(x^\mu T_O^{\gamma\nu} - x^\nu T_O^{\gamma\mu}\right) \tag{2.45}$$

with the orbital angular momentum density arising from the light's wavefront structure. The spin and orbital terms combine to form the total angular momentum density,

$$j^{\mu\nu\gamma} = \frac{1}{c}\left(x^{\mu}T^{\gamma\nu} - x^{\nu}T^{\gamma\mu}\right). \tag{2.46}$$

To verify this we integrate over the beam to obtain the total spin angular momentum,

$$S^{\mu\nu} = \int s^{\mu\nu 0} d^3x. \tag{2.47}$$

Integrating by parts then yields

$$\begin{aligned} S^{\mu\nu} &= \frac{1}{c}\int x^{\mu}T_S^{0\nu} - x^{\nu}T_S^{0\mu}d^3x \qquad (2.48)\\ &= \frac{1}{c\mu}\int x^{\mu}\partial_{\lambda}(F^{0\lambda}A^{\nu}) - x^{\nu}\partial_{\lambda}(F^{0\lambda}A^{\mu})d^3x \qquad (2.49)\\ &= \frac{1}{c\mu}\int F^{0\nu}A^{\mu} - F^{0\mu}A^{\nu}d^3x. \qquad (2.50)\end{aligned}$$

The integrand does not depend on the choice of origin of the coordinate system, which is a hallmark of spin angular momentum. Consequently, the spatial spin angular momentum density is

$$\begin{aligned} s_i &= \frac{1}{2c}\epsilon_{ijk}\left(\frac{1}{\mu_0}\left(-F^{0j}A^k + F^{0k}A^j\right)\right) \qquad (2.51)\\ s_i &= \frac{1}{2c^2\mu}\epsilon_{ijk}2E^jA^k. \qquad (2.52)\end{aligned}$$

Explicitly expressing the spatial and time dependence yields,

$$\mathbf{s}(\mathbf{r}, t) = \frac{1}{c^2\mu}\mathbf{E}\left(\mathbf{r}, t\right) \times \mathbf{A}\left(\mathbf{r}, t\right). \tag{2.53}$$

Furthermore, the time average of this quantity,

$$\mathbf{s}\left(\mathbf{r}\right)=\frac{1}{2c^{2}\mu}\Re\left\{\mathbf{E}^{*}\left(\mathbf{r},t\right)\times\mathbf{A}\left(\mathbf{r},t\right)\right\},\tag{2.54}$$

can be expressed in terms of the quantities defined in Sec. (2.1.2) as

$$\mathbf{s}\left(\mathbf{r}\right)=\mathcal{I}\left(\mathbf{r}\right)\boldsymbol{\sigma}\left(\mathbf{r}\right),\tag{2.55}$$

where $\boldsymbol{\sigma}\left(\mathbf{r}\right)$ is the local helicity defined in Eq. (2.15) and $\mathcal{I}\left(\mathbf{r}\right)$ is the spectral action density defined in Eq. (2.8). This expression matches the one we found by analyzing the Poynting vector in Eq. (2.18). Therefore it is correct to associate this with the spin angular momentum of the light.

We will end this section with the observation that the optical momentum from the curl of the optical spin angular momentum is conserved, even though the spin angular momentum itself is not. Conservation of this linear momentum arises from the properties of the spin part of the stress-energy tensor. $T_S^{\mu\nu}$ directly satisfies Eq. (2.30) since the derivatives form a symmetric tensor and the field strength tensor $F^{\mu\lambda}$ is anti-symmetric. Consequently both the energy and the momentum associated with the spin part of the stress-energy tensor are locally conserved. Because the total momentum is conserved, the same is true for energy and momentum associated with the orbital part of the stress energy tensor. However the spin angular momentum density is not locally conserved, because both spin and orbital contributions are needed for angular momentum conservation in Eq. (2.38). This fact suggests that forces arising from the optical spin angular momentum density may have surprising properties.

Chapter 3

Experimental control of light fields

3.1 Overview

We want to not only understand the forces that light exerts but also to test our theory experimentally. This requires us to control the optical fields and to have probes that are sensitive to optical forces. To control the optical fields, we used the holographic trapping technique [68, 70, 106, 107], in which the wavefronts of a beam of light are modified by adjusting the phase of the light in one plane. The light then propagates down the optical train and is focused by an objective lens to form the desired optical field. We used colloidal microparticles as our optical probes. These particles, which are a few micrometers in diameter, are a good size for detecting optical forces. They are small enough to feel the effects of the optical forces and yet large enough to be easily observed and tracked. A particle's motion

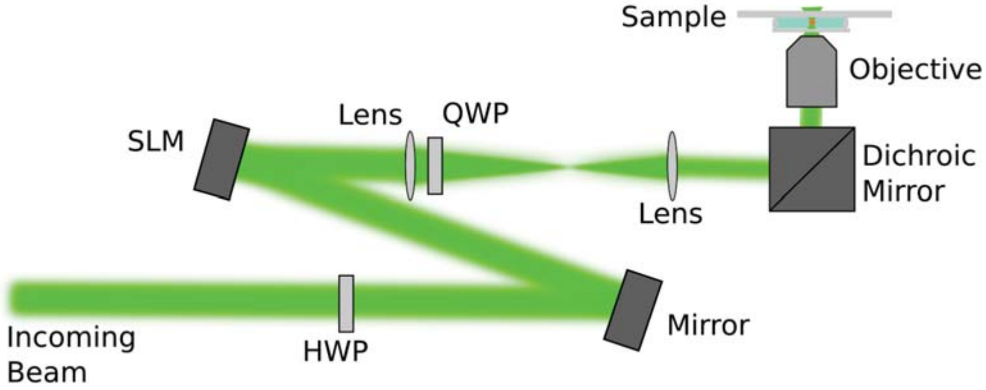

Figure 3.1: Schematic of holographic optical trapping setup

contains information about the optical forces acting on it, allowing us to directly test our theory.

3.2 Holographic Optical Trapping

Holographic optical trapping allows for great control over the optical field [108]. The hologram imparts information to the entire beam allowing complex patterns to be projected instantaneously. This is a great advantage over scanning techniques that use a single beam to form a time-averaged optical potential [109, 110]. Furthermore, holograms can control both the intensity of the light and also its phase. This allows us to create dynamic beams such as optical vortices [65,66,111], arrays of optical vortices [112,113] and optical solenoids [29]. With a few additional optical components, we can also spatially control the polarization of the light. This leads to full control of the light field and allows for some interesting and useful beams of light.

Our holographic optical trapping setup is shown schematically in Fig. (3.1).

The incoming laser beam hits the spatial light modulator (SLM) which imparts a phase hologram to the light. The SLM consists of a liquid crystal screen each of whose pixels can control the phase of the light. It does this by aligning liquid crystals in that pixel with an applied voltage. The refractive index of the liquid crystal layer depends on the molecules' orientation. Light passing through the oriented liquid crystal therefore picks up a phase delay proportional to the locally applied voltage. The back plane of the SLM is reflective so that light passes twice through the liquid crystal layer and picks up twice the phase delay. In this way, a relatively thin layer can impose phase delays of up to 2π on visible light.

After reflection off of the SLM, the modulated beam is relayed by a pair of lenses to the back aperture of the objective lens. The objective lens then focuses this hologram to form the desired optical field in the focal plane. Finally, the light passes through the transparent sample holder where it interacts with colloids that are dispersed in water.

Our implementation of this design is shown in Fig. (3.2). We use a Coherent Verdi V5 as our trapping laser, which has a vacuum wavelength of 532 nm. The beam passes through a beam expander before it hits the SLM (Holoeye Pluto) which makes the beam more uniform. Consequently the mode structure of the light from the laser does not negatively affect our ability to create arbitrary modes of light. The SLM has a 1920×1080 pixel liquid crystal screen which gives it the resolution needed to create detailed holograms. After the light reflects off of the SLM with the encoded hologram, it is relayed by a telescope to the objective lens. The objective then strongly focuses the light to form the desired optical field. We use a high numerical aperture objective (Nikon Plan-Apo 100× NA 1.4, oil immersion).

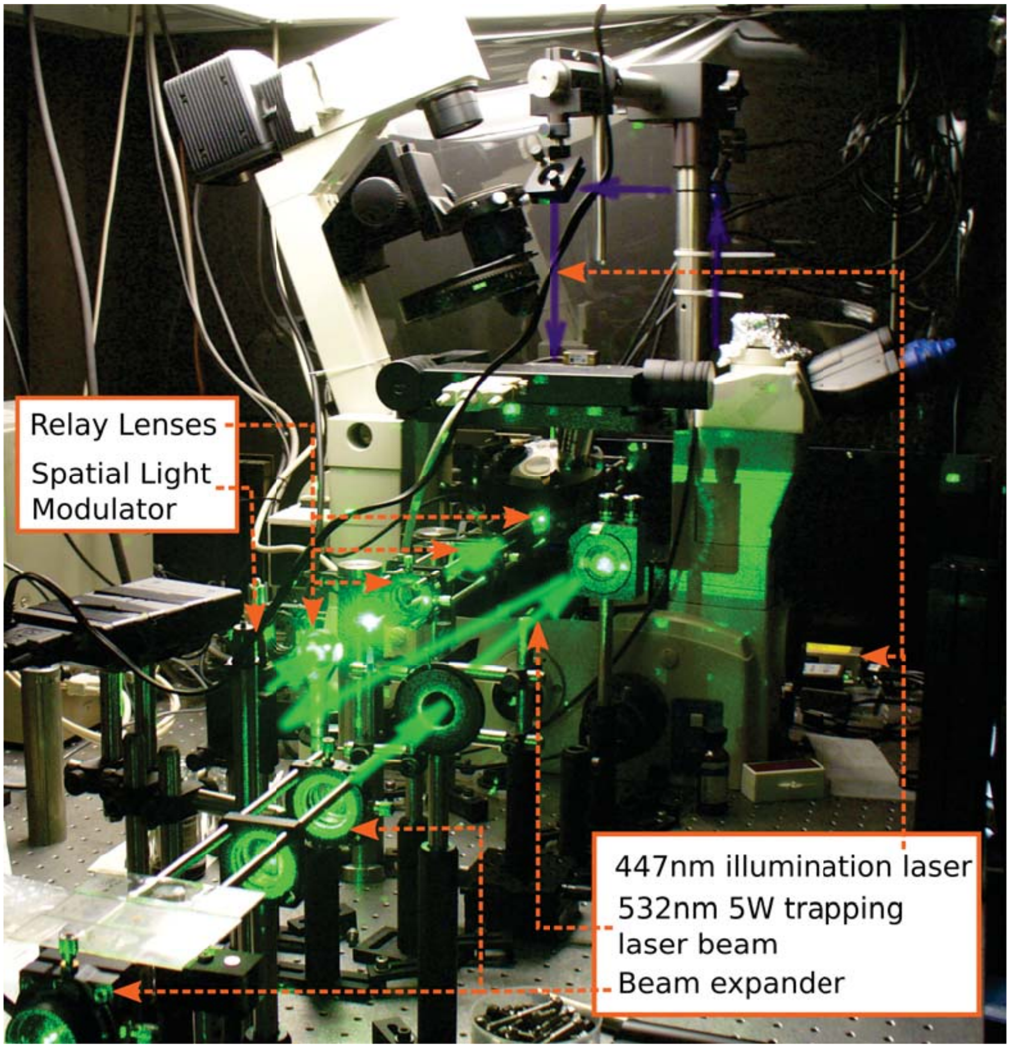

Figure 3.2: Picture of optical trapping setup

The light then passes into the sample, which consists of colloidal microparticles dispersed in water. In experiments discussed in this thesis, we used polystyrene (PS) particles (Polysciences) and silica particles (Polysciences), and always dispersed them in deionized (DI) water (Millipore Millipak*40 0.22μm). We make our sample chamber from a glass microscope slide and a No. 1.5 coverslip which has a thickness of 170 μm. The glass surfaces are cleaned with acetone and isopropanol before assembly. The chamber is sealed with optical adhesive (Norlands Optical Adhesive #68) which is cured under UV illumination. Sealing the sample chamber helps it to last longer and prevents fluid flows, which is important for accurately measuring optical forces.

Finally, we image the particles using either bright field illumination or holographic imaging. In either case the imaging light passes through the sample and is collected by the objective which passes the light through the tube lens to the camera (NEC TI-324AII). Since the trapping laser also passes through the same objective, we use a dichroic mirror to separate the two optical trains.

3.2.1 Projecting holograms

The power of holographic optical trapping arises from the holograms' ability to control both the amplitude and the phase of the light in the focal plane of the objective lens. The problem then is to compute the hologram that projects the desired optical field. In general, this is a challenging inverse problem that can be difficult to solve even numerically. Fortunately, scalar diffraction theory captures much of the important physics of the problem. We will describe this here and discuss more general theories as well.

The light field in the plane of the SLM is relayed to the back aperture of the objective as shown schematically by Fig. (3.3). In scalar diffraction theory, the objective acts to Fourier transform the field [114]. The complex field, $E_f(\mathbf{r}, z)$, in the focal plane of the objective is given by a Fourier transform of the field of the hologram, $E_h(\mathbf{r}, z)$, at the back focal plan of the objective [114],

$$E_f(\mathbf{r}) = \frac{-i}{\lambda f} \int d\rho^2 E_h(\boldsymbol{\rho}) e^{-i\frac{k}{f}\mathbf{r}\cdot\boldsymbol{\rho}} \tag{3.1}$$

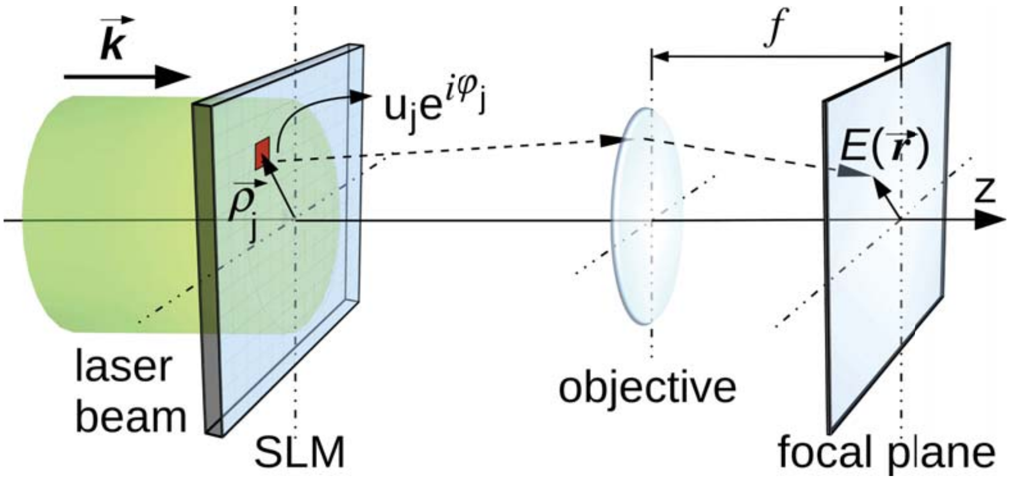

Figure 3.3: Schematic of focusing a hologram by the objective. Image from Fig. 1 of Ref. [10].

where f is the focal length of the objective and where $\boldsymbol{\rho}$ is the position in the hologram plane. Eq. (3.1) neglects the boundary condition imposed by the aperture of the microscope objective, and it also ignores the vector nature of the light.

To obtain the hologram we just inverse Fourier transform the desired field in the focal plane. A few examples illustrate how this works. In each case, we will consider a scalar field in the hologram plane,

$$E_h(\boldsymbol{\rho}) = u_h(\boldsymbol{\rho}) e^{i\varphi_h(\boldsymbol{\rho})}, \tag{3.2}$$

with an amplitude $u_h(\boldsymbol{\rho})$ and a phase $\varphi_h(\boldsymbol{\rho})$. To displace an optical trap in the focal plane, we deflect the light in the hologram plane, or equivalently add a linear phase ramp [115],

$$\varphi_h(\boldsymbol{\rho}) = \frac{k}{f}\mathbf{r}_0 \cdot \boldsymbol{\rho}. \tag{3.3}$$

This phase profile shifts the focal point from the optical axis to a position $\mathbf{r}_0$ in the focal plane. We can also displace the field along the optical axis, although Eq. (3.1) needs to be generalized by propagating the field using scalar diffraction theory. The field at a height z from the focal plane is given by

$$E_f(\mathbf{r}, z) = \frac{-i}{\lambda f} \int d\rho^2 E_h(\boldsymbol{\rho}) e^{-iz\frac{k}{f^2}\rho^2} e^{-i\frac{k}{f}\mathbf{r}\cdot\boldsymbol{\rho}}. \tag{3.4}$$

In a similar spirit to Eq. (3.3) we can displace a trap along the optical axis by imposing a quadratic phase profile upon the incident beam [115],

$$\varphi_h(\boldsymbol{\rho}) = \frac{k}{f^2} z_0 \rho^2. \tag{3.5}$$

Combining these two examples allows us to displace a trap anywhere in the focal volume [108, 115].

More complicated optical fields can be created by superimposing the fields to create a displaced optical trap. Arrays of traps can be created at arbitrary positions in this manner. Furthermore in the continuous case, we can create three-dimensional curves of light, and control the intensity and the phase of the light along the curve [95]. For instance it is possible to focus the light into rings [116] and lines [11]. More exotic possibilities include optical knots [95] and beams in the shape of a solenoid [29].

These more complex beams of light often require not only phase modulation but also amplitude modulation. This is challenging because the spatial light modulator only controls the phase of the light. If only the intensity matters, then there are iterative methods [107, 117] to find the optimal phase pattern in the hologram to create the desired intensity pattern in the focal plane. Alternatively we use the shape-phase technique to approximate amplitude modulation in the hologram [11]. This method works by adjusting each pixel on the SLM so as to displace light away from regions of the hologram with low intensity.

These techniques work remarkably well for projecting holographic optical traps with desired properties. However, to obtain more quantitative results, more complicated theories are required. The first step is to include a pupil function in Eq. (3.1). A pupil tends to obstruct the light that is most strongly converged by the objective lens. Without this strongly converging light, the structure of the resulting optical field is smoothed out. The pupil also creates problems analytically because the transform is no longer invertible, which is one of the main challenges in calculating holograms. Finally, we should also take into account the polarization of the light, especially when we use high numerical aperture objectives. The field at the focus can be calculated by the Richards-Wolf integral [118, 119]. Such vectorial calculations have been applied to holographic trapping by several groups [10, 120].

3.2.2 Polarization control

Polarization adds another degree of freedom to holographic optical trapping, and new advances are taking advantage of beams with spatially varying polarization. For example, cylindrical vector beams [121], beams with polarization varying around the optical axis, have applications in communications [122], imaging [123], and in optical trapping [124]. In particular radially polarized beams have been shown to have greater axial trapping stiffness than regular linearly polarized optical tweezers [80, 125]. As mentioned earlier, there can also be polarization dependent forces such as in a grating of circular polarization [7], which we are interested in explaining.

For our experiments involving the polarization described in this thesis, we use beams of light with uniform circular polarization. Light with this classical polarization is quantum mechanically spin polarized. By varying the intensity we spatially control the spin-angular momentum of the light. We control the intensity using the holographic trapping techniques described above, and control the polarization with waveplates. These waveplates transform the polarization by slowing one component of the light relative to the other. This is accomplished with a birefringent material, that has different indices of refractions along different directions. A quarter wave plate (QWP) circularly polarizes the beam by delaying one component by a quarter wavelength, and a half-wave plate (HWP) similarly delays one component by half a wavelength, which rotates the polarization. Assuming a collimated beam, the transmitted field $\mathbf{E}^{\mathrm{t}}$ by the Jones matrix, $\mathbf{M}$:

$$\begin{pmatrix} E_x^{\mathrm{t}} \\ E_y^{\mathrm{t}} \end{pmatrix} = \mathbf{M} \begin{pmatrix} E_x^{\mathrm{i}} \\ E_y^{\mathrm{i}} \end{pmatrix}. \tag{3.6}$$

The Jones matrix for a QWP or HWP is

$$\mathbf{M}(\delta) = \begin{pmatrix} 1 & 0 \\ 0 & e^{i\delta}, \end{pmatrix} \tag{3.7}$$

where δ is the phase delay, and the slow axis (direction with higher refractive index) is aligned along the y direction. The phase delay is $\pi/2$ for a QWP and π for a HWP. Our setup includes a QWP and HWP after the spatial light modulator, which we can rotate to fully control the uniform polarization of the beam.

3.2.3 Characterizing light fields

Experimental measurements of the projected beams provide information necessary for accurate optical force measurements. They help us to see assess the optical train's alignment and to characterize aberrations. In addition, they help us to see whether our theoretical treatment correctly predicts the intensity distribution of the holographically projected beams. We focused on two main techniques: volumetric reconstruction for measuring the relative intensity distribution near the focus [11], and polarimetry, which enables us the measure the polarization with spatial resolution [126].

Volumetric imaging uses the microscope's imaging train to collect images of the intensity distribution as a function of axial position. We simply replace the sample by a mirrored slide so that the projected beam is reflected back down the imaging train, which is shown schematically in Fig. (3.4). Although the dichroic mirror reflects most of the light back to the SLM, a fraction continues on to the camera. This transmitted light produces a cross-sectional slice of the beam in the focal plane. By shifting the mirror we can reflect different sections of the beam into the focal plane, and consequently can build up a volumetric reconstruction of the beam.

We measure the spatial polarization of the beam by measuring the Stokes parameters [126]. These are a set four parameters that fully describe the polarization state. They can be measured at each point by taking a series of pictures of the beam with polarizers at specific angles. The parameters are defined by the

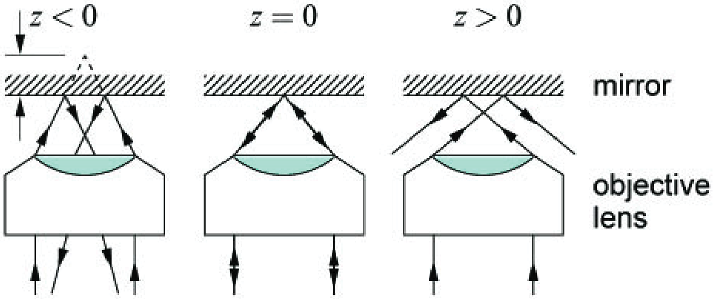

Figure 3.4: Schematic of volumetric imaging. Figure from Ref. [11].

following relations [127],

$$I = I_x + I_y \tag{3.8}$$

$$Q = I_x - I_y \tag{3.9}$$

$$U = I_{45} - I_{-45} \tag{3.10}$$

$$V = I_L - I_R \tag{3.11}$$

where I_x, I_y, I_{45}, and I_{-45} are the intensities measured with a linear polarizer oriented along the x, y, $x + y$, and $x - y$ axes respectively. The I_L and I_R are the left and right circular polarization intensities measured with a circular polarizer. The polarization state can be determined from this set of parameters using the following relations [127],

$$L = Q + iU \tag{3.12}$$

$$A = \sqrt{\frac{I + |L|}{2}} \tag{3.13}$$

$$B = \sqrt{\frac{I - |L|}{2}} \tag{3.14}$$

$$\theta = \frac{1}{2}\arg(L) \tag{3.15}$$

$$h = \mathrm{sng}(V) \tag{3.16}$$

where A and B are the major and minor axes of the polarization ellipse respectively, θ is the inclination angle, and h is the helicity.

Figure (3.5) shows the measured spatial polarization state of a beam immediately after reflecting off of an SLM. The incident light is polarized at 45 degrees relative to the axis of the SLM, although only its x component is phase delayed by the pixels of the SLM. The pattern projected on the SLM is a series of rings with phase delays alternating between 0 and π. When the phase delay is π the x component is flipped, causing the polarization to be rotated into the -45 degree polarization state. Experimentally, we recover this predicted behavior although we do measure that there is some degree of circular polarization. This indicates that the SLM also affects the y component of the light, although to a much lesser degree.

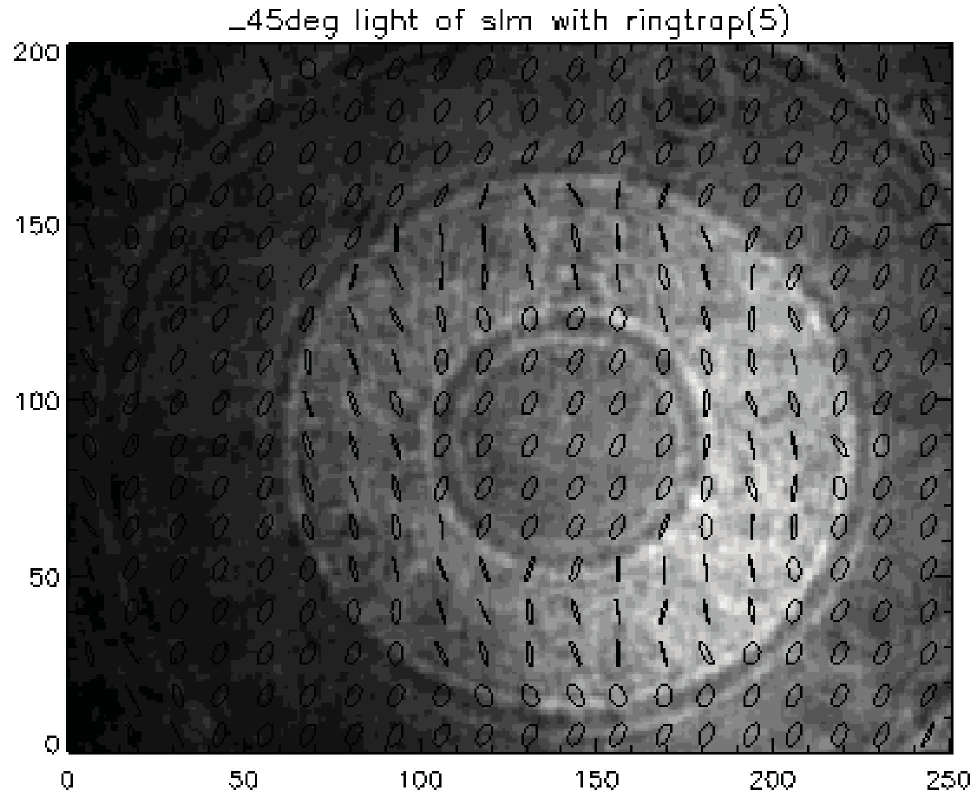

Figure 3.5: Creating and characterizing optical fields with spatially varying polarization

3.3 Holographic imaging

We measure optical forces by observing the motion of colloidal microspheres in an optical field. Extracting the optical force requires accurate measurement of the particle's trajectory over time. We use in-line holographic imaging for this task since it has great resolution in position, works over a large field of view, and over a large axial depth [9, 103].

In-line holographic imaging works by shining a collimated laser at the sample and observing the interference pattern created by the particles scattering

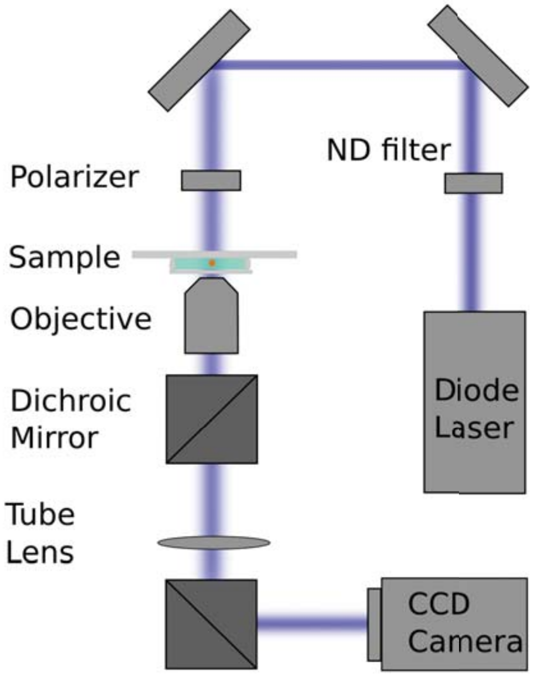

Figure 3.6: Schematic of digital holographic imaging portion of the setup.

the incident beam. Our setup is shown schematically in Fig. (3.6). We use a Coherent Cube laser operating at a vacuum wavelength of 447 nm for illumination. The interference between the incident field, $\mathbf{E}^{\mathrm{i}}(\mathbf{r})$ and scattered field $\mathbf{E}^{\mathrm{s}}(\mathbf{r}-\mathbf{r}_p)$ creates a hologram with intensity,

$$I(\mathbf{r}) = |\mathbf{E}^{\mathrm{i}}(\mathbf{r}) + \mathbf{E}^{\mathrm{s}}(\mathbf{r}-\mathbf{r}_p)|^2 \tag{3.17}$$

where $\mathbf{r}_p$ is the position of the particle. This interference pattern is collected by the same objective used for trapping, and sent to the CCD camera. From there we fit the hologram to predictions of Lorenz-Mie theory [128] which gives us the position, size, and refractive index of the particle [103, 129].

Lorenz-Mie theory allows us to calculate the exact scattered field due to a spherical particle in a homogeneous medium. It is based on matching incident, scattered, and internal fields at the surface of the sphere with appropriate boundary conditions. Lorenz-Mie theory takes advantage of the spherical symmetry of the particle by expanding the fields in a series of the vector spherical harmonics (VSHs), $\mathbf{M}_{nm}^{(i)}(k\mathbf{r})$ and $\mathbf{N}_{nm}^{(i)}(k\mathbf{r})$, which is the natural basis for spherically symmetric fields [128, 130, 131]. This greatly simplifies the boundary conditions at the expense of making the description of the fields more complicated.

Plane wave illumination can be expanded in this basis as [132]

$$\mathbf{E}^{\mathrm{i}}\left(\mathbf{r}\right) = \sum_n a_{n1}\mathbf{M}_{n\pm1}^{(1)}(k\mathbf{r}) + b_{n1}\mathbf{N}_{n\pm1}^{(1)}(k\mathbf{r}), \tag{3.18}$$

where $a_{n\pm1} = E_n$ and $b_{n\pm1} = \pm iE_n$, with $E_n = i^n\sqrt{4\pi(2n+1)}/\sqrt{n(n+1)}$ for right (+) and left (-) circular polarization respectively. Any other polarization state can be attained through a linear combination of left and right polarization. The scattered field can similarly be expanded as [132]

$$\mathbf{E}^{\mathrm{s}}(\mathbf{r} - \mathbf{r}_p) = \sum_n r_{n1}\mathbf{M}_{n\pm1}^{(1)}(k\mathbf{r} - k\mathbf{r}_p) + t_{n1}\mathbf{N}_{n\pm1}^{(1)}(k\mathbf{r} - k\mathbf{r}_p), \tag{3.19}$$

where $\mathbf{r}_p$ is the three dimensional position of the particle relative to the center of the objective's focal plane. The expansion coefficients, r_{n1} and t_{n1}, are related to the incident wave's coefficients by

$$r_{n1} = -a_n a_{n1} \tag{3.20}$$

$$t_{n1} = -b_n b_{n1}. \tag{3.21}$$

The constants of proportionality, a_n and b_n, are the sphere coefficients in Lorenz-Mie theory [128]. These sphere coefficients can be written as

$$a_n = \frac{m\psi_n(mx)\psi_n'(x) - \psi_n(x)\psi_n'(mx)}{m\psi_n(mx)\xi_n'(x) - \xi_n(x)\psi_n'(mx)} \tag{3.22}$$

$$b_n = \frac{\psi_n(mx)\psi_n'(x) - m\psi_n(x)\psi_n'(mx)}{\psi_n(mx)\xi_n'(x) - m\xi_n(x)\psi_n'(mx)}, \tag{3.23}$$

where $x = 2\pi n_m a_p/\lambda$ and $m = n_p/n_m$. The functions $\psi_n(x) = xj_n(x)$ and $\xi_n(x) = xh^{(1)}(x)$ are Riccati-Bessel functions, where $j_n(x)$ is a spherical Bessel function and $h^{(1)}(x)$ is a spherical Hankel function. Primes denote differentiation with respect to the function's argument. Therefore, the sphere coefficients depend on the particle's radius, a_p and refractive index n_p, and the refractive index of the medium, n_m.

Once we have calculated the scattered field we can use Eq. (3.17) to calculate the theoretical intensity distribution for a particle of radius a_p, refractive index n_p, located at r_p. This allows us to compare experiment and theory. We must first process the experimental image, $I_{\text{exp}}(\mathbf{r})$, by subtracting off the camera's dark counts, $I_{\text{dc}}(\mathbf{r})$, which is the instrument's response to the absence of light. Dust and other imperfections along the optical train lead to interference artifacts. We can these eliminate these artifacts by normalizing the image with a background, $I_{\text{bg}}(\mathbf{r})$, which is an image of the field view without the sample present. Taken together we get a normalized hologram,

$$I_{\text{norm}}(\mathbf{r}) = \frac{I_{\text{exp}}(\mathbf{r}) - I_{\text{dc}}(\mathbf{r})}{I_{\text{bg}}(\mathbf{r}) - I_{\text{dc}}(\mathbf{r})}. \tag{3.24}$$

The normalized hologram can then be compared to the theoretical hologram. We use the MPFIT [133] implementation of the Levenberg-Marquardt non-linear least-squares fitter [134] to find the parameters which best fit the experimental data.

Fitting experimental holograms with Lorenz-Mie theory returns excellent estimates of the x, y, and z position of the particle's center as well as its size and refractive index. Measurements of the diffusion of a single colloid in water show that the uncertainty in the x and y position is around a nanometer and in z is around 10 nanometers [135]. The size and refractive index of a colloidal particle with a radius around a micrometer can both be reliably measured with part per hundred resolution or better [129].

In this thesis, we focus on measuring the position of the colloids, since their trajectory gives us information about the optical forces. Holographic imaging is able to give such fantastic position resolution because it uses the information from tens of thousands of pixels in the hologram. This trajectory resolution should not be confused with the Abbe limit for imaging resolution, which is set by diffraction [126]. Holographic tracking offers several benefits relative to other imaging techniques including its large axial range, extending to 100 µm, and its high acquisition speed [9, 103]. Speed, range, and precision all recommend holographic microscopy for measuring optical forces.

Chapter 4

Experimental evidence of forces arising from light's spin angular momentum

4.1 Background

Optical forces arising from the polarization and polarization gradients in vector beams of light constitute a new frontier for optical micromanipulation. Linearly polarized light has been used to orient birefringent objects in conventional optical tweezers [64, 72, 136] and circular polarization has been used to make them rotate [64, 72, 74, 75, 137, 138]. More recently, optically isotropic objects also have been observed to circulate in circularly polarized optical traps [21, 22, 24], through a process described as spin-to-orbit conversion [21, 23, 139–141]. Here, we present a general formulation of the momentum and angular momentum densities in vector beams of light that clarifies how the amplitude, phase and polarization profiles contribute to the forces and torques that such beams exert on illuminated objects. This formulation reveals that spin-to-orbit conversion actually plays a secondary role in circularly polarized optical tweezers. Predicted properties of polarization-dependent optical forces are confirmed through observations of a previously unreported mode of Brownian vortex circulation for an isotropic sphere trapped in elliptically polarized optical tweezers.

4.2 Momentum from the curl of the spin

Radiation pressure is closely connected to the momentum density carried by the light. When a particle scatters light isotropically it absorbs some of the light's momentum and thus experiences a force. This interaction between the scatterer and the beam of light will be considered in more detail in Chapter 5, but here we make the ansatz that the radiation pressure coincides with the momentum density. Using this assumption, we analyze the properties of the optical momentum density, which allows us to make testable predictions of the optical force.

We write the optical momentum density in terms of experimental parameters because they can be controlled for example using holographic techniques [15, 69, 72, 121]. With the common phase factored out of the polarization, the momentum density from Eq. (2.18) becomes

$$\mathbf{g}\left(\mathbf{r}\right) = \mathcal{I}\left(\mathbf{r}\right)\,\nabla\varphi\left(\mathbf{r}\right) - i\mathcal{I}\left(\mathbf{r}\right)\epsilon_j^*\left(\mathbf{r}\right)\nabla\epsilon_j\left(\mathbf{r}\right) + \frac{1}{2}\nabla\times\mathbf{s}\left(\mathbf{r}\right), \tag{4.1}$$

where $\mathcal{I}\left(\mathbf{r}\right)$ is the spectral action density, which is defined in Eq. (2.8) and is proportional to the intensity. In this equation, ϵ_j is the jth component of the polarization and $\mathbf{s}(\mathbf{r})$ is the spin angular momentum density defined in Eq. (2.17), which an associated local helicity, $\boldsymbol{\sigma}(\mathbf{r})$, defined in Eq. (2.15). The projection of $\boldsymbol{\sigma}(\mathbf{r})$ onto the propagation direction $\hat{k}(\mathbf{r})$ is related to the Stokes parameters of the beam [126] by $\boldsymbol{\sigma}(\mathbf{r}) \cdot \hat{k}(\mathbf{r}) = S_3(\mathbf{r}) / S_0(\mathbf{r})$. It achieves extremal values of $+1$ and -1 for right- and left-circularly polarized light, respectively.

The first two terms in Eq. (4.1) leads to the familiar phase-gradient contribution to the radiation pressure [69]. In this context, the second term accounts for the independent phase profiles that may be imposed on the real and imaginary components of the polarization in an elliptically polarized beam. Phase gradients have been used to create three-dimensional optical force landscapes [69], such as knotted force fields [95] and true tractor beams [29]. They also account for the orbital angular momentum density,

$$\ell(\mathbf{r}) = \frac{\omega}{2\mu c^2} I(\mathbf{r}) \left[\mathbf{r} \times \left(\nabla\varphi - i\epsilon_j^* \nabla\epsilon_j\right)\right], \tag{4.2}$$

carried by helical modes of light [18,65]. In this context, the polarization-dependent term in Eq. (4.2) vanishes identically in linearly polarized light, but manifests spin-to-orbit conversion in elliptically polarized beams.

The third term in Eq. (4.1) describes how variations in spin angular momentum contribute to the *linear* momentum density in non-uniform beams of light. Optical forces arising from spatially-varying elliptical polarization have been observed experimentally [7,21,140] but were inappropriately attributed to the curl of the polarization itself. This distinction should be emphasized because polarization-dependent contributions to the momentum density vanish in linearly polarized

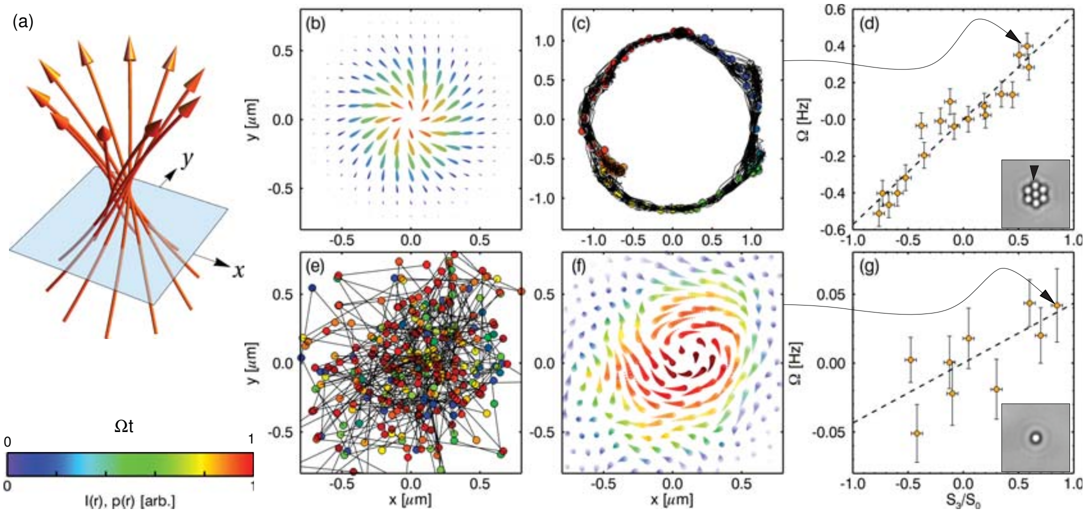

Figure 4.1: (Color online) (a) Streamlines of the momentum density $\mathbf{g}(\mathbf{r})$ in a right-circularly polarized optical tweezers. (b) Components of $\mathbf{g}(\mathbf{r})$ in the plane indicated in (a), shaded by the intensity $I(\mathbf{r})$. (c) Measured trajectory of one particle in a seven-sphere cluster trapped near the focus of the beam. Discrete points show the last three seconds of motion, colored by time. (d) Circulation rate Ω as a function of the beam's Stokes parameters S_3/S_0. Inset: snapshot of the cluster indicating the sphere whose trajectory is plotted. (e) Three seconds of a 3.5-minute trajectory of a single polystyrene sphere diffusing in a circularly polarized optical tweezers, shaded by time. (f) Time-averaged probability flux $\mathbf{j}(\mathbf{r})$ computed from the full measured trajectory. Barbs are colored by the relative probability density $p(\mathbf{r})$ computed from the same trajectory. Brownian vortex circulation is apparent in the vorticity of $\mathbf{j}(\mathbf{r})$. (g) Dependence of the Brownian vortex circulation rate on S_3/S_0. Inset: snapshot of the trapped sphere. The color bar indicates relative intensity $I(\mathbf{r})$ for (b), time for (c) and (e), and relative probability $p(\mathbf{r})$ for (f). From Ref. [8].

light, for which $\hat{\varepsilon}(\mathbf{r})$ is real-valued and $\mathbf{s} = 0$. Variations in linear polarization have no influence on the radiation pressure experienced by optically isotropic objects. The spin-curl contribution, by contrast, gives rise to optical force fields with surprising properties.

Streamlines of $\nabla \times \mathbf{s}$ loop around local extrema in the beam's intensity. Spin-curl forces thus tend to make illuminated objects circulate in the plane transverse to the direction of propagation. Comparable circulation also can arise if orbital angular momentum is transferred from the beam of light to the illuminated particle. The spin-curl term, however, does not contribute to $\ell(\mathbf{r})$. Consequently, observations [22, 24] of optically-induced circulation in spin-polarized optical traps need not imply spin-to-orbit conversion in the light itself. For example, a uniformly circularly polarized beam carrying no orbital angular momentum nonetheless will cause an illuminated object to spiral around the optical axis according to Eq. (4.1).

To illustrate this point, we consider the forces exerted on an optically isotropic colloidal sphere by elliptically polarized optical tweezers. We model the trap as a Gaussian beam of wavenumber k brought to a focus with convergence angle α by a lens of numerical aperture $NA = n_m \sin\alpha$, where n_m is the refractive index of the medium. The beam's initial polarization is

$$\hat{\varepsilon}(\mathbf{r}) = \frac{1}{\sqrt{2}} \left(\hat{x} + e^{i\delta}\, \hat{y}\right), \tag{4.3}$$

with a corresponding incident helicity $\sigma_0 = \sin\delta$ along $\hat{z}$. The focused beam's vector potential may be expressed in cylindrical coordinates $\mathbf{r} = (\rho, \phi, z)$ with the

Richards-Wolf integral formulation [118, 119, 141],

$$\begin{aligned}\mathbf{A}(\mathbf{r}) = -i\, \left[A_0\left(\mathbf{r}\right) + A_2\left(\mathbf{r}\right)\right] \left(\cos\phi + e^{i\delta}\, \sin\phi\right)\, \hat{\rho} \\ - i\, \left[A_0\left(\mathbf{r}\right) - A_2\left(\mathbf{r}\right)\right] \left(e^{i\delta}\, \cos\phi - \sin\phi\right)\, \hat{\phi} \\ - 2\, A_1\left(\mathbf{r}\right) \left(\cos\phi + e^{i\delta}\, \sin\phi\right)\, \hat{z},\end{aligned} \tag{4.4}$$

with amplitudes given by the Fourier-Bessel expansion,

$$A_n\left(\mathbf{r}\right) = \frac{kfu_0}{2i\omega} \int_0^\alpha a_n(\theta)\, J_n(k\rho\sin\theta)\, e^{izk\cos\theta}\, d\theta, \tag{4.5}$$

with expansion coefficients [119]

$$a_0(\theta) = (1 + \cos\theta)\, \sin\theta\sqrt{\cos\theta} \tag{4.6}$$

$$a_1(\theta) = \sin^2\theta\, \sqrt{\cos\theta} \tag{4.7}$$

$$a_2(\theta) = (1 - \cos\theta)\, \sin\theta\, \sqrt{\cos\theta}. \tag{4.8}$$

Computed streamlines of $\mathbf{g}\left(\mathbf{r}\right)$ in a right-circularly polarized optical tweezers ($\sigma_0 = +1$) are shown spiraling around the optical axis in Fig. 4.1(a).

A slice through the beam in the transverse plane indicated in Fig. 4.1(a) reveals the azimuthal component of the transverse momentum density, $g_\perp\left(\mathbf{r}\right) = \mathbf{g}\left(\mathbf{r}\right) \cdot \hat{\phi}$, that is plotted in Fig. (4.1b). The transverse momentum density may be resolved into two contributions

$$g_\perp\left(\mathbf{r}\right) = g_O\left(\mathbf{r}\right) + g_S\left(\mathbf{r}\right) \tag{4.9}$$

arising from the spin-to-orbital and spin-curl contributions to $\mathbf{g}(\mathbf{r})$, respectively:

$$
\begin{aligned}
g_O(\mathbf{r}) &= \frac{2\omega}{\mu c^2}\,\frac{1}{\rho}\,\left[|A_1(\mathbf{r})|^2 + |A_2(\mathbf{r})|^2\right]\,\sigma_0 \quad \text{and} && (4.10)\\
g_S(\mathbf{r}) &= \frac{\omega}{\mu c^2}\,\left[\partial_z \Im\left\{A_1^*(\mathbf{r})\,(A_0(\mathbf{r}) - A_2(\mathbf{r}))\right\}\right. \\
- &\qquad \left.\partial_r\left(|A_0(\mathbf{r})|^2 - |A_2(\mathbf{r})|^2\right)\right]\,\sigma_0. && (4.11)
\end{aligned}
$$

Both components of the azimuthal momentum density are proportional to the helicity of the incident beam, σ_0. They do not, however, contribute equally to the transverse radiation pressure. At the focus, for example, 79% of the transverse momentum density is due to the spin-curl term $g_S(\mathbf{r})$ and only 21% from spin-to-orbit conversion. More generally, both $A_1(\mathbf{r})$ and $A_2(\mathbf{r})$ vanish in the paraxial approximation; there is no spin-to-orbit conversion in weakly focused beams. The spin-curl contribution, by contrast, persists in the paraxial limit. This contribution does not correspond to orbital angular momentum of the light, but rather a contribution to the particle's orbital angular momentum arising from the light's spin angular momentum.

4.3 Observation of the spin-curl force

We probe the properties of spin-dependent optical forces by measuring their influence on the motion of micrometer-scale colloidal spheres. Our system consists of 1.0 µm diameter polystyrene (PS) spheres (Polysciences, Lot # 586632) dispersed in water and trapped in optical tweezers whose helicity σ_0 is controlled with a quarter-wave plate. The isotropic dielectric spheres absorb very little light directly. By scattering light, however, they experience radiation pressure. Our optical tweezers setup is powered by up to 4 W of laser light at a vacuum wavelength of $\lambda = 532\,\mathrm{nm}$ (Coherent Verdi 5W). The beam's polarization is modified with a quarter-wave plate before being relayed with a dichroic mirror to the input pupil of an objective lens (Nikon Plan Apo, 100×, NA 1.4), which focuses the light into a trap. The beam's Stokes parameters are measured in the input plane of the objective lens. The sample is imaged using the same lens in conventional bright-field illumination, which passes through the dichroic mirror to a video camera (NEC TI-324AII). Digitally recorded video is analyzed frame by frame with standard methods of digital video microscopy [142] to measure the trajectory $\mathbf{r}_j = \mathbf{r}(j\tau)$ of a probe particle with 10 nm resolution at $\tau = 29.97\,\mathrm{ms}$ intervals.

The trajectory plotted in Fig. 4.1(c) was obtained for one of seven spheres trapped against a glass surface by a right-circularly-polarized optical tweezers ($\sigma_0 = +0.8$) powered by 1.5 W. The optically-assembled cluster, shown inset into Fig. 4.1(d), spans the region of the beam indicated in Fig. 4.1(b), and thus rotates about the beam axis at a rate of roughly $\Omega = 0.4\,\mathrm{Hz}$. The data in Fig. 4.1(d) confirm the prediction of Eqs. (4.10) and (4.11) that the rotation rate varies linearly with the degree of circular polarization.

The colloidal cluster circulates deterministically in the elliptically polarized optical tweezers because it continuously scatters light in regions where $g_\perp(\mathbf{r})$ is substantial. A single sphere diffusing in an elliptically polarized optical tweezers, by contrast, explores the entire force landscape presented by the light. This includes regions near the optical axis where $g_\perp(\mathbf{r})$ is predicted to vanish. Figure 4.1(e) shows the measured trajectory of one such sphere in a right-circularly-polarized trap ($\sigma_0 = +0.8$) powered by 0.05 W. Optically-induced circulation is not immediately obvious in the noisy trajectory, which is shaded to indicate the passage of time. It becomes evident when the trajectory $\mathbf{r}_j$ is compiled into a time-averaged estimate [143] for the steady-state probability current

$$\mathbf{j}(\mathbf{r}) = \frac{1}{N-1} \sum_{j=1}^{N-1} \frac{\mathbf{r}_{j+1} - \mathbf{r}_j}{\tau} \, \delta_{\sigma_j}\left(\mathbf{r} - \frac{\mathbf{r}_{j+1} + \mathbf{r}_j}{2}\right), \tag{4.12}$$

which is plotted in Fig. 4.1(f). Here $N = 7,000$ is the number of discrete samples, and $\delta_\sigma(\mathbf{r})$ is the kernel of an adaptive density estimator [143] whose width σ varies with the sampling density. The symbols in Fig. 4.1(f) are shaded by the estimated probability density

$$p(\mathbf{r}) = \frac{1}{N} \sum_{j=1}^{N} \delta_{\sigma_j}(\mathbf{r} - \mathbf{r}_j) \tag{4.13}$$

for finding the particle near $\mathbf{r}$. Together, $\mathbf{j}(\mathbf{r})$ and $p(\mathbf{r})$ confirm the prediction of Eqs. (4.10) and (4.11) that circulation vanishes on the optical axis where the particle's probability density is greatest.

The mean circulation rate may be estimated as

$$\Omega = \int \rho(\mathbf{r}) \, [\mathbf{r} \times \mathbf{j}(\mathbf{r})] \cdot \hat{z} \, d^2 r. \tag{4.14}$$

Equation (4.14) improves upon the graphical method for estimating Ω introduced in Ref. [144] by making optimal use of discretely sampled data [143]. Because the single particle spends most of its time in a curl-free region of the optical force field, its circulation rate is substantially smaller than in the deterministic case. Even so, the data in Fig. 4.1(g) again are consistent with the prediction that Ω scales linearly with σ_0.

The single particle's stochastic motion differs qualitatively from the cluster's deterministic circulation. Were it not for random thermal forces, the isolated sphere would remain at mechanical equilibrium on the optical axis. Thermal forces enable it to explore the optical force landscape, where it is advected by the spin-dependent contribution to the radiation pressure. This system, therefore constitutes an example of a Brownian vortex [145, 146], a stochastic machine that uses noise to transduce work out of a static non-conservative force field.

Unlike previous experimental demonstrations of Brownian vortexes [144, 145] the conservative radial restoring force in this system is transverse to the non-conservative spin-curl contribution. Consequently, the particle's radial excursions are described by the Boltzmann distribution [146] $p(\mathbf{r}) = \exp(-\beta U(\mathbf{r}))$ where $\beta^{-1} = k_B T$ is the thermal energy scale at absolute temperature T and $U(\mathbf{r})$ is the potential energy associated with the restoring force. This probability density then is advected by the non-conservative part of the total optical force [146] to yield the transverse probability current

$$\mathbf{j}(\mathbf{r}) = \frac{1}{\xi} p(\mathbf{r}) \left[g_O(\mathbf{r}) + g_S(\mathbf{r}) \right], \tag{4.15}$$

where $\frac{1}{\xi}$ is the particle's effective mobility in the Rayleigh limit, including its scattering cross-section. Because the beam carries little orbital angular momentum, the data in Fig. 4.1(f) thus constitute a map of the spin-curl force. Moreover, because the circulation direction is established unambiguously by the curl of the optical force field, this system constitutes a practical realization of a so-called *trivial optical vortex*, which has been proposed [146] but not previously demonstrated.

Formulating the optical momentum density in terms of experimentally accessible parameters clarifies the nature and origin of the forces that can be applied to microscopic objects using the radiation pressure in beams of light. This formulation confirms previous reports of forces arising from phase gradients [69] and demonstrates that phase-gradient forces act independently of the state of polarization. The spin-curl mechanism unifies forces arising from the curl of the polarization and forces due to intensity gradients in elliptically polarized beams. Because they induce circulatory motion, spin-curl forces are easily misinterpreted as evidence for spin-to-orbit conversion. The spin-curl density, however, does not contribute to the orbital angular momentum of the light. Spin-to-orbit conversion, by contrast, removes spin angular momentum from a beam of light and transmutes it into orbital angular momentum [23]. The present formulation clarifies this mechanism, and suggests that spin-to-orbit conversion has played a secondary role in previous reports of optically-induced circulation. Using Eq. (4.1) as a guide, all three mechanisms now may be optimally leveraged to improve optical micromanipulation and the performance of light-driven machines.

Chapter 5

Photokinetics II

The experimental evidence for spin-dependent optical forces described in Chapter 4 raises the question of their origin. These forces, which act on isotropic colloidal microspheres, behave similarly to the optical momentum density. Intuitively, the light transfers its momentum to the particle through scattering, resulting in a radiation pressure proportional to the momentum density. However, this relationship between optical momentum and optical forces depends on the properties of the particle and needs to be more rigorously considered. In this chapter, we explore how particle properties lead to multipole scattering and how this in turn gives rise to optical forces. These considerations prove to be critical for understanding the origin of the spin-curl force and other photokinetic effects as well. Furthermore calculations from this perspective are naturally compatible with exact theories of light scattering such as generalized Lorenz-Mie theory [131]. The resulting theory, therefore, lends itself to comparison with experiment.

5.1 Force in Rayleigh approximation: no spin dependence

We first consider the simplest scatterer, the electric dipolar particle, which captures much of the physics of optical forces, but still yields some counterintuitive results. The electric dipole moment of an electrically neutral particle responds to the light's electromagnetic fields through the time-averaged Lorentz force [147]

$$\mathbf{F}(\mathbf{r}) = \frac{1}{2}\,\Re\left\{(\mathbf{p}(\mathbf{r},t)\cdot\nabla)\,\mathbf{E}^*(\mathbf{r},t) + \mu\,\partial_t\mathbf{p}(\mathbf{r},t)\times\mathbf{H}^*(\mathbf{r},t)\right\}, \tag{5.1}$$

where $\mathbf{p}(\mathbf{r},t) = \alpha_e\mathbf{E}\,(\mathbf{r},t)$, and α_e is the electric polarizability of the particle. For the present discussion, it is important to note that the polarizability can be complex. The imaginary part of the polarizability accounts for any phase lag between the incident field and the particle's induced polarization. We may express the force in terms of components of the vector potential as [148]

$$\mathbf{F}(\mathbf{r}) = \frac{\omega^2}{2}\,\Re\left\{\alpha_e\sum_{j=1}^{3}A_j(\mathbf{r},t)\,\nabla\,A_j^*(\mathbf{r},t)\right\}. \tag{5.2}$$

Interestingly this expression has a similar form to the first term in Eq. (2.12), which had to do with momentum arising from the orbital part of the momentum density.

In terms of experimentally accessible parameters, the time-averaged force on a dipole-polarizable particle is [149]

$$\mathbf{F}(\mathbf{r}) = \frac{\mu c}{2}\,\alpha_e'\,\nabla I(\mathbf{r}) + \mu c\,\alpha_e''\,I(\mathbf{r})\sum_{j=1}^{3} a_j^2(\mathbf{r})\,\nabla\varphi_j(\mathbf{r}). \tag{5.3}$$

The first term in Eq. (5.3) is the manifestly conservative intensity-gradient force that is responsible for trapping by single-beam optical traps [14]. The second describes a non-conservative force [69] proportional to the phase-gradient term in $\mathbf{g}(\mathbf{r})$ and induces the radiation pressure experienced by a small illuminated particle.

Surprisingly, the spin angular momentum plays no role in Eq. (5.3). This may be appreciated by considering the time-averaged spin angular momentum density

$$\mathbf{s}(\mathbf{r}) = \mathcal{I}\,(\mathbf{r})\,\boldsymbol{\sigma}\,(\mathbf{r}) = i\frac{\omega}{2\mu c^2}\,u^2(\mathbf{r})\,\hat{\epsilon}(\mathbf{r}) \times \hat{\epsilon}^*(\mathbf{r}). \tag{5.4}$$

The cross-product involves cross-terms of the Cartesian components of the polarization. Eq. (5.3), by contrast, involves only diagonal terms. The optically-mediated force therefore does not depend on the spin angular momentum density or on its derivatives.

It is surprising that electric dipolar particles do not experience an optical force from the curl of the spin angular momentum even though the light's momentum density includes a spin-curl contribution. This means that the radiation pressure acting on a particle can point in a different direction from the optical momentum. However, the experimental evidence indicates that larger colloidal microparticles, with size of the order of the wavelength of the light, do experience spin-dependent forces. This raises a question: what properties of the particle allow it to interact with the spin angular momentum in the light? We address this problem in the following sections.

5.2 Connection between scattering and local E&M forces

In the previous section we described the optical force acting on a particle in terms of the local fields exerting forces on the induced electric dipole moment. Although this familiar formulation might seem reasonable for a small dielectric particle, it does not account for observed behavior including that reported in Chapter 4. More generally, we can consider optical forces arising from a scattering process which transfers momentum to the particle. This perspective allows us to calculate additional contributions to the optical force beyond the electric dipole contribution.

The connection between optical force and light scattering is established by calculating the force in terms of the Maxwell stress tensor,

$$F_i = \oint_S T_{ij} n_j d\sigma, \tag{5.5}$$

where S is a surface enclosing the particle, $\hat{n}$ is the unit normal, and T_{ij} is the Maxwell stress tensor, which is given by

$$T_{ij} = \epsilon_0 \left[E_i E_j + c^2 B_i B_j - \frac{\delta_{ij}}{2} \left(\mathbf{E} \cdot \mathbf{E} + c^2 \mathbf{B} \cdot \mathbf{B} \right) \right]. \tag{5.6}$$

This is still a local calculation performed around the particle, but now the properties of the particle are encoded in the fields, which are a sum of the incident field and the scattered field,

$$\mathbf{E} = \mathbf{E}^{\mathrm{i}} + \mathbf{E}^{\mathrm{s}}, \;\; \mathbf{B} = \mathbf{B}^{\mathrm{i}} + \mathbf{B}^{\mathrm{s}}, \tag{5.7}$$

where $\mathbf{E}^{\mathrm{i}}$ and $\mathbf{E}^{\mathrm{s}}$ are the incident and scattered field and similarly for the magnetic field.

If the medium is lossless then electromagnetic momentum is conserved. It is possible, therefore, to extend the integration to a surface at infinity. Then we only have to consider the radiative scattered fields, which have the following properties,

$$\mathbf{B}^{\mathrm{s}} = \frac{\mathbf{k}^{\mathrm{s}} \times \mathbf{E}^{\mathrm{s}}}{ck}, \quad \mathbf{E}^{\mathrm{s}} \cdot \mathbf{k}^{\mathrm{s}} = \mathbf{B}^{\mathrm{s}} \cdot \mathbf{k}^{\mathrm{s}} = 0, \tag{5.8}$$

where $\mathbf{k}^{\mathrm{s}}$ is the local wavevector of the scattered fields. The stress tensor is quadratic in the fields so we can write it as a sum of scattered, incident and mixed terms,

$$T_{ij} = T_{ij}^{\mathrm{i}} + T_{ij}^{\mathrm{s}} + T_{ij}^{\mathrm{mix}}, \tag{5.9}$$

where T_{ij}^{i} and T_{ij}^{s} are just the same stress tensor for the incident and scattered fields respectively, and

$$T_{ij}^{\mathrm{mix}} = \epsilon_0 \left[E_i^{\mathrm{i}} E_j^{\mathrm{s}} + E_i^{\mathrm{s}} E_j^{\mathrm{i}} + c^2 B_i^{\mathrm{i}} B_j^{\mathrm{s}} + c^2 B_i^{\mathrm{s}} B_j^{\mathrm{i}} - \delta_{ij} \left(\mathbf{E}^{\mathrm{i}} \cdot \mathbf{E}^{\mathrm{s}} + c^2 \mathbf{B}^{\mathrm{i}} \cdot \mathbf{B}^{\mathrm{s}} \right) \right]. \tag{5.10}$$

We are integrating over a sphere of infinite radius centered on the scattering particle. Therefore, $n_i = k_i^{\mathrm{s}}/k^{\mathrm{s}}$ where $\mathbf{k}^{\mathrm{s}}$ is the scattered field's wavevector.

Considering first the mixed term, the projection onto the outward normal is

$$
\begin{aligned}
T_{ij}^{\mathrm{mix}} n_j &= T_{ij}^{\mathrm{mix}} k_j^{\mathrm{s}} / k^{\mathrm{s}} \\
&= \epsilon_0 \left[E_i^{\mathrm{s}} \frac{(\mathbf{E}^{\mathrm{i}} \cdot \mathbf{k}^{\mathrm{s}})}{k^{\mathrm{s}}} + c^2 B_i^{\mathrm{s}} \frac{(\mathbf{B}^{\mathrm{i}} \cdot \mathbf{k}^{\mathrm{s}})}{k^{\mathrm{s}}} - \frac{k_i^{\mathrm{s}}}{k^{\mathrm{s}}} \left(\mathbf{E}^{\mathrm{i}} \cdot \mathbf{E}^{\mathrm{s}} + c^2 \mathbf{B}^{\mathrm{i}} \cdot \mathbf{B}^{\mathrm{s}} \right) \right], \qquad (5.11)
\end{aligned}
$$

where we used the fact that the scattered fields are transverse. Using the BAC-CAB rule we can simplify this result,

$$
T_{ij}^{\mathrm{mix}} k_j^{\mathrm{s}} / k^{\mathrm{s}} = \epsilon_0 \left[\mathbf{E}^{\mathrm{i}} \times \frac{(\mathbf{E}^{\mathrm{s}} \times \mathbf{k}^{\mathrm{s}})}{k^{\mathrm{s}}} + c^2 \mathbf{B}^{\mathrm{i}} \times \frac{(\mathbf{B}^{\mathrm{s}} \times \mathbf{k}^{\mathrm{s}})}{k^{\mathrm{s}}} \right]. \qquad (5.12)
$$

Then using the fact that the electromagnetic fields are related through Eq. (5.8), we can write,

$$
T_{ij}^{\mathrm{mix}} k_j^{\mathrm{s}} / k^{\mathrm{s}} = -c g_i^{\mathrm{mix}}, \qquad (5.13)
$$

where g_i^{mix} is the ith component of the momentum density, $\mathbf{g}_i^{\mathrm{mix}} = c^2(\mathbf{E}^{\mathrm{i}} \times \mathbf{B}^{\mathrm{s}} + \mathbf{E}^{\mathrm{s}} \times \mathbf{B}^{\mathrm{i}})/\mu_0$, attributed to the mixed fields.

Next we consider the scattering term again using the fact that the scattered fields are transverse,

$$
T_{ij}^{s} k_j^{\mathrm{s}} / k^{\mathrm{s}} = \epsilon_0 \left[0 - \frac{k_i^{\mathrm{s}}}{2k} (|\mathbf{E}^{\mathrm{s}}|^2 + c^2 |\mathbf{B}^{\mathrm{s}}|^2) \right]. \qquad (5.14)
$$

This is just the energy density of the scattered fields in the opposite direction of propagation, or equivalently,

$$
T_{ij}^{s} k_j^{\mathrm{s}} = -c g_i^{\mathrm{s}}, \qquad (5.15)
$$

where g_i^{s} is the ith component of the momentum density attributed to the scattered fields. Thus the force on the particle can be written as [31],

$$\mathbf{F} = -c \oint_{S_\infty} \left[\mathbf{g}^{\mathrm{mix}} + \mathbf{g}^{\mathrm{s}} \right] d\sigma, \tag{5.16}$$

The incident field does not contribute because of momentum conservation. The particle experiences a force equal and opposite to the momentum flux that arises from scattering.

5.3 Forces from multipole scattering: extinction forces

The incident and scattered fields determine the optical force described by Eq. (5.15). The incident field we assume to be given. The main problem then is to describe the scattered field. The most natural way to do this is to expand it in a series of multipoles. The scattered field from each multipole field interacts with the incident field creating an optical force. These forces are described by the mixing term in Eq. (5.15), and are referred to in the literature as extinction forces [128].

For the case of small particles in the Rayleigh regime, we can explicitly relate the force from scattering momentum in the fields and the force exerted by the local electromagnetic fields. For an electric or magnetic dipole the scattered electric and magnetic fields are given by

$$\mathbf{E}^{\mathrm{s}}(\mathbf{r}) = \frac{k^2}{4\pi\epsilon_0}\frac{e^{ikr}}{r}\left[(\hat{n}\times\mathbf{p})\times\hat{n} - \frac{1}{c}\hat{n}\times\mathbf{m}\right] \quad \text{and} \tag{5.17}$$

$$\mathbf{H}^{\mathrm{s}}(\mathbf{r}) = \frac{ck^2}{4\pi}\frac{e^{ikr}}{r}\left[\frac{1}{c}(\hat{n}\times\mathbf{m})\times\hat{n} - \hat{n}\times\mathbf{p}\right], \tag{5.18}$$

where $\hat{n}$ is a unit vector pointing away from the particle, $\mathbf{p}$ is the electric dipole moment, and $\mathbf{m}$ is the magnetic dipole moment. The interference of these scattered fields with an arbitrary incident field leads to the following optical force on the particle [31, 150, 151],

$$\mathbf{F}^{\mathrm{mix}} = -\frac{1}{c}\oint_{S_\infty}\langle\mathbf{S}^{\mathrm{mix}}\rangle d\sigma \tag{5.19}$$

$$= \frac{1}{2}\Re\big\{p_j^*\nabla E_j^{\mathrm{i}} + m_j^*\nabla B_j^{\mathrm{i}}\big\}, \tag{5.20}$$

where E_j^{i} and B_j^{i} are the j^{th} components of the incident electric and magnetic fields at the particle's position.

We can write the force entirely in terms of the incident field and the polarizabilities, which depend on particle properties. The electric and magnetic dipole moments are give by, $\mathbf{p} = \alpha_e\mathbf{E}$ and $\mathbf{m} = \alpha_m\mathbf{B}$, where α_e and α_m are the electric and magnetic polarizabilities respectively. With these expressions, the total force becomes [150, 151]

$$\mathbf{F} = \frac{1}{2}\Re\big\{\alpha_e^* E_j^*\nabla E_j\big\} + \frac{1}{2}\Re\big\{\alpha_m^* B_j^*\nabla B_j\big\}, \tag{5.21}$$

Which is expressed entirely in terms of the incident fields. This expression is very useful because computing the scattered field can be very difficult in general. The first term in Eq. (5.21) is equivalent to the force on an electric dipolar particle as in Eq. (5.3). The second term describes the contribution from dipole scattering of the magnetic field. Because it has the same form as the first term, we posit that it also does not contribute to a spin-curl force.

The force from the electric quadrupole can similarly be identified [31],

$$F_i^Q = \frac{1}{8}\Re\big\{Q_{ij}\partial_i\partial_n E_j^*\big\}, \tag{5.22}$$

where Q_{ij} is the electric quadrupole polarizability, which for an optically isotropic particle is given by

$$Q_{ij} = \frac{\gamma_e}{2}\left(\partial_i E_j + \partial_j E_i\right). \tag{5.23}$$

This expression for the quadrupole polarizability works for dielectric spheres, because a uniform field only creates a dipole moment. So gradients of the field are necessary to induce a quadrupole moment. Furthermore we symmetrize the electric field gradient tensor because the quadrupole should be symmetric. Consequently, the quadrupole contribution to the optical force is

$$F_i^Q = \frac{1}{8}\Re\Big\{\frac{\gamma_e}{2}\left(\partial_n E_j + \partial_j E_n\right)\partial_i\partial_n E_j^*\Big\}. \tag{5.24}$$

We can interpret this by expanding,

$$F_i^Q = \frac{1}{8}\Re\{\gamma_e\}\Re\big\{\left(\partial_n E_j + \partial_j E_n\right)\partial_i\partial_n E_j^*\big\} - \frac{1}{8}\Im\{\gamma_e\}\Im\big\{\left(\partial_n E_j + \partial_j E_n\right)\partial_i\partial_n E_j^*\big\}. \tag{5.25}$$

The first term on the right hand side of Eq. (5.25) turns out to be a gradient term,

$$\mathbf{F}^{Q1} = \frac{1}{16}\Re\{\gamma_e\}\nabla\left[\left(\partial_n E_j + \partial_j E_n\right)\partial_n E_j^*\right]. \tag{5.26}$$

In contrast to the electric dipole, this gradient is not of the intensity but of a more complicated quantity that itself depends on field gradients. Nevertheless, it represents a conservative force and so can be used for trapping. The second term in Eq. (5.25) is,

$$\mathbf{F}^{Q2} = -\frac{1}{8}\Im\{\gamma_e\}\Im\big\{\left(\partial_n E_j + \partial_j E_n\right)\nabla\partial_n E_j^*\big\}. \tag{5.27}$$

This has the the same form as the phase gradient force for an electric dipole except that the gradient acts on $\partial_n E_j$ instead of E_j. So it seems that it also can be thought of as a phase gradient force. The quadrupole force definitely does not lead to a spin curl force because there are no cross terms linking different components of the electric field.

It seems likely that higher-order multipole terms will continue this pattern of contributing intensity-gradient force terms and phase-gradient force terms, but not more exotic polarization-dependent forces. To explain polarization-dependent effects, we have to look deeper.

5.4 Spin-curl force and more from multipole interference

In addition to interacting with the incident field, scattered multipole fields can interfere with other multipole fields to create a scattering force. The forces from this interference account not only for the spin-curl force but also for additional unconventional contributions to optical forces. We show this by expressing these contributions to the optical force in terms of experimentally accessible quantities.

The interference of the electric and magnetic dipole terms leads to a force [31, 150, 151],

$$\mathbf{F}^{\text{p-m}} = -\frac{k^4}{12\pi c\epsilon_0}\Re\{\mathbf{p}\times\mathbf{m}^*\}. \tag{5.28}$$

where ϵ_0 is the permittivity of free space. Equation (5.28) can be written as

$$\mathbf{F}^{\text{p-m}} = -\frac{k^4 c\mu_0}{12\pi\epsilon_0}\Re\{\alpha_e\alpha_m^*\}\mathbf{g} + \frac{k^4 c}{12\pi\epsilon_0}\Im\{\alpha_e\alpha_m^*\}\Im\{\mathbf{E}\times\mathbf{B}^*\}, \tag{5.29}$$

where we have identified part of this term as a force in the direction of the momentum density, $\mathbf{g}$. The momentum density in turn contains the spin-curl term as we saw in Eq. (2.18). Consequently there is a spin-curl force as long as no other term cancels it, as was the case for the electric dipole term [149].

The second term on the right hand side of Eq. (5.29) is less straightforward to interpret. Applying vector identities yields,

$$\begin{aligned}\Im\{\mathbf{E}\times\mathbf{B}^*\} &= \frac{1}{\omega}\Im\{i\mathbf{E}\times(\nabla\times\mathbf{E}^*)\} && (5.30)\\ &= \frac{1}{2\omega}\nabla E^2 - \frac{1}{\omega}\Re\{(\mathbf{E}\cdot\nabla)\mathbf{E}^*\}. && (5.31)\end{aligned}$$

The first term in Eq. (5.31) is the gradient of the intensity. The second part is not familiar. It has the form of a covariant derivative, describing streamlines of the electric field. Like the gradient of intensity, the $(\mathbf{E}\cdot\nabla)\mathbf{E}^*$ contribution points toward regions of highest intensity. However, this term is polarization-dependent. Consequently, the difference between the intensity gradient and the $(\mathbf{E}\cdot\nabla)\mathbf{E}^*$ term represents only the polarization-dependent forces. The difference points toward high intensity regions. This is different than the spin-curl force and represents a distinct spin-dependent force.

Decomposing the force into its real and imaginary parts in Eq. (5.29), shows that spin-curl forces and other polarization-dependent forces have different coefficients, $\Re\{\alpha_e\alpha_m^*\}$ and $\Im\{\alpha_e\alpha_m^*\}$ respectively. Their associated force contributions therefore should not cancel in general.

A similar analysis of the force from the interference of the electric dipole and the electric quadrupole also yields spin-dependent forces. The expression for the force [31],

$$\mathbf{F}^{\mathrm{Qp}} = -\frac{k^5}{40\pi\epsilon_0}\Im\left\{Q\cdot\mathbf{p}^*\right\}, \tag{5.32}$$

can be expanded using the definition of the electric quadrupole polarizability, Eq. (5.23),

$$\mathbf{F}^{\mathrm{Qp}} = -\frac{k^5}{40\pi\epsilon_0}\left(\Im\left\{\gamma_e\alpha_e^*(\partial_n E_j + \partial_j E_n)\cdot E_n^*\right\}\right). \tag{5.33}$$

Further expansion yields

$$\begin{aligned}\mathbf{F}^{\mathrm{Qp}} = -\frac{k^5}{40\pi\epsilon_0}&\left(\Im\left\{\gamma_e\alpha_e^*\right\}\Re\{(\mathbf{E}^*\cdot\nabla)\mathbf{E}\} + \Im\left\{\gamma_e\alpha_e^*\right\}\Re\{E_n^*\nabla E_n\}\right.\\ &\left.+\Re\{\gamma_e\alpha_e^*\}\Im\left\{(\mathbf{E}^*\cdot\nabla)\mathbf{E}\right\} + \Re\{\gamma_e\alpha_e^*\}\Im\left\{E_n^*\nabla E_n\right\}\right),\end{aligned} \tag{5.34}$$

where each of the four terms have been identified previously. The first term is the covariant derivative-like term that leads to a polarization-dependent force that points towards regions of higher intensity. The second gives rise to a conventional intensity gradient force. The third leads to a spin-curl force, and the last one contributes to the phase-gradient force. Again these spin-dependent contributions to the optical force do not cancel out because of their distinctive dependence on the polarizabilities.

Spin-dependent forces thus arise from interference between different orders of multipole scattering. We have shown that this is true up to electric quadrupole order. Continuation to higher order seems likely.

5.5 Induced magnetization in non-magnetic materials

From the previous section, the spin-curl force requires not only an induced electric dipole moment, but also another induced multipole moment. The electric quadrupole polarizability of a dielectric sphere typically is much smaller than the electric dipole polarizability. One might expect, furthermore, that dielectric spheres would have no magnetic response. The spin-curl force therefore ought to be very small indeed, contrary to the experimental results reported in Chapter 4. In fact, the electric and magnetic response turn out to be coupled in colloidal spheres. The oscillating electric fields of the light polarizes the dielectric material. In turn, this time varying polarization acts as a source current for magnetic multipole moments. In this way, dielectric spheres can experience strong magnetic

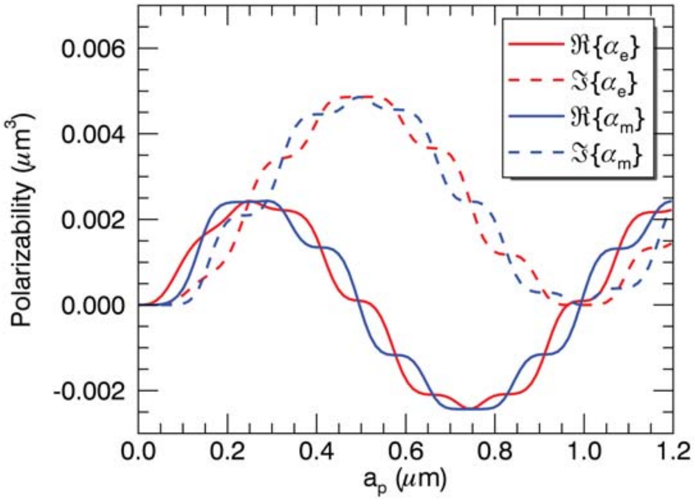

Figure 5.1: Polarizability versus radius, a_p, for polystyrene colloidal spheres in water.

forces due to Mie scattering.

Lorenz-Mie theory provides a way to exactly determine the strength of the electric and magnetic response at dipole order and beyond. Matching the boundary conditions at a particle's surface involves relating the incident and scattered fields by the a_n and b_n Mie coefficients. The first of these coefficients yield the electric and magnetic polarizability of the sphere [31],

$$\alpha_e = i\frac{6\pi\epsilon_0 n_m^2}{k^3}a_1 \quad \text{and} \quad \alpha_m = i\frac{6\pi}{\mu_0 k^3}b_1, \tag{5.35}$$

where a_1 and b_1 are the electric and magnetic Mie sphere coefficients at dipole order.

The behavior of these polarizabilities depends sensitively on particle size, and can have surprising properties. Fig. (5.1) shows the polarizability of polystyrene (PS) spheres as a function of sphere radius. There are large oscillations in both the electric and magnetic polarizability along with smaller more rapidly varying oscillations. The imaginary part of both polarizabilities is always nonnegative. This is reasonable since according to Eq. (5.21), the imaginary part of the polarizability is responsible for radiation pressure. Naturally, radiation pressure can only push. However the intensity gradient force can change sign because the real part of the polarizability can change sign. For some range of sizes, therefore, particles will be repelled from the region with the highest intensity. Such particles cannot easily be trapped by conventional optical traps.

The direction of $\mathbf{F}^{\text{p-m}}(\mathbf{r})$ in Eq. (5.29) can flip for certain values of the electric and magnetic polarizabilities. This effect was utilized by Chen *et al.* to predict the onset of an optical pulling force [31]. The dependence on the polarizabilities implies that this surprising pulling force should be very sensitive to the size of the particle. Recently Zemanek [152] showed experimentally that it is possible to pull dielectric spheres in crossed plane waves, and that this force is indeed very sensitive to particle size.

5.6 Generalized Lorenz-Mie theory

Although the previous sections give a good qualitative understanding of where each part of the optical force comes from, we need a more complete theory to obtain quantitative results for spheres in the Mie regime. This is clear from the perspective of the induced multipoles. For small spheres, only the first few induced multipoles moments are important, and the previous expressions for the optical force are accurate. For larger spheres, which we use experimentally, we need to take many multipole orders into consideration.

Generalized Lorenz-Mie theory [31, 38, 153–155] is a framework for analyzing the optical force while including all of the multipole orders. The idea is to decompose the incident field into a spherically symmetric basis that is centered on the particle. This allows the boundary conditions to be easily matched, which then determines the scattered and interior fields. The incident and scattered field can then be used to extract the optical force on the sphere. Although it is relatively easy to describe conceptually, it can be cumbersome to implement. Here we will describe the steps we use to calculate the optical force.

The first step is to expand the incident field as a series,

$$\mathbf{E}(\mathbf{r}) = E_0 \sum_{n=1}^{\infty} \sum_{m=-n}^{n} \left[a_{mn}(\theta_j)\, \mathbf{M}_{nm}^{(1)}(k\mathbf{r}) + b_{mn}(\theta_j)\, \mathbf{N}_{nm}^{(1)}(k\mathbf{r}) \right], \tag{5.36}$$

in the vector spherical harmonics, $\mathbf{M}_{nm}^{(1)}(k\mathbf{r})$ and $\mathbf{N}_{nm}^{(1)}(k\mathbf{r})$, that constitute the natural basis for transverse electric (TE) and transverse magnetic (TM) waves, respectively [132]. Finding the expansion coefficients, $a_{mn}(\theta_j)$ and $b_{mn}(\theta_j)$ is a non-trivial task, but many useful examples have been reported already. These coefficients, called the beam shape coefficients (BSCs), can be determined by the following integral [104],

$$a_{mn} = i\sqrt{\frac{4\pi}{2n+1}\frac{(n+m)!}{(n-m)!}}\frac{\int_0^{2\pi}\int_0^{\pi}\mathbf{E}\cdot\mathbf{M}_{nm}^{(1)}(k\mathbf{r})^*\sin\theta d\theta d\phi'}{\int_0^{2\pi}\int_0^{\pi}|\mathbf{M}_{nm}^{(1)}(k\mathbf{r})|^2\sin\theta d\theta d\phi'}, \tag{5.37}$$

And a similar one for b_{mn} with $\mathbf{N}_{nm}^{(1)}(k\mathbf{r})$ replacing $\mathbf{M}_{nm}^{(1)}(k\mathbf{r})$. Mackowski determined the coefficients for an arbitrary plane wave [156], which can be added up to create more complicated beams.

Next we write the associated expansion of the scattered field,

$$\begin{aligned}\mathbf{E}_s(\mathbf{r},t) = E_0\, e^{-i\omega t}\sum_{n=1}^{\infty}\sum_{m=-n}^{n}\big\{\left[r_{mn}(\theta_1)+e^{i\varphi(t)}r_{mn}(\theta_2)\right]\,\mathbf{M}_{nm}^{(3)}(k\mathbf{r})\\ +\left[s_{mn}(\theta_1)+e^{i\varphi(t)}s_{mn}(\theta_2)\right]\,\mathbf{N}_{nm}^{(3)}(k\mathbf{r})\big\}\,,\end{aligned} \tag{5.38}$$

by matching the boundary conditions for the electric and magnetic fields at the sphere's surface [31, 128, 131, 154, 155, 157]. The expansion coefficients,

$$r_{mn}(\theta_j) = -a_n\, a_{mn}(\theta_j) \quad \text{and} \tag{5.39a}$$

$$s_{mn}(\theta_j) = -b_n\, b_{mn}(\theta_j), \tag{5.39b}$$

are related to the expansion coefficients of the incident field by the standard Mie coefficients, a_n and b_n, [128], which depend on the radius and refractive index of the sphere. The ease of determining the scattered field at this stage provides the justification for taking the effort to write the incident field in terms of the vector spherical harmonics.

The final step is to calculate the force from the incident and and scattered fields, $\mathbf{E}(\mathbf{r}, t) + \mathbf{E}_s(\mathbf{r}, t)$. They contribute to the Maxwell stress tensor, $\mathbf{T}(\mathbf{r}, t)$, whose integral over a closed surface provides an estimate for the optically-induced force on a sphere centered at $\mathbf{r}$:

$$\mathbf{F}(\mathbf{r}, t) = \oint_S \hat{n} \cdot \mathbf{T}(\mathbf{r}', t) \, d\mathbf{r}', \tag{5.40}$$

where $\hat{n}$ is the unit normal to the surface S enclosing the sphere. In practice, the integral is computed directly from the combined expansion coefficients using established techniques [10, 120, 158, 159]. The expansion coefficients are calculated centered on the sphere, so we recalculate them as the sphere moves through the optical field.

Although we assume that the particle is a sphere, this is not necessary in generalized Lorenz-Mie theory. For non-spherical particles, the only difference is in the boundary conditions. Instead of the relation given by Eq. (5.39), the scattered field coefficients are determined by multiplying the incident field coefficients by the T-matrix that encapsulates the scattering properties of the particle (or cluster of particles) [130, 132]. Once we have the incident and scattered field then we can still apply Eq. (5.40) using the methods referenced above.

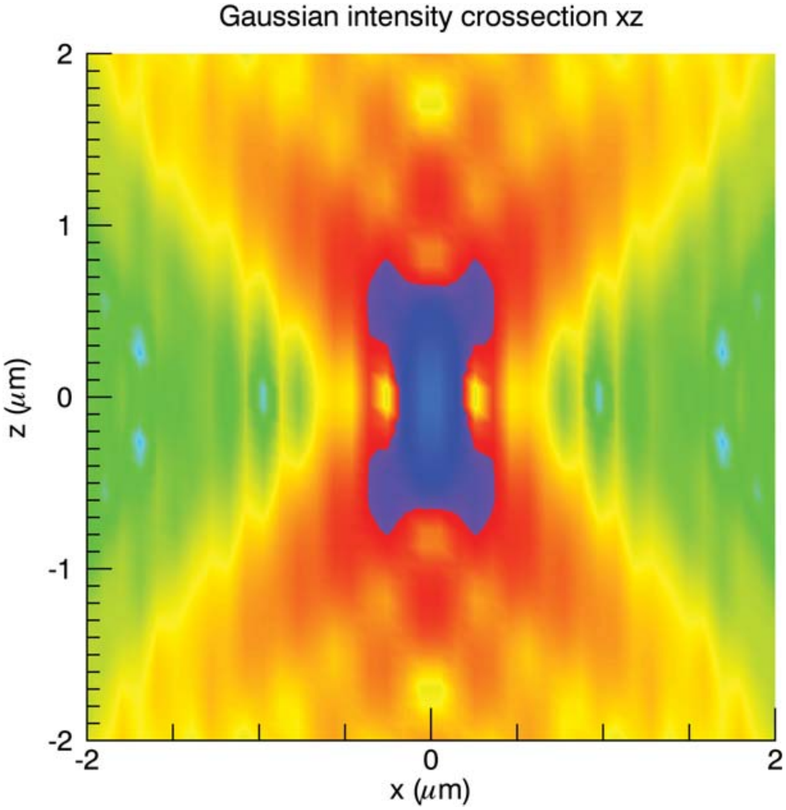

Figure 5.2: Cross section of focused circularly polarized Gaussian beam in the $x-z$ plane.

5.7 Calculation of spin curl force in circularly polarized beam

In the experiments described in Chapter 4, we found that isotropic dielectric spheres circulate around the axis of a circularly polarized beam. This evidence for a spin-curl force remains to be verified against theory. We saw in section 5.4 that a combination of electric and magnetic induced dipole moments can lead to spin-curl forces. However our experiments were done in the Mie regime and so should be interpreted with generalized Lorenz-Mie theory.

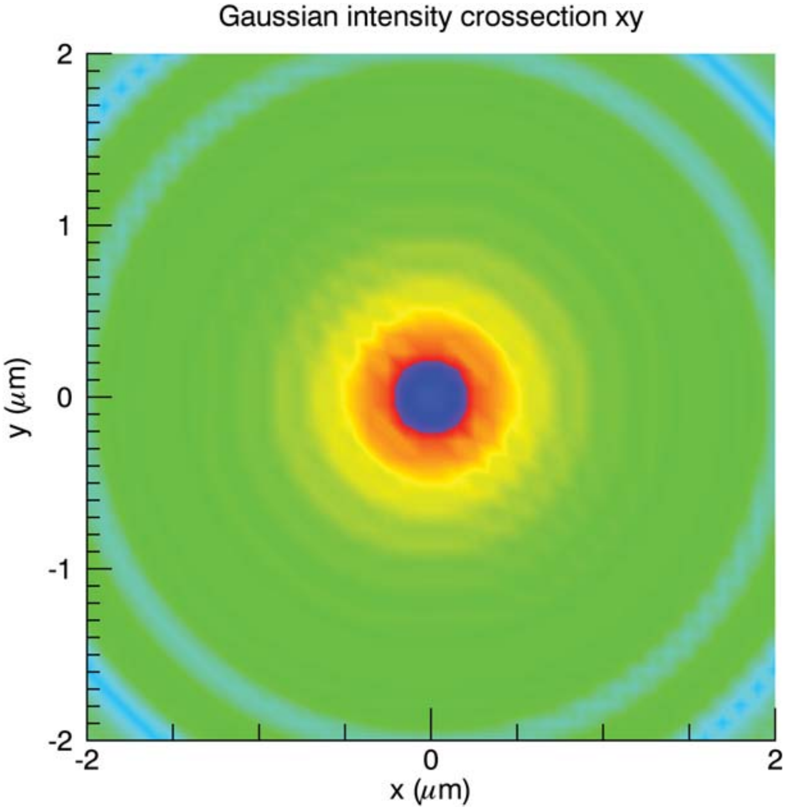

Figure 5.3: Cross section of focused circularly polarized Gaussian beam in the $x-y$ plane.

We model our circularly polarized optical tweezers as a focused vector Gaussian beam. We determine the BSCs for this beam from a superposition of Bessel beams, each with beam coefficients given by [153],

$$a_{mn}(\mathbf{r}) = E_0 \frac{4\pi i^n}{n(n+1)} e^{ikz\cos\theta_0} \left[\tilde{\pi}_{mn}(\cos\theta_0)\, I^+(\rho,\phi) + \tilde{\tau}_{mn}(\cos\theta_0)\, I^-(\rho,\phi)\right] \quad (5.41)$$

where $\rho = \sqrt{x^2+y^2}$ is the distance from the beam axis, and $\phi = \arctan(-y/x) - \pi/2$ is the azimuthal angle. We calculate b_{mn} similarly by exchanging the $\tilde{\tau}_{mn}$ with the $\tilde{\pi}_{mn}$ in Eq. (5.41). The angular functions may be expressed in terms of the

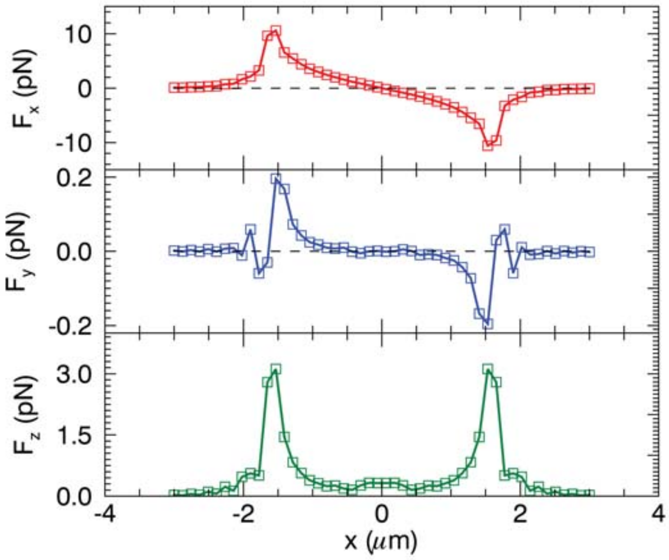

Figure 5.4: Force as a function of position in a circularly polarized optical tweezers at the beam waist. F_x, in red, represents the radial force, F_y, in blue, shows the azimuthal force, and F_z, in green, points along the optical axis. The azimuthal force arises from the curl of the optical spin angular momentum.

modified Legendre polynomials, P_n^m,

$$\tilde{\pi}_{mn}(\cos\theta_0) = \sqrt{\frac{2n+1}{4\pi}\frac{(n-m)!}{(n+m)!}}\frac{m}{\sin\theta_0}P_n^m(\cos\theta_0), \tag{5.42}$$

$$\tilde{\tau}_{mn}(\cos\theta_0) = \sqrt{\frac{2n+1}{4\pi}\frac{(n-m)!}{(n+m)!}}\frac{d}{d\theta_0}P_n^m(\cos\theta_0), \tag{5.43}$$

and finally the integrals,

$$I^{\pm}(\rho,\phi) = \pi\left[e^{i(m-1)\phi}J_{1-m}(k\sin\theta_0\rho) \pm e^{i(m+1)\phi}J_{-1-m}(k\sin\theta_0\rho)\right]. \tag{5.44}$$

The BSCs for the Bessel beam are complicated, however this form is much more useful than the integral in Eq. (5.37). All one has to do to calculate the BSCs is to evaluate Bessel functions and associated Legendre polynomials. The Gaussian beam can then be created from the superposition of these BSCs of the Bessel beams,

$$a_{mn} = U_n \int_0^{\theta_0} E'(\theta)[\tilde{\tau}_{mn}(\cos\theta_0)I^+(\rho,\phi) + \tilde{\pi}_{mn}(\cos\theta_0)I^-(\rho,\phi)]\sin\theta d\theta, \qquad (5.45)$$

where $E'(\theta) = (E_0 k^2 w_0^2/4\pi)\sqrt{\cos\theta}e^{-(\gamma\sin\theta)^2}e^{ikz\cos\theta}$ and θ_0 is the half-angle subtended by the objective at the beam focus. Additionally, w_0 is the width of the beam at the focus, and γ describes the width of the beam before it is focused by the objective.

The transverse and axial cross sections of the beam are shown in Fig. (5.3) and in Fig. (5.2) respectively. The transverse cross section is circularly symmetric because of the circular polarization. The force on a colloid in the tweezers is shown in Fig. (5.4), and we see that there is a non-zero azimuthal force. This is the spin-curl force. Furthermore, it is much smaller in magnitude than the gradient force in the radial direction, which is consistent with the low values for the circulation rate that we reported in our experiments.

Chapter 6

Experimental Demonstration of Conveyor Tractor Beams

6.1 Introduction to tractor beams

Tractor beams are traveling waves that transport illuminated objects back to their sources, opposite to the direction of energy flow. By this definition, optical tweezers [14] are not tractor beams because of their inherently limited range. Nor is an optical conveyor belt [37, 38], which is created from a standing wave rather than a traveling wave. A one-sided variant of the optical conveyor belt created from coaxial Bessel beams has been demonstrated, but relies on auxiliary forces to achieve retrograde motion [38]. Here, we demonstrate one-sided optical conveyors that act as tractor beams without requiring outside assistance. The same technique we use to project a single optical conveyor also can project arrays of optical conveyors each with independently controlled transport properties.

Most beams of light do not act as tractor beams because radiation pressure tends to drive illuminated objects downstream. Recently, however two categories of tractor beams have been described, both of which exploit properties of propagation-invariant or non-diffracting traveling waves [85], and thus have promise for long-range material transport. Both rely on the recoil force that an illuminated object experiences if it scatters transverse components of the beam's linear momentum density into the axial direction. The first is based on multipole scattering in Bessel beams, which has been predicted to drive retrograde motion in both acoustic [35] and optical [31] waves. Because this mechanism relies on scattering by high-order induced multipole moments, however, the direction of induced transport depends sensitively on the properties of the illuminated object; tractor beams based on pure Bessel modes have not yet been demonstrated experimentally. However this mechanism has been confirmed experimentally in a related system using interfering plane waves, and did exhibit sensitivity to particle size [152]. The other approach utilizes periodic axial intensity gradients in beams with discrete propagation invariance [85] to achieve forward scattering from the interference between the incident field and the dipole radiation field of an illuminated object. Such tractor beams have been realized experimentally with solenoidal waves, which have transported micrometer-scale colloidal spheres over an axial range of 10 µm [29].

6.2 Optical conveyor field

Here, we describe another category of tractor beams derived from the optical conveyor belts introduced in Refs. [36–38] that can be projected from a single source and can transport material bidirectionally without the aid of outside forces. A one-sided optical conveyor is formed by projecting two or more coherent Bessel beams along the same axis and systematically varying their relative phase. The vector potential for a two-component optical conveyor of frequency ω and polarization $\hat{\epsilon}$ may be written in cylindrical coordinates $\mathbf{r} = (r, \theta, z)$ as

$$\begin{aligned}\mathbf{A}_m(\mathbf{r}, t) = A_m \, \Big\{ J_m \left(\left[1 - \eta_1^2\right]^{\frac{1}{2}} kr \right) \, e^{i\,\eta_1 kz} \\ + \, \xi \, e^{i\varphi(t)} \, J_m \left(\left[1 - \eta_2^2\right]^{\frac{1}{2}} kr \right) \, e^{i\,\eta_2 kz} \Big\} \, e^{im\theta} \, e^{-i\omega t} \, \hat{\epsilon},\end{aligned} \tag{6.1}$$

where $k = n_m \omega / c$ is the wavenumber of light in a medium with refractive index n_m and $J_m(\cdot)$ is a Bessel function of the first kind of order m. The two beams differ in their axial wavenumbers, $\eta_1 k$ and $\eta_2 k$, which are reduced from k by factors $\eta_1, \eta_2 \in (0, 1)$. They also differ in their relative phase $\varphi(t)$, whose time variation makes the conveyor work. The prefactor A_m is the beam's amplitude. Setting the relative amplitude to unity, $\xi = 1$, maximizes the conveyor's axial intensity gradients and thus optimizes its performance for optical manipulation.

In the special case $m = 0$, $\xi = 1$, the component Bessel beams have unit amplitude along the optical axis, $r = 0$, and the conveyor's axial intensity is

$$\lim_{r \to 0} I(\mathbf{r}, t) = \frac{1}{2} \, c n_m \epsilon_0 \omega^2 \, \lim_{r \to 0} \left| \mathbf{A}_0(\mathbf{r}, t) \right|^2 \tag{6.2}$$

$$= I_0 \, \cos^2 \left(\frac{1}{2} \, \left[(\eta_1 - \eta_2) \, kz - \varphi(t) \right] \right), \tag{6.3}$$

where $I_0 = 2A_0^2 c n_m \epsilon_0 \omega^2$. The beam thus has intensity maxima at axial positions

$$z_j(t) = \left[j + \frac{\varphi(t)}{2\pi} \right] \, \Delta z \tag{6.4}$$

that are evenly spaced by multiples, $\Delta z = \lambda/(\eta_1 - \eta_2)$, of the wavelength $\lambda = 2\pi/k$ in the medium, and thus can be indexed by the integer j.

Objects trapped along $I(z,t)$ can be displaced either up or down the axis by appropriately varying the relative phase $\varphi(t)$. Continuous variations translate trapped objects deterministically along $\hat{z}$ with axial velocity

$$v(t) = \Delta z \frac{\partial_t \varphi(t)}{2\pi} \tag{6.5}$$

regardless of their size, shape, or optical properties. This differs from the action of Bessel-based tractor beams [35] in which even the sign of the induced motion depends on each object's properties. It differs also from the motion induced by solenoidal tractor beams [29] which is unidirectional but not uniformly fast.

6.3 Demonstration of optical conveyor tractor beam

6.3.1 Implementing the beam

We implemented optical conveyors using the holographic optical trapping technique [15, 70] in which a computer-designed phase profile is imprinted onto the wavefronts of a Gaussian beam, which then is projected into the sample with a high-numerical-aperture objective lens of focal length f. In practice, the trap-forming hologram is implemented with a computer-addressable spatial light modulator (SLM) (Hamamatsu X8267-16) that imposes a selected phase shift at each

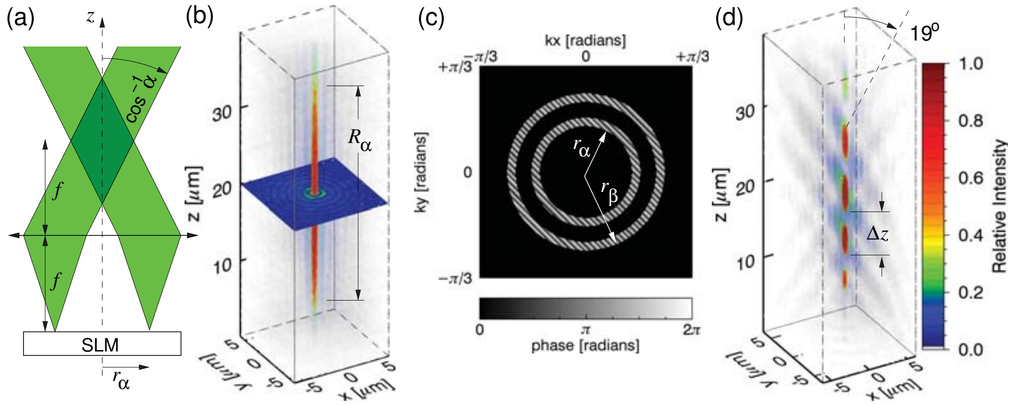

Figure 6.1: (a) Schematic representation of holographic projection of a Bessel beam with axial wavenumber $\eta_1 k$ by a lens of focal length f. Shaded region indicates volume of invariant propagation. (b) Volumetric reconstruction of a holographically projected Bessel beam. (c) Phase hologram encoding an optical conveyor. Diagonal blazing tilts the projected conveyor away from the optical axis. (d) Volumetric reconstruction of the beam projected by the hologram in (c). The color bar indicates relative intensities in (b) and (d). Figure from Ref. [12].

pixel in a 768 × 768 array. If the field described by Eq. (6.1) is to be projected into the objective's focal plane, the field in the plane of the hologram is given in the scalar diffraction approximation [114] by its Fourier transform,

$$\tilde{\mathbf{A}}_m(\mathbf{r},t) = i^{m+1}\,\frac{f}{k}\,A_m\,e^{im\theta}\,e^{-i\omega t}\left[\frac{1}{r_{\eta_1}}\,\delta\left(r - r_{\eta_1}\right) + \xi\,e^{i\varphi(t)}\,\frac{1}{r_{\eta_2}}\,\delta\left(r - r_{\eta_2}\right)\right]\hat{\epsilon}, \quad (6.6)$$

where $\delta(\cdot)$ is the Dirac delta function, $r_{\eta_1} = f\,(1-\eta_1^2)^{\frac{1}{2}}$ and $r_{\eta_2} = f\,(1-\eta_2^2)^{\frac{1}{2}}$, The ideal hologram for each Bessel beam comprising the conveyor thus is a thin ring in the plane of the SLM, as indicated schematically in Fig. 6.1(a). A holographically projected Bessel beam then propagates without diffraction over the range indicated by the shaded region. Increasing the transverse wave number increases the radius of the hologram and therefore reduces the non-diffracting range.

Figure 6.1(b) shows a volumetric reconstruction [160] of a Bessel beam projected with a ring-like hologram. Increasing the ring's thickness of the ring by $\pm\Delta r$ increases diffraction efficiency, but is equivalent to superposing Bessel beams with a range of axial wavenumbers, $\Delta\eta_1 = r_{\eta_1}\Delta r_{\eta_1}/(\eta_1 f^2)$. This superposition contributes an overall axial envelope to the projected Bessel beam, limiting its axial range to $R_{\eta_1} = 2\lambda/\Delta\eta_1$. The axial range in Fig. 6.1(b) is consistent with this estimate and so is smaller than the ray-optics estimate suggested by the overlap volume in Fig. 6.1(a).

Figure 6.1(c) shows the two-ringed phase-only hologram that encodes an optical conveyor with an overall cone angle of $\cos^{-1}([\eta_1 + \eta_2]/2) = 19°$. This function corresponds to the phase of the beam's vector potential, which the SLM imprints on an incident Gaussian plane wave. The relative phase offset between the two rings determines $\varphi(t)$. The relative widths of the two phase rings can be used to establish the components' relative amplitudes through $\xi = r_{\eta_2}^2\,\Delta r_{\eta_2}/(r_{\eta_1}^2\,\Delta r_{\eta_1})$, the range of the projected conveyor then being the smaller of R_{η_1} and R_{η_2}.

The large featureless regions in Fig. 6.1(c) do not contribute to the desired optical conveyor. Light passing through these regions is not diffracted and therefore converges at the focal point of the optical train. To prevent interference between the diffracted and undiffracted beams, the two phase rings contributing to the conveyor are offset and blazed with a linear phase gradient. This phase gradient deflects the diffracted light [115] causing the projected Bessel beams to focus 24 µm from the optical axis.

The volumetric reconstruction in Fig. 6.1(d) shows the three-dimensional intensity distribution projected by the hologram in Fig. 6.1(c), with $\hat{z}$ oriented along the diffracted beam's direction of propagation. This beam clearly displays the pattern of periodically alternating bright and dark regions predicted by Eqs. (6.1) through (6.4).

The unused regions of the hologram need not go to waste. They can be used to project additional independent conveyors, much as has been demonstrated for spatially multiplexed optical traps of other types [11,113,161]. An appropriately designed array of conveyors therefore can make full use of the light falling on the SLM and thus can be projected with very high diffraction efficiency. Each conveyor, moreover, can be operated independently of the others by selectively offsetting the phase in appropriate regions of the multiplexed hologram.

6.3.2 Bi-directional tractor action

The data in Fig. 6.2 were obtained with two separate optical conveyors projected simultaneously with equal intensity and equal axial period by a single hologram. The conveyors' phases were ramped at the same rate, but with opposite sign. This single structured beam of light therefore should transport material in opposite directions simultaneously. To demonstrate this, we projected the pair of conveyors into a sample of 1.5 µm diameter colloidal silica spheres dispersed in water (Polysciences, Lot # 600424). The sample is contained in the 100 µm deep gap between a clean glass microscope slide and a cover-slip that was formed by and sealed with UV-curing optical adhesive (Norland 68). The slide was mounted on the stage of a Nikon TE-2000U optical microscope outfitted with a custom-built holographic optical trapping system [162] operating at a vacuum wavelength of $\lambda_0 = 532\,\mathrm{nm}$. An estimated 17 mW of linearly polarized light were projected into

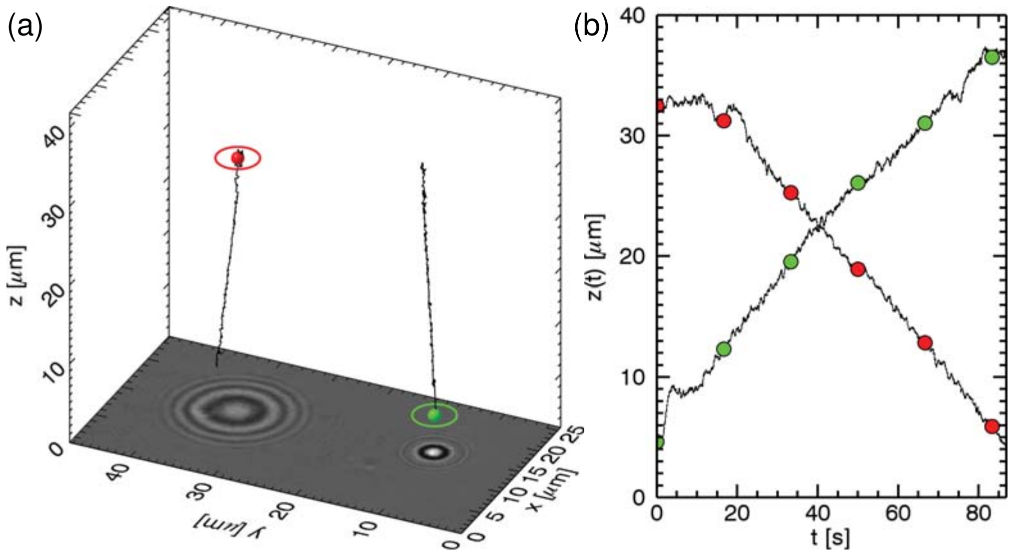

Figure 6.2: (a) Trajectories of two 1.5 μm diameter colloidal silica spheres moving along a pair of optical conveyors, superimposed with a holographic snapshot of the two spheres. Colored orbs indicate the spheres' positions in the hologram, and are plotted at the same scale as the actual spheres. Rings are added for emphasis. (b) Measured time dependence of the spheres' axial positions as one moves downstream ($+\hat{z}$) along its conveyor and the other moves upstream ($-\hat{z}$). Figure adapted from Ref. [12].

each conveyor with a 100× numerical aperture 1.4 oil-immersion objective lens (Nikon Plan-Apo DIC H) at an overall efficiency of 0.5 percent.

To facilitate tracking the spheres as they move along the optical axis, the microscope's conventional illuminator was replaced with a 10 mW 3 mm-diameter collimated laser beam at a vacuum wavelength of 447 nm . Interference between light scattered by the spheres and the rest of the illumination forms a hologram of the spheres in the focal plane of the objective lens that is magnified and recorded at 30 frames per second with a conventional greyscale video camera (NEC TI-324A-II). A typical holographic snapshot is reproduced in Fig. 6.2(a). These holograms then can be analyzed [9,163,164] to obtain the spheres' three-dimensional positions with nanometer-scale resolution. The traces in Fig. 6.2(a) show the full trajectories of both spheres over the course of the experiment. Colored orbs indicate the measured positions of the spheres at the instant of the holographic snapshot and are scaled to represent the actual sizes of the spheres. Starting from the configuration in Fig. 6.2(a), the two conveyors were run through total phase ramps of $\pm 10\pi$ in steps of $\pi/4$, yielding the axial trajectories plotted in Fig. 6.2(b). Reversing the phase ramps reverses the process. These measurements confirm that arrays of optical conveyors can selectively induce bidirectional transport over their entire lengths.

6.3.3 Self-healing

The self-healing nature of Bessel beams [85, 87] furthermore suggests that multiple objects can be trapped and moved by a single optical conveyor despite light scattering by each of the trapped objects [37, 38, 38]. This is confirmed by Fig. 6.2(c), which shows a volumetric reconstruction [9, 103] of the light scattered by two colloidal spheres simultaneously trapped on an optical conveyor. The plotted intensity distribution was computed from the inset hologram by Rayleigh-Sommerfeld back-propagation. Maxima representing the positions of the spheres are separated by two periods of the underlying optical conveyor.

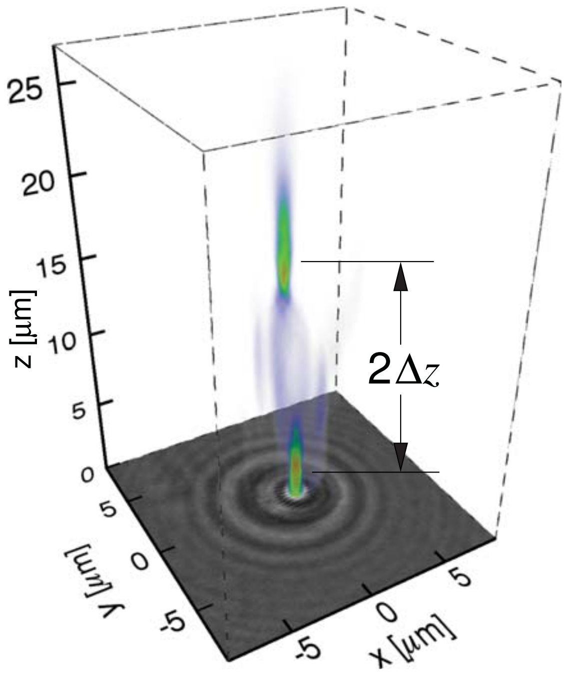

Figure 6.3: Three-dimensional reconstruction of a holographic snapshot of two colloidal spheres moving along a single optical conveyor. Figure adapted from Ref. [12].

6.4 Discussion

To characterize and optimize the transport properties of optical conveyors, we model the forces they exert in the Rayleigh approximation, which is appropriate for objects smaller than the wavelength of light. This provides a qualitative description of the physics of optical conveyors even though the colloidal microparticles in our experiment are technically too large to satisfy the Rayleigh approximation. Considering both induced-dipole attraction and radiation pressure, the axial component of the force is

$$F(z,t) = a\,\partial_z I(\mathbf{r},t) + b\,I(\mathbf{r},t), \tag{6.7}$$

where the coefficients $a = \Re\{\alpha_e\}/(4\epsilon_0 c)$ and $b = \Im\{\alpha_e\}(\eta_1+\eta_2)k/(4\epsilon_0 c)$ parametrize the light-matter interaction for a particle with electric polarizability α_e. As described in Section 5.1, this approximation omits contributions due to the curl of the spin density [8], and thus is appropriate for linearly polarized light. Further assuming a conveyor of the form described by Eq. (6.2) with continuously ramped phase, $\varphi(t) = \Omega t$, the equation of motion for a colloidal particle with drag coefficient γ is

$$\frac{\dot{z}(t)}{u_0} = \sqrt{1+\xi^2}\sin\left(2\pi\frac{z(t)}{\Delta z} + \Omega t - \cot^{-1}\xi\right) + 1, \tag{6.8}$$

where $u_0 = I_0 b/(2\gamma)$ is the downstream drift speed due to radiation pressure, and where $\xi = 2\pi a/(b\,\Delta z)$ describes the relative axial trapping strength. Particles that are trapped by intensity gradients are translated upstream with the conveyor's phase velocity, $\dot{z}(t) = -v_0 = -\Delta z\,\Omega/(2\pi)$. From Eq. (6.8), the maximum upstream transport speed is then limited by viscous drag to

$$v_0 \leq u_0\sqrt{1+\xi^2} - u_0 = \frac{I_0 b}{2\gamma}\left[\sqrt{1+\left(\frac{2\pi a}{b\Delta z}\right)^2} - 1\right]. \tag{6.9}$$

This remarkable result suggests that an optical conveyor can act as a tractor beam for any particle with $|a| > 0$ provided that it is not run too fast. Both light-seeking ($a > 0$) and dark-seeking ($a < 0$) particles should move in the same direction with the same speed, though the dark-seeking particles will sit in the beam's minima. Optical conveyors thus have the potential to out-perform optical tweezers, which cannot always achieve stable axial trapping even in the Rayleigh regime.

Equation (6.9) also suggests straightforward optimization strategies for optical conveyors. Brighter conveyors can run faster. Reducing the conveyor's spatial period Δz proportionately increases the maximum transport rate at the cost of reducing the maximum range.

Higher-order conveyors with $m > 0$ also have intensity maxima at positions z_j given by Eq. (6.4). They differ from zero-order conveyors in that their principal maxima are displaced from $r = 0$ to transverse radii that depend on m, η_1, and η_2. This larger transverse range may be useful for conveying irregular or asymmetrically shaped objects, or objects with inhomogeneous optical properties. Higher-order conveyors also carry orbital angular momentum and so will exert torques on trapped objects.

The transport direction predicted by Eq. (6.8) reverses sign in the limit of large Ω, illuminated objects then traveling steadily downstream at the drift speed u_0. The crossover between upstream and downstream transport is marked by a dynamical state in which the particle alternately is transported upstream and slips back downstream. The transition to this state is established by Eq. (6.9) in the deterministic case described by Eq. (6.8). It will be strongly affected by thermal fluctuations, however, and may feature anomalous velocity fluctuations. Still other dynamical states are possible if the relative phase $\varphi(t)$ varies discontinuously, for example in a Brownian ratchet protocol [165–167]. Even more complicated behavior may be expected for optical conveyor transport in underdamped systems for which inertia plays a role.

Chapter 7

Trapping properties of optical conveyors

7.1 Introduction: optical conveyors

Chapter 6 introduces optical conveyors and demonstrates their utility as practical realizations of tractor beams. Among the more surprising proposals arising from these initial studies is that optical conveyors might act as universal tractor beams, transporting small objects at uniform speed regardless of their composition [8]. This contrasts with the performance of conventional optical tweezers, which can only trap bright-seeking objects over a limited domain of size, shape and composition [10, 120, 158]. Another surprising suggestion is that optical conveyors might exceed the trapping stiffness even of diffraction-limited optical tweezers because their intensity actually vanishes at regular intervals along the optical axis [8].

Here we use the theory of photokinetics developed in Chapters 2 and 5 to look more closely at the trapping characteristics of these interesting modes of light. We report the results of a head-to-head comparison between the trapping characteristics of optical tweezers and optical conveyors involving both experimental measurements on micrometer-scale spheres and also numerical evaluations of optical forces using the generalized Lorenz-Mie theory. In confirming the superior performance of optical conveyors, these studies also enable us to establish the axial range over which optical conveyors can usefully transport material, and provide guidance for developing long-ranged tractor beams.

The electric field of a monochromatic optical conveyor of angular frequency ω, linearly polarized along $\hat{x}$ and propagating along $\hat{z}$ through a medium of refractive index n_m, is the superposition of two Bessel beams [8, 37, 38],

$$\mathbf{E}(\mathbf{r},t) = \frac{1}{2}\,E_0 e^{-i\omega t}\,\left[\mathbf{b}_1(k\mathbf{r}) + e^{i\varphi(t)}\mathbf{b}_2(k\mathbf{r})\right], \tag{7.1}$$

each of which may be described as a conical superposition of plane waves [38],

$$\mathbf{b}_j(k\mathbf{r}) = \int_0^{2\pi} \hat{\epsilon}(\theta_j,\phi)\, e^{i\mathbf{k}(\theta_j,\phi)\cdot\mathbf{r}}\, d\phi, \tag{7.2a}$$

where

$$\hat{\epsilon}(\theta,\phi) = \cos\phi\,\hat{\theta} + \sin\phi\,\hat{\phi} \tag{7.2b}$$

is the polarization of a plane wave incident on the optical axis at polar angle θ and azimuthal angle ϕ, and where

$$\mathbf{k}(\theta,\phi) = k(\sin\theta\cos\phi\,\hat{x} + \sin\theta\sin\phi\,\hat{y} + \cos\theta\,\hat{z}) \tag{7.2c}$$

is the corresponding wave vector. In the paraxial approximation, which is appropriate for long-range tractor beams, Eq. (7.2) reduces to

$$\mathbf{b}_j(k\mathbf{r}) \approx J_0\Big(\sqrt{1-\eta_j^2}kr\Big)\, e^{i\eta_j kz}\,\hat{x}, \tag{7.3}$$

where η_j is related to the Bessel beam's cone angle by $\eta_j = \cos\theta_j$. This is consistent with Eq. (6.1) used previously to qualitatively explain the properties of the optical conveyor beam. The approximate expression in Eq. (7.3) differs from the exact expression in Eq. (7.2) by terms involving higher-order Bessel functions [31, 168], which vanish on the optical axis. The numerical results developed in Sec. 5.6 are based on Eq. (7.2). Analytical results developed in Sec. 7.2.2 are more readily obtained from the approximation in Eq. (7.3).

The two Bessel beams comprising an optical conveyor share the same amplitude E_0, frequency ω and polarization along $\hat{x}$, but differ in their relative phase, $\varphi(t)$, and also in their axial wave numbers, $\eta_j k$, which are reduced from the plane wave value, $k = n_m\omega/c$, by the dimensionless factor $\eta_j \in (0,1]$. Here, c is the speed of light in vacuum. The superposition is usefully characterized by the mean convergence factor $\eta = (\eta_1+\eta_2)/2$ and the difference $\Delta\eta = |\eta_1-\eta_2|$. The upper limit of an optical conveyor's range, R, is set by the non-diffracting range of the most strongly converging Bessel beam [85],

$$R \leq A\cot\theta_1 = A\frac{\eta_1}{\sqrt{1-\eta_1^2}} \tag{7.4}$$

where A is the radius of the beam's aperture. Longer ranges can be achieved with values of η approaching 1.

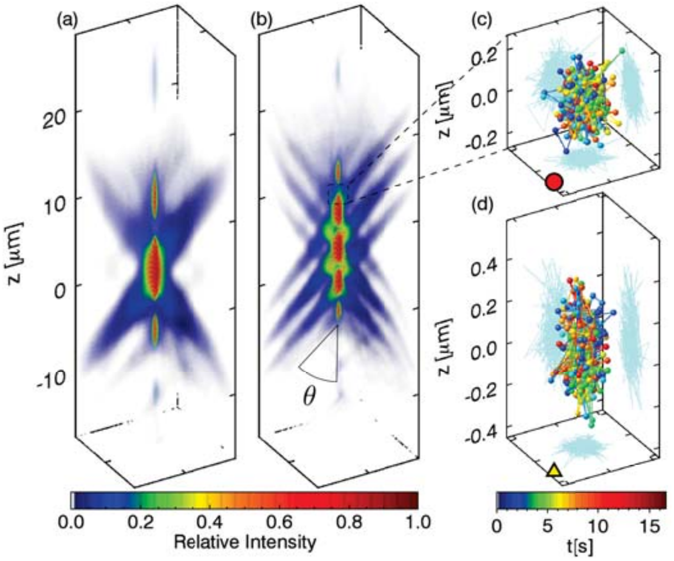

Figure 7.1: (a) Experimental reconstruction of an optical conveyor $\eta = 0.8$, $\Delta\eta = 0.04$, and (b) $\eta = 0.8$, $\Delta\eta = 0.086$. (c) Measured trajectory of a 1.5 μm-diameter silica sphere trapped in one of the intensity maxima in (b). (d) Trajectory of the same particle trapped in a conventional optical tweezers projected by the same instrument with the same peak intensity. Figure adapted from Ref. [13].

Figures 7.1(a) and 7.1(b) show the measured [160] three-dimensional intensity distribution of optical conveyors with equal values of η and differing values of $\Delta\eta$ that were projected with the holographic optical trapping technique [8, 15], which is described in general in section 3.2 and in particular for optical conveyors in section 6.3. These beams were powered by a linearly polarized diode-pumped solid-state laser (Coherent Verdi) operating at a vacuum wavelength of $\lambda = 532\,\mathrm{nm}$ that was shaped by a liquid crystal spatial light modulator (Holoeye Pluto) before being projected with a microscope objective lens (Nikon Plan-Apo, 100×, numerical aperture 1.4, oil immersion). The mode projected by this method is not the simple superposition of Bessel beams, but rather incorporates contributions from

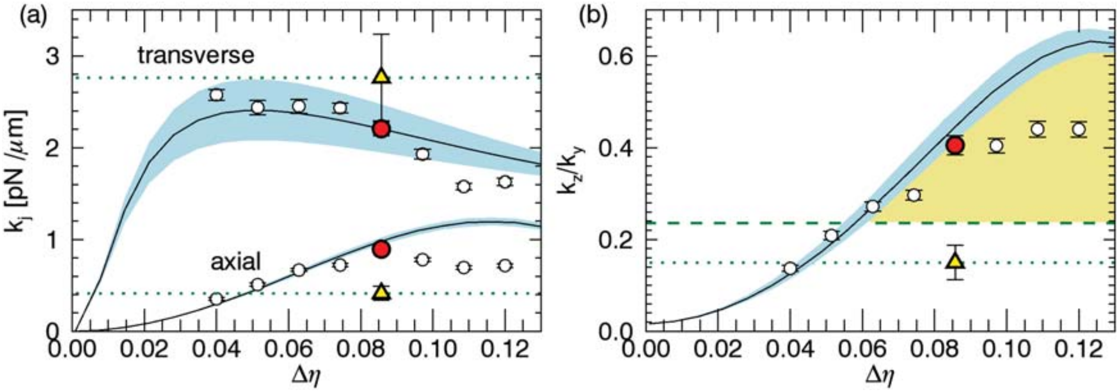

Figure 7.2: (a) Measured transverse and axial stiffness as a function $\Delta\eta$. (b) Stiffness ratio, k_z/k_r, as a function of $\Delta\eta$. Solid curves in (a) and (b) represent predictions of the Lorenz-Mie theory. Shaded bands represent uncertainty in the measured size and refractive index of the trapped silica sphere. Highlighted plot symbols represent results from Fig. 7.1(c) and (d). Dotted horizontal lines represent the measured performance of the optical tweezers. The dashed horizontal line in (b) shows the theoretical limit for optical tweezers performance. The shaded region above this line represents the optical conveyor's superior performance for optical micromanipulation. Figure adapted from Ref. [13].

small range of axial wave numbers around $\eta_j k$ [8]. Equation (7.1) therefore should be considered an idealized model for the actual beam.

The intensity distribution, $I(\mathbf{r},t) = \frac{1}{2} n_m \epsilon_0 c \left|\mathbf{E}(\mathbf{r},t)\right|^2$, has maxima at axial positions

$$z_n(t) = \frac{2\pi n + \varphi(t)}{\Delta\eta\, k}, \tag{7.5}$$

each of which can act as an optical trap for a small object. Here, ϵ_0 is the permittivity of space. Varying $\varphi(t)$ as a function of time moves these extrema, and thus conveys trapped objects along the beam. Increasing $\Delta\eta$ reduces the spacing between maxima, as shown in Figs. 7.1(a) and 7.1(b), and so provides control over the optical force profile.

7.2 Trap stiffness

We previously proposed, in Chapter 6, that optical conveyors should make better traps than conventional optical tweezers because their intensity vanishes altogether between maxima. The data in Figs. 7.1(c) and 7.1(d) demonstrate this to be true. Figure 7.1(c) shows the measured trajectory of a colloidal silica sphere diffusing through water in one of the potential energy wells of the static optical conveyor from Fig. 7.1(b). The optical conveyor has a peak intensity of $79\,\mathrm{mW\,\mu m^{-2}}$, as measured with imaging photometry. Holographic characterization [129, 135, 163], described in Section 3.3, reveals the sphere's radius to be $a_p = 0.730 \pm 0.005\,\mathrm{\mu m}$, and its refractive index to be $n_p = 1.424 \pm 0.005$. Holographic tracking [163, 169] yields the sphere's position with 1 nm precision in-plane and 3 nm resolution axially [135,170] at 16.7 ms intervals. Figure 7.1(d) shows the same sphere diffusing in a conventional optical tweezers with the same peak intensity projected by the same instrument.

In both cases, the trapped particle explores the optical force landscape under the influence of random thermal forces. The optical conveyor restricts the particle's axial excursions to less than half the range of the optical tweezers, resulting in a nearly isotropic trajectory. This suggests that an optical conveyor makes a substantially stiffer trap, even though the 2.8:1 aspect ratio of the optical tweezers' trajectory approaches the theoretical limit for a diffraction-limited Gaussian trap [171].

Modeling the traps as cylindrically symmetric harmonic potential energy wells,

$$U(\mathbf{r}) = \frac{1}{2}k_r r^2 + \frac{1}{2}k_z z^2, \tag{7.6}$$

we may estimate the transverse and axial trap stiffness, k_r and k_z from the particle's trajectory using thermal fluctuation analysis [162,172]. These measurements are performed for fixed values of the relative phase, $\varphi(t)$, so that the optical traps do not move during the measurement. For the trajectory in Fig. 7.1(c), we obtain $k_r = 2.2 \pm 0.1\,\mathrm{pN\,\mu m^{-1}}$ and $k_z = 0.89 \pm 0.03\,\mathrm{pN\,\mu m^{-1}}$, and an anisotropy of $\sqrt{k_r/k_z} = 1.57 \pm 0.04$. The equivalent results for the optical tweezers are $k_r = 2.8 \pm 0.4\,\mathrm{pN\,\mu m^{-1}}$, $k_z = 0.41 \pm 0.08\,\mathrm{pN\,\mu m^{-1}}$ and $\sqrt{k_r/k_z} = 2.6 \pm 0.4$. The optical conveyor performs as well as the optical tweezers in the transverse direction and is nearly twice as stiff along the axis.

The performance of single beam optical traps typically is limited by their axial trapping ability. Figure 7.1(e) shows how the optical conveyor's stiffness varies with $\Delta\eta$ for fixed η, and compares this with the performance of a diffraction-limited optical tweezers. Highlighted points correspond to the data from Figs. 7.1(c) and 7.1(d). The optical conveyor's axial stiffness exceeds that of a diffraction-limited optical tweezers by as much as a factor of two. This advantage is emphasized by the ratio between axial and transverse stiffness plotted in Fig. 7.1(f). Dashed horizontal dashed lines represent the measured and theoretical maximum performance of a Gaussian optical tweezers. Optical conveyors exceed this performance for $\Delta\eta > 0.06$, which corresponds to an axial period less than 6.7 µm.

7.2.1 Generalized Lorenz-Mie theory

Optical conveyors' superior trapping performance is consistent with predictions of generalized Lorenz-Mie theory [31, 38, 153–155], which are plotted as continuous curves in Figs. 7.1(e) and 7.1(f). For these calculations, each Bessel beam is expanded as a series,

$$\mathbf{b}_j(\mathbf{r}) = \sum_{n=1}^{\infty} \sum_{m=-n}^{n} \left[a_{mn}(\theta_j)\, \mathbf{M}^{(1)}_{nm}(k\mathbf{r}) + b_{mn}(\theta_j)\, \mathbf{N}^{(1)}_{nm}(k\mathbf{r}) \right], \tag{7.7}$$

in the vector spherical harmonics, $\mathbf{M}^{(1)}_{nm}(k\mathbf{r})$ and $\mathbf{N}^{(1)}_{nm}(k\mathbf{r})$, that constitute the natural basis for transverse electric (TE) and transverse magnetic (TM) waves, respectively [132]. The expansion coefficients, $a_{mn}(\theta_j)$ and $b_{mn}(\theta_j)$, have been reported previously for individual Bessel beams [153], and their functional form is described in Eq. (5.41).

The BSCs can be superimposed according to Eq. (7.1) to create an optical conveyor with specified values of η, $\Delta\eta$ and relative phase $\varphi(t)$. The force on the particle is then calculated according to established techniques [10, 120, 158, 159] described in Section 5.6. This calculation must also be repeated for each value of the relative phase $\varphi(t)$.

A trap's position, $\mathbf{r}_0(t)$, for a given value of $\varphi(t)$ is calculated numerically as a solution of $\mathbf{F}(\mathbf{r}_0(t), t) = 0$. The trap's effective stiffness along $\hat{r}_\nu$ then is calculated as

$$k_\nu = -\left. \partial_\nu F_\nu(\mathbf{r}, t) \right|_{\mathbf{r}=\mathbf{r}_0(t)}. \tag{7.8}$$

Results for the predicted transverse and axial stiffness are plotted in Fig. 7.1(e) for conveyor beams with $\eta = 0.8$ and $\Delta\eta$ ranging up to 0.13, and for values of the sphere's radius and refractive index obtained with holographic microscopy. The curves are scaled to a maximum intensity of $41\,\mathrm{mW\,\mu m^{-2}}$, which is less than the measured value presumably because holographically projected Bessel beams are not uniformly bright. This discrepancy does not affect the computed ratio of stiffnesses in Fig. 7.1(f), which also agree well with experimental results, with no adjustable parameters.

7.2.2 Dipole approximation

Generalized Lorenz-Mie theory is useful for computing the forces on specific particles in particular traps. To assess trends in optical traps' capabilities, we invoke the dipole approximation in which the time-averaged force [147, 148],

$$\mathbf{F}(\mathbf{r},t) = \frac{1}{2}\Re\left\{\alpha_e \sum_{\nu=1}^{3} E_\nu(\mathbf{r},t)\nabla E_\nu^*(\mathbf{r},t)\right\}, \tag{7.9}$$

is proportional to the object's polarizability $\alpha_e = \alpha_e' + i\alpha_e''$. This is equivalent to Eq. (5.2), which was written in terms of the vector potential. The polarizability of a dielectric sphere is related to its size and refractive index by the Clausius-Mossotti-Draine relation [173]

$$\alpha_e = \frac{4\pi\epsilon_0 n_m^2 K\, a_p^3}{1 - i\frac{2}{3}Kk^3a_p^3}, \tag{7.10}$$

where $K = (n_p^2 - n_m^2)/(n_p^2 + 2n_m^2)$ is the Lorentz-Lorenz factor. Absorptivity increases the imaginary part of α_e. Conductivity contributes an imaginary part to K. The dipole approximation typically applies in the Rayleigh limit, for particles much smaller than the wavelength of light.

An object near the axis of an optical conveyor experiences an axial force

$$\frac{F_z(\mathbf{r},t)}{E_0^2} \approx -\frac{1}{4}\alpha_e' \Delta\eta \, \sin\big(\Phi(z,t)\big) + \alpha_e'' \, \eta \, \cos^2\left(\frac{1}{2}\Phi(z,t)\right) \tag{7.11}$$

and a transverse force

$$\frac{F_r(\mathbf{r},t)}{E_0^2} \approx \alpha_e' \, \frac{1}{2}\left(1 - \eta^2 - \frac{1}{4}\Delta\eta^2\right) \, kr \, \cos^2\left(\frac{1}{2}\Phi(z,t)\right) + \frac{1}{4}\alpha_e'' \, \eta \, \Delta\eta \, kr \sin\big(\Phi(z,t)\big), \tag{7.12}$$

where $\Phi(z,t) = \Delta\eta \, kz - \varphi(t)$, and where we have assumed $kr \ll 1$. These results are obtained by averaging over times long compared with the optical cycle but short compared with variations in $\varphi(t)$. The particle is trapped where the force vanishes, which occurs at axial positions $Z_n(t)$ that are displaced from the intensity maxima by an amount that depends on the particle's light-scattering properties,

$$Z_n(t) - z_n(t) = \frac{2}{\Delta\eta k} \, \tan^{-1}\left(\frac{\alpha_e''}{\alpha_e'} \frac{2\eta}{\Delta\eta}\right). \tag{7.13}$$

Equations (7.8) and (7.14) then yield the traps' axial stiffness,

$$k_z = \frac{1}{4} \, |\alpha_e'| \, k E_0^2 \, \Delta\eta^2, \tag{7.14}$$

which is strictly positive. An optical conveyor thus can trap and transport any dipolar particle, regardless of its light-scattering characteristics. This universal, material-independent trapping capability does not require feedback [32] or fine tuning of the beam's properties [34]. Decreasing the inter-trap separation by increasing $\Delta\eta$ enhances intensity gradients and thus increases trap stiffness.

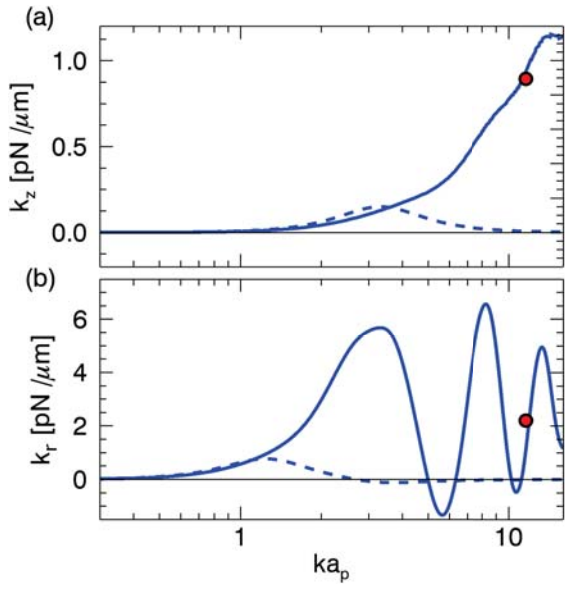

Figure 7.3: (a) Trap stiffness as a function of particle size for silica spheres in the optical conveyor from Fig. 7.1(b). Predictions from Lorenz-Mie theory are plotted as solid curves, and the corresponding results in the dipole approximation are plotted as dashed curves. Discrete points show experimental results obtained from the data in Fig. 7.1(c). Figure from Ref. [13].

Picking the largest possible value of $\Delta\eta$ to optimize axial trapping is not necessarily the best strategy. An optical conveyor's transverse stiffness,

$$k_r = k_z \frac{{\alpha_e'}^2 \left(1 - \eta^2 - \frac{1}{4}\Delta\eta^2\right) - 2{\alpha_e''}^2\eta^2}{\frac{1}{2}{\alpha_e'}^2 \Delta\eta^2 + 2{\alpha_e''}^2\eta^2}, \tag{7.15}$$

can vanish or even change sign as $\Delta\eta$ increases.

The dependence of trap stiffness on particle size predicted by Eqs. (7.10), (7.14) and (7.15) is plotted as dashed curves in Fig. 7.3 for silica spheres in an optical conveyor with $\eta = 0.8$ and $\Delta\eta = 0.086$. Results from the dipole approximation agree well with the Lorenz-Mie results that are plotted as solid curves in Fig. 7.3, at least for $ka_p \leq 1$. The Lorenz-Mie predictions, in turn, agree quantitatively with results from Fig. 7.1, which are plotted as discrete points.

The dipole approximation severely underestimates the optical conveyor's stiffness for $ka_p > 1$, and suggests that the particle studied in Fig. 7.1 would not have been stably trapped in the transverse direction. Rather than displaying a single crossover to instability, the generalized Lorenz-Mie result displays limited domains of instability for particles in particular size ranges. Results from the dipole approximation therefore are useful for establishing strict lower bounds on the performance of optical conveyors.

For example, requiring stable transverse trapping ($k_r > 0$) according to Eq. (7.15) establishes an upper bound on $\Delta\eta$ and, through Eq. (7.4), a lower bound on the range over which an optical conveyor can transport small objects:

$$R_\perp \leq \frac{A}{2}\left(\frac{\alpha_e'}{\alpha_e''} - \frac{\alpha_e''}{\alpha_e'}\right) < R. \tag{7.16}$$

The practically accessible range of transport may be substantially greater than $R_\perp$ for particles larger than the wavelength of light.

7.2.3 Comparison with optical tweezers

Conventional optical tweezers do not share optical conveyors' universal trapping ability. To show this, we model an optical tweezers as a focused Gaussian beam whose axial electric field profile is [14, 174]

$$\mathbf{E}_G(z,t) = E_0 \frac{z_R}{\sqrt{z^2 + z_R^2}} e^{ikz} e^{i\zeta(z)} e^{-i\omega t}\,\hat{\epsilon}, \tag{7.17}$$

where $z_R \approx 2R^2/(kA^2)$ is the Rayleigh range of a Gaussian beam converging at distance R from an aperture of radius A, and where $\zeta(z) = \tan^{-1}(z/z_R)$ is the Gouy phase. Because we are interested in long-ranged axial transport, we assume $R > A$. The axial component of the associated force,

$$\frac{F_G(z)}{E_0^2} = -\frac{1}{2} z_R^2 \, \frac{z\alpha_e' - k\left(z^2 - z_R^2\right)\alpha_e''}{\left(z^2 + z_R^2\right)^2}, \tag{7.18}$$

forms a trap only for particles satisfying

$$\left(\frac{\alpha_e'}{\alpha_e''}\right)^2 > 4kz_R(kz_R - 1). \tag{7.19}$$

This condition is most easily satisfied in strongly converging beams for which z_R is small. The condition on α_e is qualitatively consistent with numerical studies [10, 120, 158] which describe the difficulty of trapping high index or absorbing particles with laser tweezers.

7.3 Transport range

The ultimate rate of an optical conveyor is limited by the non-diffracting range of the constituent Bessel beams. Equation (7.19), by contrast, establishes an inherent upper limit on an optical tweezers' range

$$R_G = \frac{A}{2}\sqrt{1 + \sqrt{1 + \left(\frac{\alpha_e'}{\alpha_e''}\right)^2}}. \tag{7.20}$$

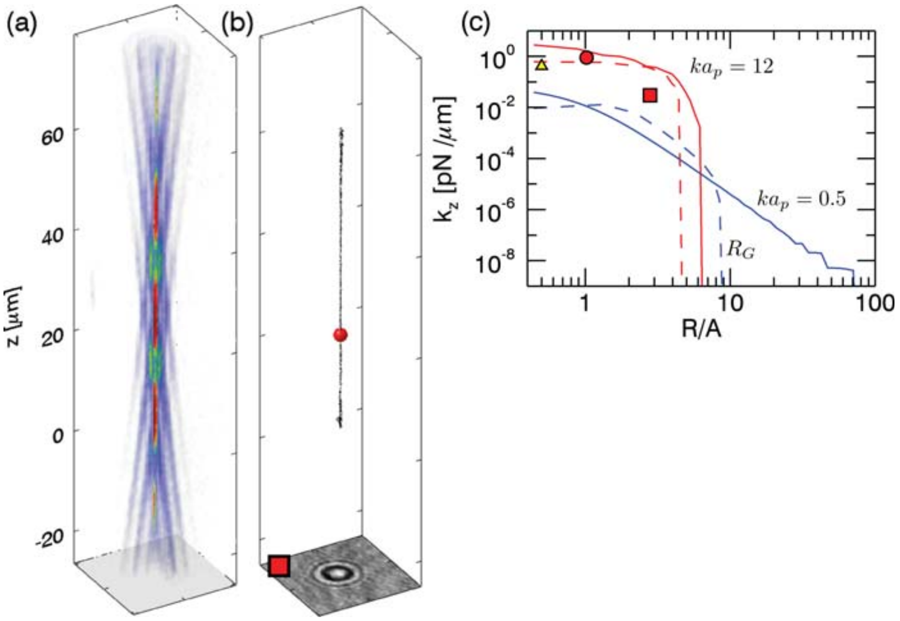

Figure 7.4: (a) Experimental reconstruction of an optical conveyor with $\eta = 0.96$ and $\Delta\eta = 0.04$. (b) Trajectory of a 1.5 µm silica sphere transported by the same optical conveyor over a range of 66 µm. (c) Axial stiffness as a function of transport range. Solid curves show Lorenz-Mie predictions for optical conveyors transporting large (1.5 µm-diameter) and small (0.036 µm-diameter, $ka_p = 0.5$) silica spheres through water. Dashed curves show corresponding results for optical tweezers. Discrete symbols show results for the optical tweezers in Fig. 7.1(c) and the optical conveyors in Figs. 7.1(d) and 7.4(a). Figure from Ref. [13].

At ranges R beyond R_G, radiation pressure overwhelms trapping forces due to axial intensity gradients and ejects the particle. The upper bound of an optical tweezers' range therefore is smaller than the lower bound of an optical conveyor's. This means that optical conveyors can transport objects over substantially longer axial ranges, and at much lower numerical apertures. The price for long-ranged transport is paid in the strength of an optical conveyor's traps.

Figure 7.4(a) is a volumetric reconstruction of an optical conveyor with $\eta =$

0.96 and $\Delta\eta = 0.04$ that was projected with a 60× objective lens (Nikon Plan-Apo, numerical aperture 1.4 oil immersion). Holographic projection limits the conveyor's range to $R = 70\,\mu\mathrm{m}$, and thus suggests an effective numerical aperture of 0.43 given the convergence angle of $\theta = 19°$. The holographically measured trajectory plotted in Fig. 7.4(b) shows this optical conveyor trapping and transporting a $1.5\,\mu\mathrm{m}$-diameter silica sphere over $66\,\mu\mathrm{m}$. The hologram at the bottom of this figure was recorded when the sphere was located at the position indicated by the sphere in Fig. 7.4(b). This measurement demonstrates that an optical conveyor can transport objects along its entire length, even at low numerical aperture.

Figure 7.4(c) shows how the traps' stiffness falls off with range. The solid and dashed curves are Lorenz-Mie calculations of the axial trap stiffness of optical conveyors and optical tweezers, respectively, and are scaled for a peak intensity of $41\,\mathrm{mW\,\mu m^{-2}}$. One set of curves is calculated for a $1.5\,\mu\mathrm{m}$ silica sphere, and agrees reasonably well with experimental results for the optical tweezers in Fig. 7.1(c), the optical conveyor in Fig. 7.1(d) and the optical conveyor in Fig. 7.4(a). The other set is calculated in the Rayleigh regime at $ka_p = 0.5$, and agrees quantitatively with the dipole result from Eq. (7.18).

Despite the dipole prediction from Eq. (7.11), the force experienced by a large particle in an optical conveyor can be purely repulsive. Lorenz-Mie calculations reveal that additional radiation pressure due to off-axis scattering can overwhelm trapping forces due to axial intensity gradients for particles larger than the wavelength of light. Although a conveyor can be projected with a range exceeding this limit, it will not be able to transport large particles in the retrograde direction, and so will not act as a tractor beam.

The dependence of the trapping force on range for small particles shows no such crossover from stable trapping to repulsion. While the optical tweezers is inherently limited to $R/A < 9$ the optical conveyor extends indefinitely, albeit with a stiffness that falls off as R^{-4}. The maximum trapping force in this regime falls off as R^{-2}. Both the force and the stiffness scale with the intensity of the beam, and therefore with the laser power. These considerations demonstrate that optical conveyors are viable candidates for long-ranged tractor beams, particularly for objects that are smaller than the wavelength of light.

7.4 Conclusions

Interference endows optical conveyors with trapping characteristics surpassing those of conventional single-beam optical traps. Most notably, optical conveyors are universal traps that can hold and transport small objects regardless of their light scattering properties. Under conditions where optical tweezers also are effective, moreover, optical conveyors make stiffer traps, particularly in the axial direction.

Optical conveyors act as universal traps because their intensity vanishes at points along the optical axis [8, 37, 38]. This ensures that retrograde forces arising from intensity gradients can counteract radiation pressure to hold illuminated objects in place. These traps can be positioned any placed along the propagation-invariant range of the conveyor by varying the relative phase of the constituent Bessel beams. As a consequence, optical conveyors can transport objects over substantially larger axial distances than conventional optical traps [8, 37, 38], which are inherently limited by radiation pressure.

Further improvements in performance almost certainly can be realized by appropriately structuring the intensity and phase gradients [69, 78, 175] along the projected beam. The range and trapping strength also should improve in optical conveyors created with radially polarized light [79, 125, 176]. These insights apply also to other interferometrically structured beams of light, such as solenoidal waves [29]. Both as tractor beams, and also as ordinary optical traps, interferometrically structured beams of light offer clear benefits for optical micromanipulation.

Chapter 8

Conclusion

Spin-dependent and retrograde optical forces are both examples of how light can interact with matter in unexpected ways. This thesis has examined these topics, theoretically and experimentally, in the context of optical forces in general beams of light. We have developed a framework for understanding optical forces in terms of local and experimentally accessible quantities. This view point has allowed us to clarify how optical spin angular momentum contributes to optical forces. It also has provided direction to our experiments with optical pulling force in optical conveyors that have opened up new possibilities in long range optical trapping. In both cases, our work highlights the interesting physics possible with optical forces in a beam of light.

In Chapter 2, we wrote down the momentum density carried by a beam of light in terms of experimentally accessible quantities [8]. The approach revealed a some interesting properties of the momentum density, in particular a contribution to the linear momentum density from the curl of the spin angular momentum density. This result extended previous work that had identified contributions to the linear momentum in a beam of light from its spin and orbital angular momentum [25,93]. We explored this connection between light's linear and angular momentum by connecting our results to calculations by Belinfante on the origin of optical spin angular momentum [105]. This exploration contributes to the discussion of the paradoxes surrounding spin and orbital angular momentum in light [177, 178]. In strongly focused beams of light, spin and orbital angular momentum are not separately conserved [23], and there are still open questions about the mechanism of conversion between the spin and orbital angular momentum in light [27].

To address these questions, we measured spin dependent optical forces experimentally as describe in Chapter 4. We found that isotropic colloidal microspheres experience spin dependent optical forces in circularly polarized optical traps and that this force arises from the curl of the spin angular momentum density [8]. This result agreed with previous measurements circulation of metallic particles in circularly polarized optical tweezers [22,24], however our work clarified the spin-curl force makes a larger contribution than the spin-to-orbital conversion. This distinction was confirmed by experiments revealing circulation even in beams of light with low convergence [26]. The physical effects of non-uniform optical spin angular momentum continue to be explored [179].

Although we had measured these spin-dependent forces, their origin was not clear. In Chapter 5, we considered the origin of these forces through an analysis of multipole scattering. Surprisingly, at electric dipole level the spin angular momentum density plays no role in optical forces due to an exact cancellation [13]. This result clarified some confusion in the literature that had previously suggested that electric dipolar particles do experience spin curl forces [180]. To find the origin of spin curl force, we considered forces from multipole scattering, which had been shown to create interesting optical forces [150, 151] and allow for optical pulling forces [31]. We found that the interference between multipoles leads to a spin-curl force, but it also leads to another polarization dependent force. This new force seems to act like an intensity gradient except that it is polarization dependent. We used generalized Lorenz-Mie theory to calculate the force on colloidal microspheres so that we can compare to experiment. This quantitative results confirm the existence of spin dependent optical forces in the direction of the spin-curl.

One of the interesting results of this analysis of optical forces was the sensitive dependence on particle properties. We describe how dielectric colloidal microspheres in the Mie regime can develop magnetic multipole moments through their interaction with optical fields. This surprising effect is crucial for spin-dependent optical forces and optical pulling forces [31, 152]. There has been growing interest in these magnetic properties of particles [181], which not only could be useful for tailoring optical forces, but also for creating new metamaterials [182, 183].

Next, we applied these insights in optical forces to the interesting case of optical tractor beams. We demonstrated in Chapter 6 that optical conveyor beams can act as practical realizations of tractor beams [12]. In this work, we showed optical conveyors transport colloidal microparticles bidirectionally over 60 µm using holographic techniques. In addition, optical conveyors are easier to project than optical solenoid beams [29], and their interferometric structure allows them to work for a greater variety of particles than Bessel beam based tractor beams [31, 152].

One disadvantage with optical conveyors is that they need modulation in order to pull, compared to other nonconservative tractor beams [32]. However, this makes them active tractor beams which pull all objects at the same speed over a very wide range of particle properties. Recently, much longer range tractor beams have been demonstrated that take advantage of photophoretic forces [184]. Optical conveyors on the other hand only rely on the light's interaction with the particle and so could work in a vacuum.

Questions about the relative merits of various tractor beams spurred us to study the trapping properties of optical conveyors as described in Chapter 7. The underlying unresolved question surrounding all of these tractor beams was how they performed relative to conventional optical traps. Many of these tractor beams consisted of non-diffracting modes of light [84], and were suggested therefore to have potential for long range trapping [30]. However, physical realizations of these modes were known to have limited range [85] so the advantage of tractor beams was not clear.

Our experiments showed that the axial interference in optical conveyor beams granted them exceptional trapping in the axial direction, which typically is the weak point in optical trapping [13]. In turn, these superior trapping properties suggest that optical conveyors can work over a larger range than conventional optical traps with an especially large advantage for small particles. Our results show that optical tractor beams have the potential to considerably extend the range of optical trapping. Further research is needed to find the optimal beam structure for long-range optical trapping.

Our insights into in optical forces have possible applications not only with optical phenomena but also in acoustics and other wave phenomena. Micromanipulation has long been possible in acoustics through levitation in standing waves [185]. Single-beam gradient force acoustical tweezers have been demonstrated [186]. In addition, demonstrations of acoustic pulling force indicate that tractor beams could be created with to sound waves [187]. Similar pulling forces are possible for floating objects interacting with water waves [188]. These alternative waves can exert much stronger forces than is possible with light since they travel much slower than the speed of light. This property greatly extends the possibilities for micromanipulation.

Throughout this thesis we have analyzed optical forces in terms of the local and experimentally accessible properties of complex beams of light, which has helped us to understand the physically relevant forces. This viewpoint has allowed us to uncover surprising properties of spin dependent forces and to apply this knowledge towards making practical tractor beams with optical conveyor beams. These advances open up possibilities in new spin-dependent forces, in optical metamaterials, and in long-ranged optical trapping. It is not clear what else is possible with light, but this thesis suggests that a better question might be, what is not possible?

Appendix A

Vector Spherical Harmonics

The vector spherical harmonics can be used to decompose a vector field in spherical polar coordinates. When the field is in this form, we can more easily calculate the scattering off of spherical particles. In fact each component of the incident field contributes to the scattered field by an amount that depends on the Lorenz-Mie scattering coefficients [128]. Each textbook uses its own notation so it is hard to compare different formulations. Here we present the calculations of Jackson [104] and Gouesbet [132] in detail to clarify these differences.

Jackson begins with the scalar wave equation,

$$\nabla^2\psi - \frac{1}{c^2}\frac{\partial^2\psi}{\partial t^2} = 0. \tag{A.1}$$

Solutions can be written as an expansion in multipole terms,

$$\psi(\mathbf{r}) = \sum_{l,m}[A_{lm}z_l(kr) + B_{lm}z_l(kr)]Y_{lm}(\theta,\phi), \tag{A.2}$$

where Y_{lm} are the spherical harmonics, defined by

$$Y_{lm}(\theta, \phi) = \tilde{P}_l^m(\cos\theta)e^{im\theta} \tag{A.3}$$

and where $\tilde{P}_l^m(\cos\theta)$ are the normalized associated Legendre polynomials, which are defined by,

$$\tilde{P}_l^m(x) = N_p(-1)^m(1-x^2)^{m/2}\frac{d^m}{dx^m}P_l(x). \tag{A.4}$$

The $P_l(x)$ are the Legendre polynomials defined by Rodrigues' formula and the normalization is $N_p = \sqrt{\frac{(2l+1)(l-m)!}{4\pi(l+m)!}}$. The radial factors $z_l(kr)$ in Eq. (A.2) are spherical Bessel functions, for instance

$$j_l(x) = \sqrt{\frac{\pi}{2x}}J_{l+1/2}(x), \tag{A.5}$$

where $J_l(x)$ is a Bessel function of the first kind of order l.

Next, Jackson points out that Maxwell's equations can be written in the form of the Helmholtz equation and a divergence condition,

$$(\nabla^2 + k^2)\mathbf{E} = 0 \qquad \text{and} \qquad \nabla \cdot \mathbf{E} = 0 \tag{A.6}$$

with $\mathbf{H}$ given by

$$\mathbf{H} = \frac{-i}{kZ_0}\nabla \times \mathbf{E}, \tag{A.7}$$

where $Z_0 = \frac{1}{c\epsilon_0}$ is the impedance of free space. Instead of working with this set of vector equations, we can transform them into a set of scalar equations. The scalar quantities $\mathbf{r} \cdot \mathbf{E}$ and $\mathbf{r} \cdot \mathbf{H}$ each satisfy the scalar Helmholtz equation, which can be shown by using the vector identity,

$$\nabla^2(\mathbf{r} \cdot \mathbf{A}) = \mathbf{r} \cdot \nabla^2 \mathbf{A} + 2\nabla \cdot \mathbf{A}. \tag{A.8}$$

Consequently we can expand $\mathbf{r} \cdot \mathbf{E}$ and $\mathbf{r} \cdot \mathbf{H}$ in terms of Eq. (A.2). The two expansions lead to two families of vector spherical harmonics. Although light is a vector field with three components, only two scalar fields are necessary to describe a general field of light. This interesting fact arises from the transverse nature of the fields.

To extract the electric an magnetic fields from the scalar fields we need to use the angular momentum operator, $\mathbf{L}$, defined by

$$\mathbf{L} = -i\mathbf{r} \times \nabla. \tag{A.9}$$

Jackson shows that

$$\mathbf{r} \cdot \mathbf{H}_{lm}^{(M)} = \frac{l(l+1)}{k} z_l(kr) Y_{lm}(\theta, \phi), \tag{A.10}$$

and the electric field corresponding to this magnetic multipole of order l,m is

$$\mathbf{E}_{lm}^{(M)} = Z_0 z_l(kr) \mathbf{L} Y_{lm}(\theta, \phi). \tag{A.11}$$

Similarly for an electric multipole field,

$$\mathbf{E}_{lm}^{(E)} = \frac{iZ_0}{k} \nabla \times (z_l(kr) \mathbf{L} Y_{lm}(\theta, \phi)). \tag{A.12}$$

These two sets of functions are the vector spherical harmonics (VSHs), which are orthogonal functions that form a basis for a general field of light. Such a field can be written as a sum of the VSHs,

$$\mathbf{E} = \sum_{l,m} \left\{ \frac{i}{k} a_E(l,m) \nabla \times [z_l(kr) \mathbf{L} Y_{lm}(\theta,\phi)] + a_M(l,m) \mathbf{L} Y_{lm}(\theta,\phi) \right\}. \tag{A.13}$$

Here we depart slightly from Jackson who defines his vector spherical harmonic function $\mathbf{X}_{lm}$ with a factor of $1/\sqrt{l(l+1)}$ that we omit for consistency with other formulations.

We can write these functions in spherical coordinates to facilitate comparison. Considering the magnetic term first,

$$\begin{aligned} j_l(kr) \mathbf{L} Y_{lm}(\theta,\phi) &= -i j_l(kr) \mathbf{r} \times \nabla Y_{lm}(\theta,\phi) && \text{(A.14)} \\ &= -\hat{\phi} i \frac{\psi_l(kr)}{kr} \partial_\theta Y_{lm}(\theta,\phi) && \text{(A.15)} \\ &\quad -\hat{\theta} \frac{\psi_l(kr)}{kr} \frac{m Y_{lm}(\theta,\phi)}{\sin\theta}, && \text{(A.16)} \end{aligned}$$

where $\psi_l(kr) = kr z_l(kr)$. Next we evaluate the electric term,

$$\begin{aligned} \frac{-i}{k} \nabla \times j_l(kr) \mathbf{L} Y_{lm}(\theta,\phi) &= \frac{-i}{k} \nabla \times \mathbf{L}(j_l(kr) Y_{lm}(\theta,\phi)) && \text{(A.17)} \\ &= \hat{r} \frac{l(l+1)}{(kr)^2} \psi_l(kr) Y_{lm}(\theta,\phi) && \text{(A.18)} \\ &\quad + \hat{\theta} \frac{1}{kr} \psi_l'(kr) \partial_\theta Y_{lm}(\theta,\phi) && \text{(A.19)} \\ &\quad + \hat{\phi} \frac{im}{kr} \psi_l'(kr) \frac{Y_{lm}(\theta,\phi)}{\sin\theta}. && \text{(A.20)} \end{aligned}$$

There are a number of steps in evaluating this term. We used the fact that the angular momentum operator only operates on the angular variables. We also used Eq. (9.125) in Jackson and Eq. (8) in Gouesbet [132]. This yields the same result as Eq. (1) and Eq. (2) in Gouesbet for the magnetic and the electric VSHs respectively, except for a factor of $(-1)^m$.

For a circularly polarized plane wave traveling along the z axis, the coefficients are

$$a_M(l,m)_\pm = i^l \sqrt{\frac{4\pi(2l+1)}{l(l+1)}}\delta_{m,\pm 1} \quad \text{and} \tag{A.21}$$

$$a_E(l,m)_\pm = \pm i a_M(l,m)_\pm. \tag{A.22}$$

These differ from the corresponding coefficients defined in Bohren and Huffman [128] by the square root.

The series in Eq. (A.13) tends to be numerically unstable when the angular dependence is computed in terms of the Legendre polynomials directly. More reliable results are obtained by expressing the angular dependence in terms of the normalized angular functions $\tilde{\pi}_{mn}$ and $\tilde{\tau}_{mn}$ [128, 189], which are defined by,

$$\tilde{\pi}_{mn}(\cos\theta) = m\frac{\tilde{P}_n^m(\cos\theta)}{\sin\theta} \tag{A.23}$$

and

$$\tilde{\tau}_{mn}(\cos\theta) = \partial_\theta \tilde{P}_n^m(\cos\theta). \tag{A.24}$$

This gives us an improved expression for the vector spherical harmonics,

$$j_l(kr)\mathbf{L}Y_{lm}(\theta,\phi) = -\hat{\phi} i \frac{\psi_l(kr)}{kr}\tilde{\tau}_{mn}(\cos\theta)e^{im\phi} - \hat{\theta}\frac{\psi_l(kr)}{kr}\tilde{\pi}_{mn}(\cos\theta)e^{im\phi}, \tag{A.25}$$

and,

$$\begin{aligned}\frac{-i}{k}\nabla \times j_l(kr)\mathbf{L}Y_{lm}(\theta,\phi) = \hat{r}\frac{l(l+1)}{(kr)^2}\psi_l(kr)Y_{lm}(\theta,\phi) \\ + \hat{\theta}\frac{1}{kr}\psi_l'(kr)\tilde{\tau}_{mn}(\cos\theta)e^{im\phi} \\ + \hat{\phi}\frac{i}{kr}\psi_l'(kr)\tilde{\pi}_{mn}(\cos\theta)e^{im\phi}.\end{aligned} \tag{A.26}$$

These are the forms that were used for the numerical calculations in this thesis.

Bibliography

[1] Wikimedia Commons, "The Bayeux Tapestry," 1070s. Bayeux Museum, France. [cited on 12-23-14] http://en.wikipedia.org/wiki/Halley.

[2] Wikimedia Commons, "Johannes Kepler," 1610, Benediktinerkloster, Kremsmuenster, Germany. [cited on 12-23-14] http://en.wikipedia.org/wiki/Johannes_Kepler.

[3] Wikimedia Commons, "Leonhard Euler," by Jakob Emanuel Handmann, 1756. [cited on 12-23-14] http://en.wikipedia.org/wiki/Leonhard_Euler.

[4] E. F. Nichols and G. F. Hull, "The pressure due to radiation," *Proc. Am. Acad. Arts Sci.*, vol. 38, pp. 559–599, 1903.

[5] A. Ashkin, "Acceleration and trapping of particles by radiation pressure," *Phys. Rev. Lett.*, vol. 24, pp. 156–159, 1970.

[6] J. E. Curtis and D. G. Grier, "Structure of optical vortices," *Phys. Rev. Lett.*, vol. 90, p. 133901, 2003.

[7] G. Cipparrone, I. Ricardez-Vargas, P. Pagliusi, and C. Provenzano, "Polarization gradient: exploring an original route for optical trapping and manipulation," *Opt. Express*, vol. 18, pp. 6008–6013, Mar. 2010.

[8] D. B. Ruffner and D. G. Grier, "Optical forces and torques in nonuniform beams of light," *Phys. Rev. Lett.*, vol. 108, p. 173602, Apr. 2012.

[9] F. C. Cheong, D. G. Grier, and S.-H. Lee, "Holographic microscopy of holographically trapped three-dimensional structures," U. S. Patent Application 20100253762, New York University, 2010.

[10] B. Sun, Y. Roichman, and D. G. Grier, "Theory of holographic optical trapping," *Opt. Express*, vol. 16, no. 20, pp. 15765–15776, 2008.

[11] Y. Roichman and D. G. Grier, "Projecting extended optical traps with shape-phase holography," *Opt. Lett.*, vol. 31, no. 11, pp. 1675–1677, 2006.

[12] D. B. Ruffner and D. G. Grier, "Optical conveyors: A class of active tractor beams," *Phys. Rev. Lett.*, vol. 109, p. 163903, Oct. 2012.

[13] D. B. Ruffner and D. G. Grier, "Universal, strong and long-ranged trapping by optical conveyors," *Opt. Express*, vol. 22, pp. 26834–26843, Nov 2014.

[14] A. Ashkin, J. M. Dziedzic, J. E. Bjorkholm, and S. Chu, "Observation of a single-beam gradient force optical trap for dielectric particles," *Opt. Lett.*, vol. 11, pp. 288–290, May 1986.

[15] D. G. Grier, "A revolution in optical manipulation," *Nature*, vol. 424, no. 6950, pp. 810–816, 2003.

[16] M. Dienerowitz, M. Mazilu, and K. Dholakia, "Optical manipulation of nanoparticles: a review," *Journal of Nanophotonics*, vol. 2, no. 1, pp. 021875–021875–32, 2008.

[17] O. M. Marag, P. H. Jones, P. G. Gucciardi, G. Volpe, and A. C. Ferrari, "Optical trapping and manipulation of nanostructures," *Nature Nanotechnology*, vol. 8, pp. 807–819, Nov. 2013.

[18] L. Allen, M. W. Beijersbergen, R. J. C. Spreeuw, and J. P. Woerdman, "Orbital angular momentum of light and the transformation of laguerre-gaussian laser modes," *Phys. Rev. A*, vol. 45, p. 8185, June 1992.

[19] H. He, M. E. J. Friese, N. R. Heckenberg, and H. Rubinsztein-Dunlop, "Direct observation of transfer of angular momentum to absorptive particles from a laser beam with a phase singularity," *Phys. Rev. Lett.*, vol. 75, p. 826, July 1995.

[20] R. A. Beth, "Mechanical detection and measurement of the angular momentum of light," *Physical Review*, vol. 50, p. 115, July 1936.

[21] X.-L. Wang, J. Chen, Y. Li, J. Ding, C.-S. Guo, and H.-T. Wang, "Optical orbital angular momentum from the curl of polarization," *Phys. Rev. Lett.*, vol. 105, p. 253602, Dec. 2010.

[22] Y. Zhao, D. Shapiro, D. Mcgloin, D. T. Chiu, and S. Marchesini, "Direct observation of the transfer of orbital angular momentum to metal particles from a focused circularly polarized gaussian beam," *Opt. Express*, vol. 17, p. 23316, Dec. 2009.

[23] T. A. Nieminen, A. B. Stilgoe, N. R. Heckenberg, and H. Rubinsztein-Dunlop, "Angular momentum of a strongly focused gaussian beam," *Journal of Optics A: Pure and Applied Optics*, vol. 10, p. 115005, Nov. 2008.

[24] Y. Zhao, J. Edgar, G. Jeffries, D. McGloin, and D. Chiu, "Spin-to-orbital angular momentum conversion in a strongly focused optical beam," *Phys. Rev. Lett.*, vol. 99, Aug. 2007.

[25] M. V. Berry, "Optical currents," *Journal of Optics A: Pure and Applied Optics*, vol. 11, p. 094001, Sept. 2009.

[26] O. V. Angelsky, A. Y. Bekshaev, P. P. Maksimyak, A. P. Maksimyak, S. G. Hanson, and C. Y. Zenkova, "Orbital rotation without orbital angular momentum: mechanical action of the spin part of the internal energy flow in light beams," *Opt. Express*, vol. 20, pp. 3563–3571, Feb. 2012.

[27] S. M. Barnett, "Rotation of electromagnetic fields and the nature of optical angular momentum," *Journal of Modern Optics*, vol. 57, no. 14-15, pp. 1339–1343, 2010.

[28] K. Y. Bliokh, M. A. Alonso, and E. A. Ostrovskaya, *Angular Momenta and Spin-Orbit Interaction of Nonparaxial Light in Free Space*. 2010.

[29] S.-H. Lee, Y. Roichman, and D. G. Grier, "Optical solenoid beams," *Opt. Express*, vol. 18, pp. 6988–6993, Mar. 2010.

[30] S. Sukhov and A. Dogariu, "On the concept of "tractor beams"," *Opt. Lett.*, vol. 35, pp. 3847–3849, Nov 2010.

[31] J. Chen, J. Ng, Z. Lin, and C. T. Chan, "Optical pulling force," *Nature Photonics*, vol. 5, pp. 531–534, July 2011.

[32] S. Sukhov and A. Dogariu, "Negative nonconservative forces: Optical "tractor beams" for arbitrary objects," *Phys. Rev. Lett.*, vol. 107, p. 203602, Nov 2011.

[33] T. Kudo and H. Ishihara, "Proposed nonlinear resonance laser technique for manipulating nanoparticles," *Phys. Rev. Lett.*, vol. 109, p. 087402, Aug 2012.

[34] A. Novitsky, C.-W. Qiu, and A. Lavrinenko, "Material-independent and size-independent tractor beams for dipole objects," *Phys. Rev. Lett.*, vol. 109, p. 023902, Jul 2012.

[35] P. L. Marston, "Axial radiation force of a bessel beam on a sphere and direction reversal of the force," *The Journal of the Acoustical Society of America*, vol. 120, no. 6, pp. 3518–3524, 2006.

[36] T. imr, V. Kollrov, Z. Bouchal, and P. Zemnek, "Sub-micron particle organization by self-imaging of non-diffracting beams," *New Journal of Physics*, vol. 8, pp. 43–43, Mar. 2006.

[37] T. imr, V. Garcs-Chvez, K. Dholakia, and P. Zemnek, "Optical conveyor belt for delivery of submicron objects," *Appl. Phys. Lett.*, vol. 86, no. 17, pp. –, 2005.

[38] T. imr, M. iler, and P. Zemnek, "An optical nanotrap array movable over a milimetre range," *Applied Physics B*, vol. 84, no. 1-2, pp. 197–203, 2006.

[39] P. Apianus, *Astronomicum Caesareum.* 1540.

[40] P. Lancaster-Brown, *Halley and His Comet.* Blandford Press, 1985.

[41] J. Kepler, *De Cometis Libelli Tres.* Avgvst Vindelicorvm: A. Apergeri, 1619.

[42] L. Euler, "Recherches physiques sur la cause de la queüe des cometes, de la lumiere boreale et de la lumiere zodiacale," *Mémoires de l'Académie Royale des Sciences de Berlin*, vol. 2, pp. 117–140, 1746.

[43] J. C. Maxwell, *A Treatise on Electricity and Magnetism.* London: Oxford University, 1873.

[44] P. Lebedew, "Testings on the compressive force of light," *AdP*, vol. 6, pp. 433–458, 1901.

[45] E. F. Nichols and G. F. Hull, "The application of radiation pressure to cometary theory," *Astrophys. J.*, vol. 17, pp. 352–360, 1903.

[46] P. S. Epstein, "Die ponderomotorischen drehwirkungen einer lichtwelle und die impulssätze der elektronentheorie," *Ann. der Phys.*, vol. 349, pp. 593–604, 1914.

[47] R. A. Beth, "Direct detection of the angular momentum of light," *Phys. Rev.*, vol. 48, p. 471, 1935.

[48] A. Ashkin, "Forces of a single-beam gradient laser trap on a dielectric sphere in the ray optics regime," *Biophys J*, vol. 61, pp. 569–582, Feb 1992.

[49] A. Ashkin and J. M. Dziedzic, "Optical trapping and manipulation of viruses and bacteria," *Science*, vol. 235, no. 4795, pp. 1517–1520, 1987.

[50] A. Ashkin, J. M. Dziedzic, and T. Yamane, "Optical trapping and manipulation of single cells using infrared-laser beams," *Nature*, vol. 330, no. 6149, pp. 608–609, 1987.

[51] K. Svoboda and S. M. Block, "Biological applications of optical forces," *Annual Review of Biophysics and Biomolecular Structure*, vol. 23, pp. 247–285, 1994.

[52] S. M. Block, L. S. B. Goldstein, and B. J. Schnapp, “Bead movement by single kinesin molecules studied with optical tweezers,” *Nature*, vol. 348, no. 6299, pp. 348–352, 1990.

[53] K. Svoboda, C. F. Schmidt, B. J. Schnapp, and S. M. Block, “Direct observation of kinesin stepping by optical trapping interferometry,” *Nature*, vol. 365, no. 6448, pp. 721–727, 1993.

[54] H. M. Warrick, R. M. Simmons, J. T. Finer, T. Q. P. Uyeda, S. Chu, and J. A. Spudich, “In-vitro methods for measuring force and velocity of the actin-myosin interaction using purified proteins,” *Methods in Cell Biology*, vol. 39, pp. 1–21, 1993.

[55] J. T. Finer, R. M. Simmons, and J. A. Spudich, “Single myosin molecule mechanics – piconewton forces and nanometer steps,” *Nature*, vol. 368, no. 6467, pp. 113–119, 1994.

[56] T. T. Perkins, D. E. Smith, R. G. Larson, and S. Chu, “Stretching of a single tethered polymer in a uniform flow,” *Science*, vol. 268, pp. 83–87, 1995.

[57] S. R. Quake, H. Babcock, and S. Chu, “The dynamics of partially extended single molecules of DNA,” *Nature*, vol. 388, no. 6638, pp. 151–154, 1997.

[58] S. Chu, J. E. Bjorkholm, A. Ashkin, and A. Cable, “Experimental observation of optically trapped atoms,” *Phys. Rev. Lett.*, vol. 57, pp. 314–317, 1986.

[59] J. C. Crocker and D. G. Grier, “Microscopic measurement of the pair interaction potential of charge-stabilized colloid,” *Phys. Rev. Lett.*, vol. 73, no. 2, pp. 352–355, 1994.

[60] A. D. Dinsmore, A. G. Yodh, and D. J. Pine, "Entropic control of particle motion using passive surface microstructures," *Nature*, vol. 383, no. 6597, pp. 239–242, 1996.

[61] A. Terray, J. Oakey, and D. W. M. Marr, "Microfluidic control using colloidal devices," *Science*, vol. 296, no. 5574, pp. 1841–1844, 2002.

[62] A. Terray, J. Oakey, and D. W. M. Marr, "Fabrication of linear colloidal structures for microfluidic applications," *Appl. Phys. Lett.*, vol. 81, no. 9, pp. 1555–1557, 2002.

[63] M. E. J. Friese, T. A. Nieminen, N. R. Heckenberg, and H. Rubinsztein-Dunlop, "Optical torque controlled by elliptical polarization," *Opt. Lett.*, vol. 23, no. 1, pp. 1–3, 1998.

[64] M. E. J. Friese, T. A. Nieminen, N. R. Heckenberg, and H. Rubinsztein-Dunlop, "Optical alignment and spinning of laser-trapped microscopic particles," *Nature*, vol. 394, pp. 348–350, July 1998.

[65] N. B. Simpson, L. Allen, and M. J. Padgett, "Optical tweezers and optical spanners with laguerre-gaussian modes," *Journal of Modern Optics*, vol. 43, pp. 2485–2491, Dec. 1996.

[66] K. T. Gahagan and J. Swartzlander, "Optical vortex trapping of particles," *Opt. Lett.*, vol. 21, pp. 827–829, June 1996.

[67] M. E. J. Friese, J. Enger, H. Rubinsztein-Dunlop, and N. R. Heckenberg, "Optical angular-momentum transfer to trapped absorbing particles," *Phys. Rev. A*, vol. 54, no. 2, pp. 1593–1596, 1996.

[68] "Multi-functional optical tweezers using computer-generated holograms," *Optics Communications*, vol. 185, no. 13, pp. 77 – 82, 2000.

[69] Y. Roichman, B. Sun, Y. Roichman, J. Amato-Grill, and D. G. Grier, "Optical forces arising from phase gradients," *Phys. Rev. Lett.*, vol. 100, p. 013602, Jan. 2008.

[70] E. R. Dufresne and D. G. Grier, "Optical tweezer arrays and optical substrates created with diffractive optical elements," *Rev. Sci. Instrum.*, vol. 69, no. 5, pp. 1974–1977, 1998.

[71] Y. Roichman, A. S. Waldron, E. Gardel, and D. G. Grier, "Performance of optical traps with geometric aberrations," *Appl. Opt.*, vol. 45, no. 15, pp. 3425–3429, 2006.

[72] D. Preece, S. Keen, E. Botvinick, R. Bowman, M. Padgett, and J. Leach, "Independent polarisation control of multiple optical traps," *Opt. Express*, vol. 16, no. 20, pp. 15897–15902, 2008.

[73] S. J. van Enk and G. Nienhuis, "Spin and orbital angular momentum of photons," *Europhys. Lett.*, vol. 25, pp. 497–501, 1994.

[74] A. T. ONeil and M. J. Padgett, "Three-dimensional optical confinement of micron-sized metal particles and the decoupling of the spin and orbital angular momentum within an optical spanner," *Optics Communications*, vol. 185, pp. 139–143, Nov. 2000.

[75] A. T. O'Neil, I. MacVicar, L. Allen, and M. J. Padgett, "Intrinsic and extrinsic nature of the orbital angular momentum of a light beam," *Phys. Rev. Lett.*, vol. 88, p. 053601, Jan. 2002.

[76] L. Marrucci, E. Karimi, S. Slussarenko, B. Piccirillo, E. Santamato, E. Nagali, and F. Sciarrino, “Spin-to-orbital conversion of the angular momentum of light and its classical and quantum applications,” *J. Opt.*, vol. 13, p. 064001, 2011.

[77] M. Gu and D. Morrish, “Three-dimensional trapping of mie metallic particles by the use of obstructed laser beams,” *Journal of Applied Physics*, vol. 91, no. 3, 2002.

[78] M. Lei, Z. Li, S. Yan, B. Yao, D. Dan, Y. Qi, J. Qian, Y. Yang, P. Gao, and T. Ye, “Long-distance axial trapping with focused annular laser beams,” *PLoS ONE*, vol. 8, p. e57984, Mar. 2013.

[79] M. Michihata, T. Hayashi, and Y. Takaya, “Measurement of axial and transverse trapping stiffness of optical tweezers in air using a radially polarized beam,” *Appl. Opt.*, vol. 48, pp. 6143–6151, Nov. 2009.

[80] Q. Zhan, “Trapping metallic rayleigh particles with radial polarization,” *Opt. Express*, vol. 12, no. 15, p. 3377, 2004.

[81] A. Jannasch, A. F. Demirors, P. D. J. van Oostrum, A. van Blaaderen, and E. Schaffer, “Nanonewton optical force trap employing anti-reflection coated, high-refractive-index titania microspheres,” *Nat Photon*, vol. 6, pp. 469–473, Jul 2012.

[82] P. J. Rodrigo, V. R. Daria, and J. Glückstad, “Real-time three-dimensional optical micromanipulation of multiple particlesand living cells,” *Opt. Lett.*, vol. 29, pp. 2270–2272, Oct 2004.

[83] P. J. Rodrigo, V. R. Daria, and J. Glckstad, “Four-dimensional optical manipulation of colloidal particles,” *Appl. Phys. Lett.*, vol. 86, no. 7, pp. –, 2005.

[84] J. Durnin, “Exact solutions for nondiffracting beams. i. the scalar theory,” *Journal of the Optical Society of America A*, vol. 4, pp. 651–654, Apr. 1987.

[85] J. Durnin, J. Miceli, and J. Eberly, “Diffraction-free beams,” *Phys. Rev. Lett.*, vol. 58, pp. 1499–1501, Apr 1987.

[86] “Optical micromanipulation using a bessel light beam,” *Optics Communications*, vol. 197, no. 46, pp. 239 – 245, 2001.

[87] V. Garces-Chavez, D. McGloin, H. Melville, W. Sibbett, and K. Dholakia, “Simultaneous micromanipulation in multiple planes using a self-reconstructing light beam,” *Nature*, vol. 419, pp. 145–147, Sep 2002.

[88] E. E. Smith, “Spacehounds of ipc,” *Amazing Stories*, July 1931.

[89] A. Novitsky, C.-W. Qiu, and H. Wang, “Single gradientless light beam drags particles as tractor beams,” *Phys. Rev. Lett.*, vol. 107, p. 203601, Nov 2011.

[90] S. M. Block, “Making light work with optical tweezers,” *Nature*, vol. 360, pp. 493–495, Dec 1992.

[91] G. Sinclair, P. Jordan, J. Leach, M. J. Padgett, and J. Cooper, “Defining the trapping limits of holographical optical tweezers,” *Journal of Modern Optics*, vol. 51, pp. 409–414, Feb. 2004.

[92] J. H. Poynting, “On the transfer of energy in the electromagnetic field,” *Philosophical Transactions of the Royal Society of London*, vol. 175, pp. 343–

361, 1884.

[93] S. M. Barnett, "Optical angular-momentum flux*," *Journal of Optics B: Quantum and Semiclassical Optics*, vol. 4, pp. S7–S16, Apr. 2002.

[94] M. Polin, Y. Roichman, and D. G. Grier, "Autocalibrated colloidal interaction measurements with extended optical traps," *Phys. Rev. E*, vol. 77, p. 051401, 2008.

[95] E. R. Shanblatt and D. G. Grier, "Extended and knotted optical traps in three dimensions," *Opt. Express*, vol. 19, pp. 5833–5838, Mar. 2011.

[96] C. Leavens, "Weak measurements from the point of view of bohmian mechanics," *Foundations of Physics*, vol. 35, no. 3, pp. 469–491, 2005.

[97] Y. Aharonov, D. Z. Albert, and L. Vaidman, "How the result of a measurement of a component of the spin of a spin-1/2 particle can turn out to be 100," *Phys. Rev. Lett.*, vol. 60, pp. 1351–1354, Apr 1988.

[98] S. Kocsis, B. Braverman, S. Ravets, M. J. Stevens, R. P. Mirin, L. K. Shalm, and A. M. Steinberg, "Observing the average trajectories of single photons in a two-slit interferometer," *Science*, vol. 332, no. 6034, pp. 1170–1173, 2011.

[99] K. Y. Bliokh, A. Y. Bekshaev, A. G. Kofman, and F. Nori, "Photon trajectories, anomalous velocities and weak measurements: a classical interpretation," *New Journal of Physics*, vol. 15, no. 7, p. 073022, 2013.

[100] R. Dorn, S. Quabis, and G. Leuchs, "Sharper focus for a radially polarized light beam," *Phys. Rev. Lett.*, vol. 91, p. 233901, 2003.

[101] M. O. Scully and M. S. Zubairy, "Simple laser accelerator: Optics and particle dynamics," *Phys. Rev. A*, vol. 44, pp. 2656–2663, 1991.

[102] R. Pfleegor and L. Mandel, "Interference of independent photon beams," *Phys. Rev.*, vol. 159, pp. 1084–1088, Jul 1967.

[103] S.-H. Lee and D. G. Grier, "Holographic microscopy of holographically trapped three-dimensional structures," *Opt. Express*, vol. 15, pp. 1505–1512, 2007.

[104] J. D. Jackson, *Classical Electrodynamics Third Edition.* Wiley, 3 ed., Aug. 1998.

[105] B. F.J., "On the current and the density of the electric charge, the energy, the linear momentum and the angular momentum of arbitrary fields," *Physica*, vol. 7, pp. 449–474, May 1940.

[106] M. Reicherter, T. Haist, E. U. Wagemann, and H. J. Tiziani, "Optical particle trapping with computer-generated holograms written on a liquid-crystal display," *Opt. Lett.*, vol. 24, pp. 608–610, May 1999.

[107] E. R. Dufresne, G. C. Spalding, M. T. Dearing, S. A. Sheets, and D. G. Grier, "Computer-generated holographic optical tweezer arrays," *Rev. Sci. Instrum.*, vol. 72, no. 3, pp. 1810–1816, 2001.

[108] D. G. Grier and Y. Roichman, "Holographic optical trapping," *Appl. Opt.*, vol. 45, pp. 880–887, 2006.

[109] K. Visscher, G. J. Brakenhoff, and J. J. Krol, "Micromanipulation by multiple optical traps created by a single fast scanning trap integrated with

the bilateral confocal scanning laser microscope," *Cytometry*, vol. 14, no. 2, pp. 105–114, 1993.

[110] C. Mio, T. Gong, A. Terray, and D. W. M. Marr, "Design of a scanning laser optical trap for multiparticle manipulation," *Rev. Sci. Instrum.*, vol. 71, no. 5, pp. 2196–2200, 2000.

[111] H. He, N. R. Heckenberg, and H. Rubinsztein-Dunlop, "Optical particle trapping with higher-order doughnut beams produced using high efficiency computer generated holograms," *Journal of Modern Optics*, vol. 42, pp. 217–223, Jan. 1995.

[112] K. Ladavac, K. Kasza, and D. G. Grier, "Sorting by periodic potential energy landscapes: Optical fractionation," *Phys. Rev. E*, vol. 70, no. 1, p. 010901(R), 2004.

[113] K. Ladavac and D. G. Grier, "Colloidal hydrodynamic coupling in concentric optical vortices," *Europhys. Lett.*, vol. 70, no. 4, pp. 548–554, 2005.

[114] J. W. Goodman, *Introduction to Fourier Optics.* New York: McGraw-Hill, 3rd ed., 2005.

[115] J. E. Curtis, B. A. Koss, and D. G. Grier, "Dynamic holographic optical tweezers," *Optics Communications*, vol. 207, pp. 169–175, June 2002.

[116] Y. Roichman, G. M. Zaslavsky, and D. G. Grier, "Anomalous collective dynamics in optically driven colloidal rings," *Phys. Rev. E*, vol. 75, p. 020401(R), 2007.

[117] L. D. Victor A. Soifer, V Kotlar, *Iterative Methods for Diffractive Optical Elements Computation.* CRC Press, 1997.

[118] E. Wolf, “Electromagnetic diffraction in optical systems. i. an integral representation of the image field,” *Proceedings of the Royal Society of London. Series A. Mathematical and Physical Sciences*, vol. 253, pp. 349 –357, Dec. 1959.

[119] B. Richards and E. Wolf, “Electromagnetic diffraction in optical systems. II. structure of the image field in an aplanatic system,” *Proceedings of the Royal Society of London. Series A. Mathematical and Physical Sciences*, vol. 253, pp. 358 –379, Dec. 1959.

[120] T. A. Nieminen, V. L. Y. Loke, A. B. Stilgoe, G. Knner, A. M. Braczyk, N. R. Heckenberg, and H. Rubinsztein-Dunlop, “Optical tweezers computational toolbox,” *Journal of Optics A: Pure and Applied Optics*, vol. 9, pp. S196–S203, Aug. 2007.

[121] Q. Zhan, “Cylindrical vector beams: from mathematical concepts to applications,” *Advances in Optics and Photonics*, vol. 1, p. 1, Jan. 2009.

[122] W. Cheng, J. W. Haus, and Q. Zhan, “Propagation of vector vortex beams through a turbulent atmosphere,” *Opt. Express*, vol. 17, pp. 17829–17836, Sep 2009.

[123] D. P. Biss, K. S. Youngworth, and T. G. Brown, “Dark-field imaging with cylindrical-vector beams,” *Appl. Opt.*, vol. 45, pp. 470–479, Jan 2006.

[124] Q. Zhan, “Radiation forces on a dielectric sphere produced by highly focused cylindrical vector beams,” *Journal of Optics A: Pure and Applied Optics*, vol. 5, no. 3, p. 229, 2003.

[125] H. Kawauchi, K. Yonezawa, Y. Kozawa, and S. Sato, "Calculation of optical trapping forces on a dielectric sphere in the ray optics regime produced by a radially polarized laser beam," *Opt. Lett.*, vol. 32, pp. 1839–1841, July 2007.

[126] M. Born and E. Wolf, *Principles of Optics: Electromagnetic Theory of Propagation, Interference and Diffraction of Light.* Cambridge University Press, 6 ed., Nov. 1997.

[127] W. H. McMaster, "Polarization and the stokes parameters," *American Journal of Physics*, vol. 22, no. 6, 1954.

[128] C. F. Bohren and D. R. Huffman, *Absorption and Scattering of Light by Small Particles.* Wiley-VCH Verlag GmbH, 2007.

[129] F. C. Cheong, K. Xiao, D. J. Pine, and D. G. Grier, "Holographic characterization of individual colloidal spheres' porosities," *Soft Matter*, vol. 7, pp. 6816–6819, 2011.

[130] M. I. Mishchenko, *Electromagnetic Scattering by Particles and Particle Groups.* Cambridge University Press, 2014.

[131] G. Gouesbet and G. Grhan, *Generalized Lorenz-Mie Theories.* Berlin; New York: Springer, 2011 edition ed., Feb. 2011.

[132] "T-matrix formulation and generalized lorenzmie theories in spherical coordinates," *Optics Communications*, vol. 283, no. 4, pp. 517 – 521, 2010.

[133] C. B. Markwardt, "Non-linear least-squares fitting in idl with mpfit," in *Astronomical Data Analysis Software and Systems XVIII* (P. D. D. Bohlender and D. Durand, eds.), San Francisco: Astronomical Society of the Pacific, 2009.

[134] J. Mor, "The levenberg-marquardt algorithm: Implementation and theory," in *Numerical Analysis* (G. Watson, ed.), vol. 630 of *Lecture Notes in Mathematics*, pp. 105–116, Springer Berlin Heidelberg, 1978.

[135] B. J. Krishnatreya, A. Colen-Landy, P. Hasebe, B. A. Bell, J. R. Jones, A. Sunda-Meya, and D. G. Grier, "Measuring boltzmann's constant through holographic video microscopy of a single colloidal sphere," *American Journal of Physics*, vol. 82, no. 1, pp. 23–31, 2014.

[136] S. K. Mohanty, K. D. Rao, and P. K. Gupta, "Optical trap with spatially varying polarization: application in controlled orientation of birefringent microscopic particle(s)," *Applied Physics B*, vol. 80, pp. 631–634, Mar. 2005.

[137] E. Santamato, B. Daino, M. Romagnoli, M. Settembre, and Y. R. Shen, "Collective rotation of molecules driven by the angular momentum of light in a nematic film," *Phys. Rev. Lett.*, vol. 57, pp. 2423–2426, Nov. 1986.

[138] A. I. Bishop, T. A. Nieminen, N. R. Heckenberg, and H. Rubinsztein-Dunlop, "Optical microrheology using rotating laser-trapped particles," *Phys. Rev. Lett.*, vol. 92, p. 198104, May 2004.

[139] S. Yan, B. Yao, and M. Lei, "Comment on Optical orbital angular momentum from the curl of polarization," *Phys. Rev. Lett.*, vol. 106, p. 189301, May 2011.

[140] X. L. Wang, J. Chen, Y. N. Li, J. P. Ding, C. S. Guo, and H. T. Wang, "Wang et al. reply:," *Phys. Rev. Lett.*, vol. 106, p. 189302, May 2011.

[141] Z. Bomzon, M. Gu, and J. Shamir, "Angular momentum and geometrical phases in tight-focused circularly polarized plane waves," *Appl. Phys. Lett.*,

vol. 89, p. 241104, 2006.

[142] J. C. Crocker and D. G. Grier, "Methods of digital video microscopy for colloidal studies," *J. Colloid Interface Sci.*, vol. 179, pp. 298–310, 1996.

[143] B. W. Silverman, *Density Estimation for Statistics and Data Analysis.* Chapman and Hall/CRC, 1 ed., Apr. 1986.

[144] Y. Roichman, B. Sun, A. Stolarski, and D. G. Grier, "Influence of nonconservative optical forces on the dynamics of optically trapped colloidal spheres: The fountain of probability," *Phys. Rev. Lett.*, vol. 101, no. 12, p. 128301, 2008.

[145] B. Sun, J. Lin, E. Darby, A. Y. Grosberg, and D. G. Grier, "Brownian vortexes," *Phys. Rev. E*, vol. 80, p. 010401, July 2009.

[146] B. Sun, D. G. Grier, and A. Y. Grosberg, "Minimal model for brownian vortexes," *Phys. Rev. E*, vol. 82, no. 2, p. 021123, 2010.

[147] J. P. Gordon, "Radiation forces and momenta in dielectric media," *Phys. Rev. A*, vol. 8, pp. 14–21, July 1973.

[148] P. C. Chaumet and M. Nieto-Vesperinas, "Time-averaged total force on a dipolar sphere in an electromagnetic field," *Opt. Lett.*, vol. 25, pp. 1065–1067, Aug. 2000.

[149] D. B. Ruffner and D. G. Grier, "Comment on "scattering forces from the curl of the spin angular momentum of a light field"," *Phys. Rev. Lett.*, vol. 111, p. 059301, Jul 2013.

[150] M. Nieto-Vesperinas, J. J. Senz, R. Gmez-Medina, and L. Chantada, "Optical forces on small magnetodielectric particles," *Opt. Express*, vol. 18, pp. 11428–11443, May 2010.

[151] P. C. Chaumet and A. Rahmani, "Electromagnetic force and torque onmagnetic and negative-index scatterers," *Opt. Express*, vol. 17, pp. 2224–2234, Feb. 2009.

[152] O. Brzobohat, V. Karsek, M. iler, L. Chvtal, T. imr, and P. Zemnek, "Experimental demonstration of optical transport, sorting and self-arrangement using a /'tractor beam/'," *Nature Photonics*, vol. 7, pp. 123–127, Feb. 2013.

[153] J. M. Taylor and G. D. Love, "Multipole expansion of bessel and gaussian beams for mie scattering calculations," *Journal of the Optical Society of America A*, vol. 26, pp. 278–282, Feb 2009.

[154] "Optical forces in a non-diffracting vortex beam," *Journal of Quantitative Spectroscopy and Radiative Transfer*, vol. 126, no. 0, pp. 78 – 83, 2013.

[155] N. Wang, J. Chen, S. Liu, and Z. Lin, "Dynamical and phase-diagram study on stable optical pulling force in bessel beams," *Phys. Rev. A*, vol. 87, p. 063812, June 2013.

[156] D. W. Mackowski, "Calculation of total cross sections of multiple-sphere clusters," *Journal of the Optical Society of America A*, vol. 11, pp. 2851–2861, Nov. 1994.

[157] J. P. Barton, "Internal and near-surface electromagnetic fields for a spheroidal particle with arbitrary illumination," *Appl. Opt.*, vol. 34, pp. 5542–5551, Aug 1995.

[158] A. B. Stilgoe, T. A. Nieminen, G. Knöener, N. R. Heckenberg, and H. Rubinsztein-Dunlop, "The effect of mie resonances on trapping in optical tweezers," *Opt. Express*, vol. 16, pp. 15039–15051, 2008.

[159] J. P. Barton, D. R. Alexander, and S. A. Schaub, "Theoretical determination of net radiation force and torque for a spherical particle illuminated by a focused laser beam," *Journal of Applied Physics*, vol. 66, no. 10, pp. 4594–4602, 1989.

[160] Y. Roichman, I. Cholis, and D. G. Grier, "Volumetric imaging of holographic optical traps," *Opt. Express*, vol. 14, pp. 10907–10912, 2006.

[161] C.-S. Guo, X. Liu, J.-L. He, and H.-T. Wang, "Optimal annulus structures of optical vortices," *Opt. Express*, vol. 12, no. 19, pp. 4625–4634, 2004.

[162] M. Polin, K. Ladavac, S.-H. Lee, Y. Roichman, and D. G. Grier, "Optimized holographic optical traps," *Opt. Express*, vol. 13, no. 15, pp. 5831–5845, 2005.

[163] S.-H. Lee, Y. Roichman, G.-R. Yi, S.-H. Kim, S.-M. Yang, A. van Blaaderen, P. van Oostrum, and D. G. Grier, "Characterizing and tracking single colloidal particles with video holographic microscopy," *Opt. Express*, vol. 15, pp. 18275–18282, 2007.

[164] F. C. Cheong, B. Sun, R. Dreyfus, J. Amato-Grill, K. Xiao, L. Dixon, and D. G. Grier, "Flow visualization and flow cytometry with holographic video microscopy," *Opt. Express*, vol. 17, pp. 13071–13079, 2009.

[165] S.-H. Lee, K. Ladavac, M. Polin, and D. G. Grier, "Observation of flux reversal in a symmetric optical thermal ratchet," *Phys. Rev. Lett.*, vol. 94, no. 11, p. 110601, 2005.

[166] S.-H. Lee and D. G. Grier, “Flux reversal in a two-state symmetric optical thermal ratchet,” *Phys. Rev. E*, vol. 71, p. 060102(R), 2005.

[167] S.-H. Lee and D. G. Grier, “Giant colloidal diffusivity on corrugated optical vortices,” *Phys. Rev. Lett.*, vol. 96, p. 190601, 2006.

[168] Z. Bouchal and M. Olivk, “Non-diffractive vector bessel beams,” *Journal of Modern Optics*, vol. 42, no. 8, pp. 1555–1566, 1995.

[169] F. C. Cheong, B. J. Krishnatreya, and D. G. Grier, “Strategies for three-dimensional particle tracking with holographic video microscopy,” *Opt. Express*, vol. 18, pp. 13563–13573, 2010.

[170] H. W. Moyses, B. J. Krishnatreya, and D. G. Grier, “Robustness of lorenz-mie microscopy against defects in illumination,” *Opt. Express*, vol. 21, pp. 5968–5973, Mar 2013.

[171] A. Rohrbach, “Stiffness of optical traps: Quantitative agreement between experiments and electromagnetic theory,” *Phys. Rev. Lett.*, vol. 95, p. 168102, 2005.

[172] E.-L. Florin, A. Pralle, E. Stelzer, and J. Hrber, “Photonic force microscope calibration by thermal noise analysis,” *Applied Physics A*, vol. 66, no. 1, pp. S75–S78, 1998.

[173] B. T. Draine, “The discrete-dipole approximation and its application to interstellar graphite grains,” *Astrophys. J.*, vol. 333, p. 848, Oct. 1988.

[174] Y. Harada, “Radiation forces on a dielectric sphere in the rayleigh scattering regime,” *Optics Communications*, vol. 124, pp. 529–541, Mar. 1996.

[175] T. imr and K. Dholakia, “Tunable bessel light modes: engineeringthe axial propagation,” *Opt. Express*, vol. 17, no. 18, pp. 15558–15570, 2009.

[176] L. Carretero, P. Acebal, and S. Blaya, “Three-dimensional analysis of optical forces generated by an active tractor beam using radial polarization,” *Opt. Express*, vol. 22, pp. 3284–3295, Feb 2014.

[177] A. M. Stewart, “Angular momentum of the electromagnetic field: the plane wave paradox resolved,” *European Journal of Physics*, vol. 26, no. 4, p. 635, 2005.

[178] R. N. C. Pfeifer, T. A. Nieminen, N. R. Heckenberg, and H. Rubinsztein-Dunlop, “Optical tweezers and paradoxes in electromagnetism,” *J. Opt.*, vol. 13, no. 4, p. 044017, 2011.

[179] K. Y. Bliokh, A. Y. Bekshaev, and F. Nori, “Extraordinary momentum and spin in evanescent waves,” *Nat Commun*, vol. 5, Mar 2014.

[180] S. Albaladejo, M. I. Marqus, M. Laroche, and J. J. Senz, “Scattering forces from the curl of the spin angular momentum of a light field,” *Phys. Rev. Lett.*, vol. 102, p. 113602, Mar. 2009.

[181] A. I. Kuznetsov, A. E. Miroshnichenko, Y. H. Fu, J. Zhang, and B. Luk’yanchuk, “Magnetic light,” *Sci. Rep.*, vol. 2, Jul 2012.

[182] B. Garca-Cmara, J. F. Algorri, V. Urruchi, and J. M. Snchez-Pena, “Directional scattering of semiconductor nanoparticles embedded in a liquid crystal,” *Materials*, vol. 7, no. 4, pp. 2784–2794, 2014.

[183] L. Wei, A. E. Miroshnichenko, and Y. S. Kivshar, “Control of light scattering by nanoparticles with optically-induced magnetic responses,” *Chinese*

Physics B, vol. 23, no. 4, p. 047806, 2014.

[184] V. Shvedov, A. R. Davoyan, C. Hnatovsky, N. Engheta, and W. Krolikowski, "A long-range polarization-controlled optical tractor beam," *Nat Photon*, vol. 8, pp. 846–850, Nov 2014.

[185] M. C. Lee and I. Feng, "Acoustic levitating apparatus for submillimeter samples," *Review of Scientific Instruments*, vol. 53, no. 6, 1982.

[186] R. M. Diego Baresch, Jean-Louis Thomas, "Observation of a single-beam gradient force acoustical trap for elastic particles: acoustical tweezers," 2014.

[187] C. E. M. Démoré, P. M. Dahl, Z. Yang, P. Glynne-Jones, A. Melzer, S. Cochran, M. P. MacDonald, and G. C. Spalding, "Acoustic tractor beam," *Phys. Rev. Lett.*, vol. 112, p. 174302, Apr 2014.

[188] H. Punzmann, N. Francois, H. Xia, G. Falkovich, and M. Shats, "Generation and reversal of surface flows by propagating waves," *Nat Phys*, vol. 10, pp. 658–663, Sep 2014.

[189] W. J. Wiscombe, "Improved mie scattering algorithms," *Appl. Opt.*, vol. 19, pp. 1505–1509, May 1980.